SECOND HARMONIC GENERATION AS A SURFACE PROBE

By

Jorge Enrique Mejía Sánchez

SUBMITTED IN PARTIAL FULFILLMENT OF THE
REQUIREMENTS FOR THE DEGREE OF
DOCTOR IN SCIENCES (OPTICS)
AT
CENTRO DE INVESTIGACIONES EN OPTICA, A.C.
DEPARTMENT OF OPTICAL PROPERTIES OF MATTER
UNIVERSIDAD DE GUANAJUATO
LEÓN GUANAJUATO, MÉXICO
DECEMBER 2001

Supervisor: Dr. Bernardo Mendoza Santoyo

Internal examiners:

Dr. Alexander Pisarchik

Dra. Gloria Verónica Vázquez García

External examiners:

Dra. Ana Cecilia Noguez Garrido, Instituto de Física, UNAM

To my mother,

father and sister.

Table of Contents

Agradecimientos

De manera especial agradezco el apoyo y enseñanzas que durante la supervisión de esta tesis me brindo el *Dr. Bernardo Mendoza Santoyo.* Gracias por su paciencia y consejos.

Quiero agradecer a la *Dra. Gloria Verónica Vázquez García (CIO)*, *al Dr. Alexander Pisarchik (CIO)* y a la *Dra. Ana Cecilia Noguez Garrido (Instituto de Física, UNAM)* por revisar este trabajo. Sus sugerencias y comentarios han ayudado a enriquecerlo y mejorarlo.

Mi reconocimiento al *Centro de Investigaciones en Optica* por las facilidades otorgadas durante mi estancia en sus instalaciones. En particular quiero agradecer a todas las personas que han pertenecido a la Dirección de Formación Académica por todo el apoyo que me han brindado.

Agradezco el apoyo económico por parte del Consejo Nacional de Ciencia y Tecnología CONACyT, México y del Consejo de Ciencia y Tecnología del Estado de Guanajuato CONCyTEG, México.

Parte fundamental de este proceso a sido mi familia que debido a su apoyo he podido concluir, *Emma*, *Jorge* y *Paty*, gracias por estar siempre a mi lado.

Durante todo este tiempo varias personas han sido importantes por su amistad y apoyo incondicional. A *Elizabeth Falcón, Norberto Arzate, Eric Rosas, Gilberto Gómez, Mario Pacheco, Abigaël Kok* y *Brenda Martínez*, por todos esos perdurables momentos que hemos vivido aqui en León, ustedes han hecho más agradable esta etapa doctoral. A *Elsa Mayorga* por nuestra amistad de años. A *Bárbara Pichardo, Jesús Velázquez* y *Hugo Guzmán* que a pesar de la distancia siempre estuvieron aquí.

Chapter 1

Introduction

The demonstration by Franken et al. [1] in 1961 of the second harmonic generation (SHG) unleashed the development of nonlinear optics as a new branch of physics. In 1961, Bloembergen recognized the potential of nonlinear optics, beginning a theoretical investigation in the summer of that year. One of his theoretical works dealt with the behavior of light waves at the boundary of a nonlinear medium [2]. The classical laws of optical reflection and refraction were generalized to nonlinear optical response. The development of SHG at interfaces of media with inversion symmetry during the decade of the sixties are summarized in a fairly comprehensive paper by Bloembergen et al. [3]. It was followed by a decade with relatively little activity. Since 1980, the subject has experienced a period of continuous growth. For this topic Bloembergen has designated the decade of the sixties as the period of classical antiquity, the seventies as the Middle Ages, with the Renaissance starting in 1980 [4]. As Bloembergen said, the potential of nonlinear optics as a surface-specific tool was not fully exploited until the decade of the eighties. Before some advances were realized. During the decade of the seventies, for example, the demonstration of surface plasmon resonant enhancement of nonlinear susceptibilities was made [5]. We can begin the renaissance of the nonlinear optical spectroscopy with the work of Shu et. al. [6], where the adsorption of CO molecules on a clean crystalline Ni surface was studied. The intensity of SHG decrease proportional to the degree of coverage of the adsorbed monomolecular layer. Adsorption of a monolayer of oxygen on a Si(111) surface of a silicon crystal almost completely suppresses SHG [7]. Heinz et al. have studied the transformation from a Si(111) (2×2) structure for a freshly cleaved surface to a (7x7) structure [7].

This was the origin of one of the most important physical applications of nonlinear optical spectroscopy.

The study of interfaces and in particular of semiconductor surfaces, is very important due to their technological applications in the transistor world. Since the invention of the transistor in 1948 by Bardeen, Brattain and Shockley, all the technological development has rested upon this device. The transistor has made possible to build compact electronic computers and other devices with size moving from microscopic circuits to impressive dimensions comparable to interatomic distances [8]. Nowadays, millions of transistors can be built on a square centimeter of a silicon surface, that is the base material for building an integrated circuit.

Nonlinear optical spectroscopy has been used for basic research in other areas as well. Du et al. [9] developed sum frequency generation (SFG) spectroscopy for the purpose of studying vibrational resonances at molecular interfaces. The SHG and SFG methods can also be used to study the effect of polymer interfaces. A two dimensional orientation phase transition as a function of density of surfactant monolayer has been reported [10].

In the process of manufacturing electronic devices many tools for surface analysis have been developed, among others we have *synchrotron radiation* which is used for surface experiments where high intensity electromagnetic radiation to analyze surfaces is needed. This radiation is useful, for instance, for photoelectron spectroscopy and reflectivity measurements in the ultraviolet region. The *low energy electron diffraction* (LEED) method is used for determining surface structures. Low energy electrons have a wavelength comparable with the internuclear spacings of the atoms in a crystal, e.g $\approx$1 Å for an energy of $\approx$150 eV. Electrons with this energy penetrate only a few atomic layers due to the strong interaction with the solid so that the outermost surface layers can be probed. *Photoelectron or photoemission spectroscopy* is a technique that is based on the photoelectric effect. The crystal is irradiated and photoelectrons are emitted from the filled valence bands just below the Fermi level with different kinetic energies. By means of a retarding potential the number of electrons with kinetics energies greater than a fixed energy can be determined. If the experiments are performed in the ultraviolet spectral region, then the technique is called *ultraviolet photoemission spectroscopy* (UPS) or if soft-x rays are used we then call it *x-ray photoemission spectroscopy* (XPS). *Auger electron spectroscopy* (AES) is used to probe for impurities. In this technique an electron (auger electron) is emitted after deexcitation of the atom once it has been bombarded with energetic electrons or photons. The

emitted electron has a characteristic kinetic energy determined by the quantum states of the atom.

Besides the techniques mentioned above, we have the *optical techniques*, which unlike others, they do not require ultra-high vacuum (UHV) environments and also they are non-invasive, non-destructive, and have wide spectral coverage as well. These techniques do not have enough surface sensitivity unless the signal contributed by the bulk media can be suppressed.

The use of non-linear optical techniques to study surface phenomena has gained much attention in recent years. In particular second harmonic generation (SHG) has been established as a powerful spectroscopy to study a wide range of physical and chemical phenomena at the surface of centrosymmetric materials, as it has a high-surface sensitivity, is non-invasive and non-destructive, and can be used out of UHV conditions and even at buried interfaces [11–19]. Good reviews of these topics are the papers of Lüpke [20] and Downer et al. [21]. The surface sensitivity of SHG is due to the fact that within the dipole approximation a centrosymmetric environment does not radiate SH, while the inversion symmetry is broken at its surface, thus allowing the radiation of SH. On the experimental side, new tunable high intensity laser systems have made SHG spectroscopy readily accessible and applicable to a wide range of systems [11–19]. In particular, the use of femtosecond lasers offers broad-bandwidth fundamental pulses which can be used to obtain SH radiation over a broad spectral range without laser tuning. For instance, Wilson et al [22], have applied a new spectroscopic technique to measure simultaneously the intensity and the phase of SH radiation from a $Si/SiO_2/Cr$ metal-oxide-semiconductor capacitor in the spectral range of the Si E_1 bulk critical point without laser tuning by using 15-fs pulses. More recently, Mitchell et al. [23], have also used femtosecond pulses to study adsorbate covered Si(111) surfaces around E_1. The SHG advances on the experimental side, are being followed by the theoretical development of the field. Some recent progress for the case of semiconducting and metallic systems have appeared in the literature, where the confrontation of theoretical models with experiment has succeeded, yielding correct physical interpretations for the SHG spectra [21, 24–32].

The SHG technique arises because a second-order process is forbidden, within the dipole approximation, in a medium with inversion symmetry, i.e. centrosymmetric medium [33]. Such a symmetry will necessarily be broken at an interface, for instance the discontinuity of the interface (i.e. the structural change in passing from the bulk to the surface layer) is sufficient to break such a symmetry, and thus

the second-order non-linear process is therefore allowed at the surface.

Consider the following electromagnetic optical wave

$$\vec{E}(\vec{r},t) = \vec{E}(\vec{r})e^{-i\omega t}, \tag{1.1}$$

oscillating at frequency ω impinging on a medium. Within the dipole approximation, the total polarization induced by this wave is given by

$$\vec{P}(\vec{r},t) = \overleftrightarrow{\alpha} \cdot \vec{E}(\vec{r})e^{-i\omega t} + \overleftrightarrow{\chi} : \vec{E}(\vec{r})\vec{E}(\vec{r})e^{-i2\omega t}, \tag{1.2}$$

where the first and second terms on the right hand side give the response at ω and 2ω, respectively. After a proper Fourier transformation, we obtain

$$\vec{P}(\omega) = \overleftrightarrow{\alpha}(\omega) \cdot \vec{E}(\omega), \tag{1.3}$$

as the linear polarization proportional to the incoming field with $\overleftrightarrow{\alpha}(\omega)$ the linear polarizability tensor and

$$\vec{P}(\vec{r},2\omega) = \overleftrightarrow{\chi}(2\omega) : \vec{E}(\vec{r},\omega)\vec{E}(\vec{r},\omega) \tag{1.4}$$

as the second-order non-linear polarization proportional to the squared of the incoming field, this polarization is the source of the SH generation. The third rank tensor $\overleftrightarrow{\chi}(2\omega)$ is the second-order non-linear susceptibility, which characterize the SH response of the medium. A typical sketch for surface SHG is shown in Fig. 1.1.

Now, if we consider a medium with inversion symmetry (e.g. a cubic crystal), the operation $\vec{r} \to -\vec{r}$ must leave the system invariant. As both $\vec{P}$ and $\vec{E}$ are polar vectors and $\overleftrightarrow{\chi}$ should be invariant, from Eq. (1.4) we have that,

$$\begin{aligned} \vec{P}(-\vec{r},2\omega) &= \overleftrightarrow{\chi}(2\omega)\vec{E}(-\vec{r},\omega)\vec{E}(-\vec{r},\omega) \\ -\vec{P}(\vec{r},2\omega) &= \overleftrightarrow{\chi}(2\omega)(-\vec{E}(\vec{r},\omega))(-\vec{E}(\vec{r},\omega)) \\ \vec{P}(\vec{r},2\omega) &= -\overleftrightarrow{\chi}(2\omega)\vec{E}(\vec{r},\omega)\vec{E}(\vec{r},\omega). \end{aligned} \tag{1.5}$$

As we can see, if we compare Eq. (1.5) with Eq. (1.4) the only solution is that

$$\overleftrightarrow{\chi} = 0 \quad \Leftrightarrow \quad \text{inversion symmetry} \tag{1.6}$$

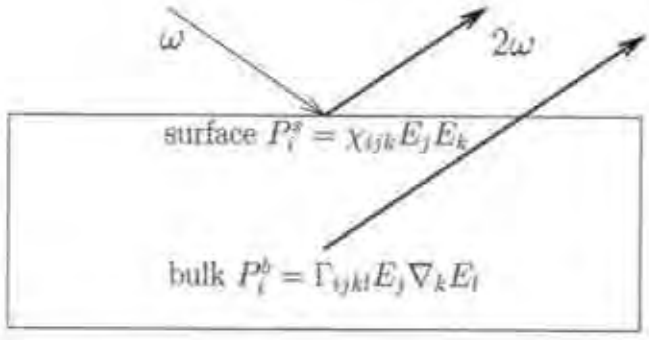

Figure 1.1: Sketch of the surface second harmonic generation technique. An incident electric field oscillating at the fundamental frequency ω induces a second-order non-linear optical response at the bulk and surface, characterized by $\vec{P}^b$ and $\vec{P}^s$ respectively. In reflection a harmonic wave at 2ω that is surface and bulk generated could be observed.

indicating that the dipolar contribution to SHG is forbidden for centrosymmetric media. At an interface between two media where the inversion symmetry is necessarily broken, the dipolar term is allowed, making this technique a highly surface specific probe to analyze surfaces and interfaces.

When higher-order effects are taken into account, the effective non-linear polarization $\vec{P}_{eff}(2\omega)$ generally should consists of a series of multipoles terms, which for a non-magnetic medium is written as

$$\vec{P}_{eff}(2\omega) = \vec{P}(2\omega) - \nabla \cdot \overleftrightarrow{Q}(2\omega), \tag{1.7}$$

where $\vec{P}(2\omega)$ is the electric-dipole polarization and $\overleftrightarrow{Q}$ is the electric-quadrupolar polarization. The terms in Eq. (1.7) are quadratic functions of the field and/or their derivatives. Up to the first derivatives of the field these terms are written as [34]

$$\vec{P}(2\omega) = \overleftrightarrow{\chi} : \vec{E}(\omega)\vec{E}(\omega) + \overleftrightarrow{\chi}_P^{(Q)} : \vec{E}(\omega)\nabla\vec{E}(\omega) \tag{1.8}$$

$$\overleftrightarrow{Q}(2\omega) = \overleftrightarrow{\chi}_Q^{(Q)} : \vec{E}(\omega)\vec{E}(\omega), \tag{1.9}$$

where $\overleftrightarrow{\chi}^{(Q)}$ is a fourth rank tensor that describes the electric quadrupolar contributions. The subscript P (Q) refers to quadrupolary induced dipole (quadrupole).

Defining a general susceptibility $\overleftrightarrow{\chi}^{(Q)}$ as

$$\overleftrightarrow{\Gamma}(2\omega) = \overleftrightarrow{\chi}_P^{(Q)}(2\omega) - 2\overleftrightarrow{\chi}_Q^{(Q)}(2\omega), \tag{1.10}$$

then the effective polarization can be written as

$$\vec{P}_{eff}(2\omega) = \overleftrightarrow{\chi} : \vec{E}(\omega)\vec{E}(\omega) + \overleftrightarrow{\Gamma} : \vec{E}(\omega)\nabla\vec{E}(\omega) - (\nabla\overleftrightarrow{\Gamma}) : \vec{E}(\omega)\vec{E}(\omega). \tag{1.11}$$

The first term is the electric dipole contribution and the other two are the electric quadrupolar contributions. The second term is related to the field gradient and the third term that is zero in the bulk of a homogeneous medium, has a non-zero value at the surface due to structural discontinuity [35], and although originates from the surface, it only depends on bulk parameters [34].

Therefore, we can write the surface and bulk main contributions to SHG as

$$\vec{P}_i^S(2\omega) = \overleftrightarrow{\chi}_{ijk}E_j(\omega)E_k(\omega), \qquad \text{Surface} \tag{1.12}$$

and

$$\vec{P}_i^B(2\omega) = \overleftrightarrow{\Gamma}_{ijkl}E_j(\omega)\nabla_k E_l(\omega), \qquad \text{Bulk} \tag{1.13}$$

respectively, where the last term in Eq. (1.11) has been neglected.

Measurements of SHG from the interface allows us to deduce the surface non-linear susceptibility. In such measurements the bulk may contribute to the signal to the same order of magnitude and may complicate the experiment since the detector collects the total SHG signal contributed by both the surface and the bulk [36] (see Fig. 1.1). However, in media with large dielectric constant such as metals and semiconductors, the contribution from the bulk is much weaker [37]. For some surfaces, the bulk contribution is at most an order of magnitude smaller than the surface term and can be safely neglected [15,24,25,35,37]. Thus, systems for which $P^B \ll P^S$, have SHG as a surface specific probe, making this technique a desirable tool to analyze surfaces and interfaces.

Notice that the non-linear susceptibility $\overleftrightarrow{\chi}(2\omega)$ directly reflects the structural symmetry of the surface or interface and gives us information from the surface electronic and vibrational transitions [38]. The origin of the surface SHG arises from two sources [33, 37]: a) structural discontinuity as changes in the atomic positions, symmetry, electron density, as well as the presence of adsorbates at the surface and b) field discontinuity or variation of the field across the interface.

The former dominates at a semiconductor surface with dangling bonds* or where a monolayer (ML) of molecules is adsorbed with a preferred orientation at an interface [40]. On the other hand, field discontinuity dominates on a liquid or glass surface, where the surface structure is not different from that in the bulk. Based on the origin of the SHG, we can define an interface layer as the region where both the structure and the field change significantly [37]. If the thickness of an interface layer is much smaller than the optical wavelength the long wavelength approximation can be assumed.

We define the SHG efficiency as

$$\mathcal{R}(\omega) = \frac{I(2\omega)}{I^2(\omega)} \tag{1.14}$$

where the intensity is $I(\omega) = (c/8\pi)|E(\omega)|^2$, then

$$\mathcal{R}(\omega) = \frac{8\pi}{c}\frac{|E(2\omega)|^2}{|E(\omega)|^4}, \tag{1.15}$$

with c the speed of light. To make a simple estimate of the order of magnitude of $\mathcal{R}$ we proceed as follows. The fact that $\overleftrightarrow{\chi}$ is different from zero only near the surface or interface of the system, allow us to make the simplifying approximation that the non-linear polarization given by Eq. (1.4) is localized within a sheet of infinitesimal width. This surface polarization $\mathcal{P}$ is of the order of the width of the sheet times $P(2\omega)$. We take this width to be of the order of an atomic distance, i.e. the Bohr radius a_B. On the other hand, the field radiated by such (non-linear) polarization sheet is of the order of $\mathcal{P}/\lambda$ with λ the wavelength of the radiated field, i.e. $E(2\omega) \sim \mathcal{P}/\lambda \sim a_B P/\lambda$. From Eq. (1.4), we notice that the units of $\overleftrightarrow{\chi}$ are those of inverse electric field (recall that P is polarization per unit volume), where the electric field is estimated to be of the order of e/a_B^2, with e the electron charge. Then we take the $\chi \sim (e/a_B^2)^{-1}$ putting everything together into Eq. (1.15) we get

$$\begin{aligned}\mathcal{R}(\omega) &\sim \frac{1}{c}\left(\frac{a_B P}{\lambda}\right)^2 \frac{1}{E^4(\omega)} \sim \frac{1}{c}\left(\frac{a_B \chi E^2(\omega)}{\lambda}\right)^2 \frac{1}{E^4(\omega)} \sim \frac{1}{c}\left(\frac{a_B \chi}{\lambda}\right)^2 \\ &\sim \frac{1}{c}\left(\frac{a_B^3}{e\lambda}\right)^2 \sim 10^{-21} \quad \text{cm}^2/\text{W} \quad (\text{for } \lambda \sim \text{visible}).\end{aligned} \tag{1.16}$$

*A dangling bond is an orbital of a surface atom of a crystal that is directed outward from the surface and is unbounded [39].

Due to the generality of this argument, this estimate can be used not only for semiconductors but also for metals, for which we expect a similar order of magnitude. However, the non-linear reflectance may still be increased in regions of resonance and suppressed in regions of transparency. The estimation of Eq. (1.16) also shows that very powerful lasers are needed to observe SHG.

The first experimental method used to detect SHG from semiconductors and metals was that of Bloembergen and coworkers [3]. They presented experimental results on the polarization and directional dependence of SHG of Si, Ge and Ag. Heinz *et al.* [40] made measurements of optical SHG spectra of adsorbates at submonolayers coverages. They obtained the position and the lineshape of the electronic transition for rhodamine-dye molecules adsorbed onto fused silica. More recently, we can find in the literature experimental studies on SHG as a selective tool to probe excitons on NiO and CuCl surfaces [41] or for magnetized surfaces [42]. For semiconductors, the technique of SHG has been applied to the Si surface. For instance, we find experiments on the clean or oxide surface [11, 12, 35, 43], on the clean or H-adsorbed surface [17, 19, 44] and B-doped surface [30].

On the theoretical side, different approaches for studying SHG at surfaces have been developed [2, 24, 25, 27, 29, 32, 45–53]. We find in the literature the early theoretical work of transmitted and reflected SHG of light waves at the boundary of non-linear media of Bloembergen and Pershan [2]. Rudnick and Stern [54] made a theoretical scheme for the calculation of the microscopic susceptibility components for a flat metallic surface with some limitations. Aksipetrov *et al.* [45] carried out an analysis of SHG in crystals showing the possibility of separating out the non-linear optical contribution from the layer near the surface. Almost at the same time, Sipe *et al.* [46] developed a phenomenological analysis of the surface and bulk susceptibility tensors, identifying their independent components, and the functional dependence of the second-order reflectance on the incidence and azimuthal angles and as a function of the incoming and outgoing polarizations for different crystal surfaces. However, they did not attempt actual calculations of the susceptibility tensor. Mizrahi and Sipe [47] applied a Green method to calculate SHG in terms of the surface non-linear susceptibility.

Models for the calculation of the non-linear susceptibility can be classified according to phenomenological and microscopic models. In the first class, one approximates the susceptibility with simple expressions, usually those of harmonic oscillators and adjust, somehow, this expression to usually linear optical data. The second class uses quantum mechanical expressions for the non-linear susceptibility

and evaluates them according to semi-empirical tight-binding (SETB) and *ab initio* methods. Both approaches have been applied to semiconducting [27,29,32,51–53] and metallic surfaces [55–60].

For SHG at semiconductors we find the phenomenological model of Schaich and Mendoza [48] where local field effects are taken into account. Here, the system is considered to be composed of polarizable entities. With this approach, Mendoza and Mochán [24] gave simple analytical expressions modeling a centrosymmetric semi-infinite system by a pointlike polarizable bond distribution that responds harmonically to the perturbing field. In particular, the polarizable bond model (PBM) was able to corroborate, for the first time, the origin of the E_1 in Si(100). Indeed, this model accounts for the local field effect, that at the surface of a centrosymmetric material allows SH through atomic relaxation [24,25]. More recently, the full surface relaxation of Si(100) was used in the PBM to study with more detail SHG at this surface [61]. Alternative PBM studies have been put forward in [62], and in particular in [63] a more rigorous calculation for the bond-bond interaction is discussed and implemented. The phenomenological methods have been able to give a qualitative picture of the SHG phenomena for Si surfaces. A dipolium model, where the dipoles are smeared continuously through out the system, was applied to Si surfaces with qualitative results resembling the experiments. [24,64].

Within the microscopic models for SHG at semiconductors surfaces we can find the followings approaches: Gavrilenko and Rebentrost used the SETB method with a sp^3s^* basis to calculate the χ_{zzz} component [52,53] of Si surfaces. Cini proposed a microscopic formalism for SHG [65]. He found closed expressions for the SH intensity. The theory allows to study SHG as a function of substrate band structure, overlayer chemical properties and experimental geometry. Such a model, within the SETB scheme has been successfully applied by Reining et al. [51] and Mendoza et al. [27]. On the other hand, *ab initio* schemes have been recently reported by Gavrilenko *et al.* [29] and Mendoza *et al.* [32]. Gavrilenko *et al.* [29] studied the non-linear response of Si(100) to H and Ge adatoms at Si(100)2×1 surfaces whereas Mendoza *et al.* studied Si(100)c(4×2) surfaces with H adsorption [32].

Because of the technological importance of Si, the optical techniques above have been applied extensively to study different aspects of Si(100) and Si(111)

surfaces with various reconstructions[†], ad-atom coverage, etc. [14–20,35,66]. Most of the studies dealt with the (100) surface because most electronic devices are formed on this surface. The interest has been focused on understanding the basic physical properties of the clean surface, its growth, the process of adsorption of foreign atoms, etc. showing how this particular spectroscopy is becoming a reliable surface tool [20,21].

The purpose of this work is to study the optical properties of surfaces by SHG. In particular, we analyze the atomic structure of the surface, the surface symmetry, the main microscopic contributions to the non-linear process that converts the fundamental frequency into the SH radiation. We chose silicon, since its surfaces is the most used in technological applications, and study the properties of two of its faces, the (100) and (111). The Si(111) (1*times*1) is the simplest of all semiconductor surfaces, in the sense that its equilibrium relaxed geometry is almost identical to an ideally terminated (111) surface [67]. Also, as H saturates every Si dangling bond, there are no surface-related electronic states in the forbidden gap. Experimentally, this surface can be prepared to a high level of quality [67,68]. Indeed, the experiments are performed on a high quality surface produced by a state-of-the-art technique by the German group of Professor W. Daum. Also, computationally it is very simple as it has only one atom per unit surface cell. Therefore, this surface presents a very good reference system for SHG studies, since neither the atomic structure nor electronic surface states in the gap region should be of concern when comparing the theoretical and experimental SHG spectra. The microscopic nonlinear surface susceptibility tensor $\overleftrightarrow{\chi}$ is evaluated within the polarizable bond model and the microscopic formulation, using both the semi-empirical tight binding (SETB) and the *ab-initio* schemes. The SHG spectra are compared among the three different approaches, and with the available experimental results. We show that SHG is a very powerful tool to study several physical aspects of a semiconductor surface. Based on the previous success, we finally proceed to calculate SHG from the most fascinating of all semiconductor surfaces, the Si(111)(7×7). The reconstruction of this surface involves a unit cell 7 times larger than the ideally terminated (1×1) unit cell, thus implying a *tour de force* calculation with very surprising results.

In Chapter 2 we describe the three methods used to calculate the SHG. We

[†]The rearrangement of the atoms on a surface lowering the translational symmetry of the surface layers is called surface reconstruction.

begin with the polarizable bond model (PBM), and then, the microscopic SETB and *ab-initio* methods are described. We conclude with a section devoted to the calculation of the SHG radiation within the three-layer-model, that is new in the field.

In Chapter 3 we apply the SETB microscopic formulation to calculate the second harmonic spectra of a clean single-domain Si(100)c(4 × 2) surface. This calculation has only been done in double-domain surfaces. The new physics in the single domain surface comes about as the dimer formed between the top-most Si atoms and the sublayer atoms give a surface with a C_{1v} symmetry class, characterized by ten non-zero elements of the non-linear surface susceptibility tensor $\overleftrightarrow{\chi}$. This symmetry gives rise to a second harmonic signal that is anisotropic in the azimuthal angle ϕ which the incident plane of the fundamental beam of frequency ω makes with the surface plane. The anisotropy depends on the surface or bulk nature of the SH resonance. In particular, the spectral range around the Si E_1 critical point is investigated.

For Si(111):H (1×1), the most ideal of all semiconductor surfaces, we apply the three methods to study SHG. In Chapter 4, we first use the polarizable bond model (PBM) to study the atomic structure of the surface. The PBM is driven by the local-field interaction among the polarizable entities that make up the system. We show that the Si-H bond can be used to obtain a theoretical SHG spectrum in qualitative agreement with experimental data for the resonant E_1 bulk critical point of Si, and that SHG can be strongly modified by changing the position of the centroid of the Si back bonds in this surface. This is the first time that such modeling is carried out, and is in good qualitative agreement with experimental results.

In Chapter 5, we then apply the SETB and *ab-initio* schemes to evaluate the microscopic nonlinear surface susceptibility tensor $\overleftrightarrow{\chi}$. We make an extensive analysis on the different parameters that enter the calculation in order to asses the convergence of the results. Thus, we study this convergence as a function of the number of crystalline planes, number of k-points, energy cut-off, etc. that is usually not done in this kind of calculations due to the excessive computing time of larger surface unit cells. The qualitative agreement between theory and experiment is good in both schemes.

In Chapter 6, we use the SETB microscopic formulation to calculate SHG at the Si(111)7×7 surface. This fascinating surface has several characteristics which were never considered before, like the reduction of its symmetry due to the

interlayer interaction near the surface induced by the reconstruction. Although the agreement with the experiment is not as good as in the previous cases, several issues are analyzed with very surprising results.

Finally, in Chapter 7 we give the general conclusions of this thesis and an overlook of possible future work in the field of surface non-linear optics.

Chapter 2

Methods to Calculate Second Harmonic Generation

The development of high-power tunable lasers with broad spectral range has stimulated experiments in nonlinear surface spectroscopy. In particular second harmonic generation has been used to study phase transitions, atomic structure, adsorption of atoms, etc. at surfaces and interfaces [11, 15–18, 66]. An important example of surface SHG is given by the resonance measured around 3.3 eV (in the two-photon energy) in Si [11]. This resonance coincides with the E_1 bulk critical point of Si, that is SHG (dipolar) allowed due to the presence of the surface. Modifications on the surface change this resonance, and thus it can be ascribed as a surface enhanced SHG resonance. Therefore, this E_1 surface SHG peak has been used to study different aspects of the Si(100) and Si(111) surfaces with several reconstructions, adatom coverage, etc [11, 15–18, 66]. Höfer [17] and Dadap et al. [19], demonstrated the ability of SHG to describe the dynamics of H adsorption on Si surfaces. Recently in Ref. [68] femtosecond laser pulses have been used to measure SHG of several chemical modifications of Si(111) surfaces around E_1.

Therefore it is necessary the development of the theoretical approaches to explain and understand the physics involved in the experiments. On one hand, phenomenological methods have been able to give a qualitative picture of the phenomena. On the other hand, microscopic methods have been developed to study more rigorously the SHG at surfaces. However, these microscopic approaches are much more computationally demanding and their interpretation is not as direct as in the phenomenological methods. In this Chapter we will explain both

methods. In the phenomenological methods, we will use the polarizable bond model [24, 25, 61] and in the microscopic methods, we will use the semi-empirical tight-binding [27, 30–32, 50, 51, 69–71] and *ab initio* [30, 32, 67, 72] schemes which have been used successfully in several semiconductor surfaces.

2.1 Polarizable Bond Model

The dipole model has been used successfully in several systems. This method gives an explicit account of the microscopic crystalline effects and is based on treating the material as an ordered array of point-like, polarizable entities [24, 25, 48, 73, 74]. If an external field perturbs each entity then it develops various multipole moments which, in turn, produce fields that influence neighbors. The self-consistent solution for the net polarization of the system allows one to calculate the various parameters required to calculate the optical response. The polarization induced in a semiconductor originates from the displacement of its charge distribution. This charge distribution typically has a strong maximum at the middle of each bond for mono-atomic semiconductors except for diamond, which has a bimodal distribution [75]. Thus, the *polarizable bond model* is based on treating the semiconductor as a lattice of point-like polarizable bonds. The model was used previously by Mochán and Barrera [73, 74] for the linear response of clean and Br-adsorbed Ge surface, where they show that the local field effect induces a change in the macroscopic dielectric response of cubic crystals close to their surface. On the other hand, Schaich and Mendoza [48] developed a model for surface second harmonic generation (SHG) consisting of a semi-infinite system made up of polarizable entities. Then, the model was developed for the unreconstructed silicon surface by Mendoza and Mochán [24, 25].

We expect the local field to have large consequences in SHG through the following mechanism: consider a localized polarizable entity and a semi-infinite crystal made up of its replicas. If each entity is centrosymmetric it would have no electric-dipole-allowed second harmonic (SH) transition, though it may have electric-quadrupolar and magnetic-dipolar contributions proportional to $\vec{\mathcal{E}}\nabla\vec{\mathcal{E}}$ where $\mathcal{E}_i$ is the local field acting at site i. The external field has a very slow spatial variation whose scale is of the order of the wavelength λ, although the field induced by a nearby entity j may have a very large variation, with a scale determined by the distance from j to i, r_{ij}, which is of atomic dimensions a. Different neighbors

contribute to the gradient $\nabla\vec{\mathcal{E}}$ along different directions, so that, if the site i itself is centrosymmetric, these large gradients will cancel out among themselves, leaving only a small residual gradient of the order $\mathcal{E}/\lambda$. This cancellation is no longer possible at the surface, where $|\nabla\mathcal{E}| \approx \mathcal{E}/a$, yielding a large SH surface polarization. If written in terms of the microscopic field $\vec{E}$ this surface polarization is proportional to $\vec{E}\vec{E}/a$, which corresponds to a large surface allowed dipolar SH process.

The polarizable bond model replaces the crystal by an array of point-like dipoles. Each dipole is considered as an anisotropic point-like harmonic oscillator of cylindrical symmetry, with charge e and mass m. The x coordinate is chosen to be along the symmetry axis and y, z perpendicular to it. The resonant frequencies of the dipole are denoted by $\omega_x = \omega_{\parallel}$ that corresponds to the response parallel and by $\omega_y = \omega_z = \omega_{\perp}$ that corresponds to the response perpendicular to the bond.

The first order induced dipole moment is written as

$$\vec{p}(\omega) = \overleftrightarrow{\alpha}(\omega) \cdot \vec{\mathcal{E}}, \tag{2.1}$$

where $\vec{\mathcal{E}}$ is the local field and $\overleftrightarrow{\alpha}(\omega)$ the linear microscopic polarizability tensor which is given by

$$\alpha_{ij}(\omega) = \begin{pmatrix} \alpha_{\parallel}(\omega) & 0 & 0 \\ 0 & \alpha_{\perp}(\omega) & 0 \\ 0 & 0 & \alpha_{\perp}(\omega) \end{pmatrix} \tag{2.2}$$

where $\alpha_{xx} \to \alpha_{\parallel}$ and $\alpha_{yy} = \alpha_{zz} \to \alpha_{\perp}$ for its response parallel and perpendicular to the bond respectively and

$$\alpha_i(\omega) = \frac{e^2/m}{\omega_i^2 - \omega^2}, \tag{2.3}$$

with $i = \parallel$ or $\perp$.

To determine the polarizability in the crystal coordinate system we use the following expression

$$\overleftrightarrow{\alpha} = \alpha_{\parallel}\tilde{e}^{\lambda}\tilde{e}^{\lambda} + \alpha_{\perp}(\overleftrightarrow{1} - \tilde{e}^{\lambda}\tilde{e}^{\lambda}), \tag{2.4}$$

where $\overleftrightarrow{1}$ is the unit tensor and $\hat{e}^{\lambda}$ is the unit vector along the direction of the $\lambda - th$ bond. The microscopic polarizability of each dipole, indeed, depends on its position through its particular bond orientation and its surface or bulk location.

The linear response of the oscillator is well described by eq. (2.1), since the linear quadrupolar and magnetic contributions are negligible in the long-wavelength limit [76]. The second-order induced dipole moment is given by [25, 48]

$$(\vec{p}_{n\lambda}(2\omega))_i = [\chi^{(d)}_{ijkl}(\omega) + \chi^{(m)}_{ijkl}(\omega)]\mathcal{E}_j(\nabla_k\mathcal{E}_l), \tag{2.5}$$

with

$$\chi^{(d)}_{ijkl}(\omega) = \frac{1}{2e}[\alpha_{il}(2\omega)\alpha_{jk}(\omega) + \alpha_{ik}(2\omega)\alpha_{jl}(\omega)], \tag{2.6}$$

$$\chi^{(m)}_{ijkl}(\omega) = \frac{3}{2e}[\alpha_{il}(2\omega)\alpha_{jk}(\omega) - \alpha_{ik}(2\omega)\alpha_{jl}(\omega)]. \tag{2.7}$$

Here $\overleftrightarrow{\chi}^{(d)}$ and $\overleftrightarrow{\chi}^{(m)}$ are the dipolar and magnetic originated contributions to the microscopic second-order susceptibility of the dipole oscillator respectively. Then, Eqs. (2.6) and (2.7) are simple relations between the non-linear susceptibilities (dipolar and quadrupolar) with the linear polarizability for harmonic oscillators [25, 48]. Finally, the second-order induced electric quadrupolar moment is

$$Q_{ij}(2\omega) = \chi^{(Q)}_{ijkl}(\omega)\mathcal{E}_k\mathcal{E}_l, \tag{2.8}$$

where $\chi^{(Q)}_{ijkl}(\omega)$ is the quadrupolar susceptibility given by [25, 48]

$$\chi^{(Q)}_{ijkl}(\omega) = \frac{1}{2e}[\alpha_{il}(\omega)\alpha_{jk}(\omega) + \alpha_{ik}(\omega)\alpha_{jl}(\omega)]. \tag{2.9}$$

The microscopic susceptibilities $\overleftrightarrow{\alpha}$ and $\chi^{(d),(m),(Q)}$ of a single oscillator given by expressions (2.2), (2.6), (2.7) and (2.9) respectively determine all the relevant response functions within the long wavelength limit. It can be seen also from these equations, that from the knowledge of the linear polarizabilities $\alpha_i(\omega)$ the non-linear susceptibilities, for a single dipole, can be obtained (by substitution of Eq. (2.4) into Eqs. (2.6), (2.7) and (2.9)) and therefore, the total microscopic non-linear behavior as well.

The sum of the dipole moment of aech dipole of the sistem gives its total polarization to an external field. Then, the total induced linear dipole moment

of every dipole that is in a plane ℓ and that has an orientation λ is given by Eq. (2.1) which is written in the form

$$\vec{p}_{\ell\nu\lambda}(\omega) = \overleftrightarrow{\alpha}^{\ell\nu\lambda}(\omega) \cdot \left(\vec{E}^{(ext)}(\vec{r}_{\ell\nu\lambda}, \omega) + \sum_{\ell'\nu'\lambda'} \overleftrightarrow{M}_{\ell\nu\lambda\ell'\nu'\lambda'} \cdot \vec{p}_{\ell'\nu'\lambda'}(\omega) \right) \tag{2.10}$$

where ν numbers the individuals dipoles that make up the plane ℓ with the same orientation λ. The term in parentheses in Eq. (2.10) is the local field $\vec{\mathcal{E}}$ which is the sum of the external field $\vec{E}^{(ext)}$ plus the fields generated by the surrounding dipoles, $\overleftrightarrow{M}$ is the dipolar interaction tensor between dipoles $\ell\nu\lambda$ and $\ell'\nu'\lambda'$ given by

$$\overleftrightarrow{M}_{\ell\nu\lambda\ell'\nu'\lambda'} = \nabla\nabla \frac{1}{|\vec{r} - \vec{r}_{\ell'\nu'\lambda'}|}\bigg|_{\vec{r}=\vec{r}_{\ell\nu\lambda}}, \tag{2.11}$$

where the gradient operator acts over $\vec{r}$. The sum in Eq. (2.10) is over all dipoles $\ell'\nu'\lambda' \neq \ell\nu\lambda$ and can be carried out by using a planewise summation [77].

Within the long wavelength approximation the slow spatial variation of the external field is neglected so that $\vec{E}^{(ext)}(\vec{r}_{\ell\nu\lambda}, \omega) \to \vec{E}(A, \omega)$ with $\vec{E}(A, \omega)$ being the external field independent of position. In such a case, all dipoles with the same orientation λ in a particular plane would have the same dipole moment; this permits the ν index to be dropped in the dipole moment expression, i.e. $\vec{p}_{\ell\nu\lambda} \to \vec{p}_{\ell\lambda}$ and the sum over ν' in Eq. (2.10) produces the interplane interactions

$$\overleftrightarrow{\mathcal{M}}_{\ell\lambda\ell'\lambda'} = {\sum_{\nu'}}' \overleftrightarrow{M}_{\ell\nu\lambda\ell'\nu'\lambda'}, \tag{2.12}$$

here the prime on the sum indicates that the self interaction of a dipole should be excluded, i.e. the term with $\nu = \nu'$, when both $\ell = \ell'$ and $\lambda = \lambda'$. Notice that the tensor $\overleftrightarrow{M}$ depends on the difference $(\vec{r}_{\ell\nu\lambda} - \vec{r}_{\ell'\nu'\lambda'})$, which means that after summing over ν' the tensor $\overleftrightarrow{\mathcal{M}}$ does not depend on ν [77].

Then we obtain from Eq. (2.10) that

$$\sum_{\ell'\lambda'} [\vec{1}\delta_{\ell\ell'}\delta_{\lambda\lambda'} - \overleftrightarrow{\alpha}^{\ell\lambda} \cdot \overleftrightarrow{\mathcal{M}}_{\ell\lambda\ell'\lambda'}] \cdot \vec{p}_{\ell'\lambda'}(\omega) = \overleftrightarrow{\alpha}^{\ell\lambda}(\omega) \cdot \vec{E}(A, \omega), \tag{2.13}$$

that is a set of $3 \times \lambda \times \ell$ equations to be solved for the linear dipole moments of each dipole λ in the plane ℓ. The total polarization is obtained by summing the

contributions of all dipoles as,

$$\vec{p}(\omega) = \sum_{\ell\lambda} \vec{p}_{\ell\lambda}(\omega), \tag{2.14}$$

For the description of the non-linear response, the total second-order dipole moment of every dipole $\ell\nu\lambda$ is the sum of the second-order non-linear response $\vec{p}_{\ell\nu\lambda}(2\omega)$ to the spatially varying local field plus the linear response to the field at the harmonic frequency 2ω due to the oscillating quadrupoles

$$\begin{aligned} \vec{p}^{(tot)}_{\ell\nu\lambda}(2\omega) &= \vec{p}_{\ell\nu\lambda}(2\omega) \\ &\quad + \overleftrightarrow{\alpha}^{\ell\nu\lambda}(2\omega) \cdot \left(\vec{\mathcal{E}}^{(Q)}_{\ell\nu\lambda}(2\omega) + \sum_{\ell'\nu'\lambda'} \overleftrightarrow{M}_{\ell\nu\lambda\ell'\nu'\lambda'} \cdot \vec{p}^{(tot)}_{\ell'\nu'\lambda'}(2\omega) \right), \end{aligned} \tag{2.15}$$

where

$$(\vec{p}_{\ell\nu\lambda}(2\omega))_i = \chi^{(d)\ell\nu\lambda}_{ijkl} (\vec{\mathcal{E}}_{\ell\nu\lambda}(\omega))_j \nabla_l (\vec{\mathcal{E}}_{\ell\nu\lambda}(\omega))_k. \tag{2.16}$$

Expression (2.16) is obtained from Eq. (2.5) where we have neglected the magnetic contribution of the magnetic susceptibility of each bond. The second-order dipole moment is also driven by the linear response to the field at 2ω due to the oscillating quadrupoles,

$$(\vec{\mathcal{E}}^{(Q)}_{\ell\nu\lambda}(2\omega))_i = \frac{1}{2} \sum_{\ell'\nu'\lambda'} (\overleftrightarrow{N}_{\ell\nu\lambda\ell'\nu'\lambda})_{ijk} (\overleftrightarrow{Q}_{\ell'\nu'\lambda'}(2\omega))_{jk}, \tag{2.17}$$

which, with the help of Eq. (1.8), can be written as

$$(\vec{\mathcal{E}}^{(Q)}_{\ell\nu\lambda}(2\omega))_i = \frac{1}{2} \sum_{\ell'\nu'\lambda'} (\overleftrightarrow{N}_{\ell\nu\lambda\ell'\nu'\lambda})_{ijk} \chi^{(Q)\ell'\nu'\lambda'}_{jklm} (\vec{\mathcal{E}}_{\ell\nu\lambda}(\omega))_l (\vec{\mathcal{E}}_{\ell\nu\lambda}(\omega))_m. \tag{2.18}$$

Finally, the last term on the left-hand side of Eq. (2.15) represents the linear response to the field at 2ω due to the other dipoles oscillating at 2ω and should be included to achieve self consistency.

The gradient of the local field in Eq. (2.16) is evaluated at the bonds and is proportional to the linear dipole moment which is given by

$$\nabla_i (\vec{\mathcal{E}}_{\ell\nu\lambda}(\omega))_j = -\sum_{\nu'\lambda'} (\overleftrightarrow{N}_{\ell\nu\lambda\ell'\nu'\lambda'})_{ijk} (\vec{p}_{\ell'\nu'\lambda'}(\omega))_k, \tag{2.19}$$

with the interaction tensor

$$\overleftrightarrow{N}_{\ell\nu\lambda\ell'\nu'\lambda'} = -\nabla\nabla\nabla \frac{1}{|\vec{r} - \vec{r}_{\ell'\nu'\lambda'}|}\bigg|_{\vec{r}=\vec{r}_{\ell\nu\lambda}}, \tag{2.20}$$

that decays quickly as the separation between planes increases. Similarly to Eq. (2.13), Eq. (2.15) can be written as

$$\sum_{\ell'\lambda'} [\vec{1}\delta_{\ell\ell'}\delta_{\lambda\lambda'} - \overleftrightarrow{\alpha}^{\ell\lambda}(2\omega) \cdot \overleftrightarrow{\mathcal{M}}_{\ell\lambda\ell'\lambda'}] \cdot \vec{p}^{\,tot}_{\ell'\lambda'}(2\omega) = \vec{\mathcal{S}}_{\ell\lambda}(2\omega), \tag{2.21}$$

where $\vec{\mathcal{S}}$ is the non-linear source given by

$$\begin{aligned}(\vec{\mathcal{S}}_{\ell\lambda}(2\omega))_i = \; & - \; \chi^{(\vec{d}),\ell\lambda}_{ijkl}(\vec{\mathcal{E}}_{\ell\lambda}(\omega))_j \sum_{\ell'\lambda'} (\mathcal{N}_{\ell\lambda\ell'\lambda'})_{klm}(\vec{p}_{\ell'\lambda'}(\omega))_m \\ & + \; \frac{1}{2}\alpha^{\ell\lambda}_{ij}(2\omega) \sum_{\ell'\lambda'} (\overleftrightarrow{\mathcal{N}}_{\ell\lambda\ell'\lambda'})_{jkl}\chi^{(Q),\ell'\lambda'}_{klmn}(\vec{\mathcal{E}}_{\ell'\lambda'}(\omega))_m(\vec{\mathcal{E}}_{\ell'\lambda'}(\omega))_n,\end{aligned} \tag{2.22}$$

which is expressed in terms of the linear dipole moment $\vec{p}_{\ell\lambda}(\omega)$ (see Eq. (2.13)). The linear local field $\vec{\mathcal{E}}_{\ell\lambda}(\omega)$ is obtained through the linear dipole moment as

$$\vec{\mathcal{E}}_{\ell\lambda}(\omega) = (\overleftrightarrow{\alpha}^{\lambda}(\omega))^{-1} \cdot \vec{p}_{\ell\lambda}(\omega). \tag{2.23}$$

Equation (2.21) gives the non-linear dipole moment of each dipole that is in the plane ℓ with orientation λ. Therefore, the total surface second-order dipole moment would be the sum of the contributions of all dipoles, i.e.

$$\vec{P}^{tot}(2\omega) = \sum_{\ell\lambda} \vec{p}^{\,(tot)}_{\ell\lambda}(2\omega). \tag{2.24}$$

Notice that, in principle, the sum in Eq. (2.24) is carried out over all dipoles in the system i.e, ℓ runs from $\ell = 0$ (from the surface) to $\ell \to \infty$ (to the bulk), however since the interaction tensor between surface dipoles with bulk dipoles decays quickly with plane separation, the source $\vec{\mathcal{S}}$ in Eq. (2.21) converges to a fixed value and thus, the total surface non-linear dipole moment $\vec{p}^{\,(tot)}_{\ell\lambda}(2\omega)$ as well. This means that we should only sum over a finite number of planes to get the total surface non-linear dipole moment.

On the other hand, we have to add the finite bulk contribution to the signal whose origin comes from the quadrupole moment [34], i.e.

$$P_i^{tot}(2\omega) \rightarrow P_i^{tot}(2\omega) - \frac{1}{2}\sum_{\lambda}(\overleftrightarrow{Q}_{\lambda}(B,2\omega))_{iz}, \tag{2.25}$$

with

$$(\overleftrightarrow{Q}_{\lambda}(B,2\omega))_{ij} = \chi_{ijkl}^{(Q),\lambda}(\vec{\mathcal{E}}(B,\omega))_k(\vec{\mathcal{E}}(B,\omega))_l \tag{2.26}$$

where $\vec{\mathcal{E}}(B,\omega)$ is the local field at the bulk.

Once the total polarization is obtained we could obtain the different susceptibility components by making use of the definition of the second order polarization Eq. (1.4). First, we fixed the external electric field $\vec{E}(A,\omega)$ in different directions; if $\vec{E}(A,\omega) = E_j(A,\omega)\hat{e}_j$, it would be possible to obtain χ_{izz}, χ_{iyy} and χ_{izz}, with $i = x, y$ or z, through

$$P_i^{tot} = \chi_{ijj}(\omega)E_j(B,\omega)E_j(B,\omega) \tag{2.27}$$

where $\vec{E}(B,\omega)$ is the macroscopic electric field inside the medium which differs from the external electric field $\vec{E}(A,\omega)$ through the equation

$$\vec{E}(B,\omega) = (E_x(A,\omega), E_y(A,\omega), E_z(A,\omega)/\varepsilon(\omega)) \tag{2.28}$$

with $\epsilon(\omega)$ the dielectric function. If now $\vec{E}(A,\omega)$ is let to have two no null components, namely, $E_j(A,\omega)$ and $E_k(A,\omega)$ with $j \neq k$, thus we have

$$P_i^{tot} = \chi_{ijj}E_j^2(B,\omega) + \chi_{ikk}E_k^2(B,\omega) + 2\chi_{ijk}E_j(B,\omega)E_k(B,\omega). \tag{2.29}$$

Knowing χ_{ijj} and χ_{ikk}, Eq. (2.29) can be solved for χ_{ijk}, generating the 27 components of $\overleftrightarrow{\chi}$. Indeed, some of these components would be identically zero due to the symmetry of the system. Then, the SHG efficiency $\mathcal{R}(\omega)$ can be calculated in terms of the non-linear susceptibilities, as explained in Sec. 2.3.

Once we have calculated the surface SHG, we have to add the bulk contribution to the surface SHG from a centrosymmetric medium. However, such a contribution is negligible (at least an order of magnitude smaller than the surface contribution) in media with large dielectric constant such as metals and semiconductors. Nevertheless the bulk contribution has been included in our results. For details of the bulk contribution to the SHG see Ref. [25].

2.2 Microscopic Methods

In the previous section, we presented a review of the phenomenological polarizable bond model that allowed us to get a physical understanding of the optical response of several systems in a very simple way.

A more realistic calculation of the SHG is obtained using a microscopic approach where the quantum mechanical theory is applied to obtain the electronic band structure of the system. This approach uses a linear combination of the atomic orbitals to construct the wave equation for a system of electrons, i.e. the wave function of each electron of the system is expanded in atomic wave functions which are centered at their atomic position. In the semi-empirical methods, the matrix elements of the one electron hamiltonian are parametrized and fitted in order to find, for instance, the bulk optical response in agreement with experiment. On the other hand, the *ab-initio* methods calculate the matrix elements from first principles where no adjustable parameters are required.

Several approaches have been developed to calculate the nonlinear optical response in this topic [78]. For semiconductor surfaces, a microscopic approach for the calculation of $\overleftrightarrow{\chi}$ was proposed by Cini [65] and adapted for a semiconductor surface by Reining *et al.* [51]. This method has the characteristic that within the same formalism one calculates the microscopic susceptibility and the radiated SH efficiency. We use a slab approach to mimic the semi-infinite system. The main steps taken to this purpose will be described. The key point is the calculation of the vector potential from which the non-linear radiated fields are calculated, and thus, the SHG yield is obtained through $\mathcal{R}$ of Eq. (1.14). The vector potential $\vec{A}(\vec{r},t)$ is given by [79]

$$A_i(\vec{r},t) = -\frac{1}{\hbar c}\int \mathrm{d}\vec{r}' \int_{-\infty}^{t} \mathrm{d}t' D_{ij}^{R}(\vec{r},t;\vec{r}',t')J_j(\vec{r}',t'), \tag{2.30}$$

where $\overleftrightarrow{D}^R$ is the retarded Green function appropriate for an interface [80], and $\vec{J}$ is the induced current. The interaction of the electron with the electromagnetic field is described through the perturbing scalar potential V, that within the Coulomb gauge is given by

$$V = -\frac{e}{mc}\vec{A}\cdot\vec{p} + \frac{e^2}{2mc^2}\vec{A}^2 \tag{2.31}$$

where $\vec{p}$ is the momentum operator of the electron, m is the mass and e is the charge. In the long wavelength approximation the term proportional to $\vec{A}^2$ cancels

identically [81]. Applying perturbation theory, the wave function to n-th order in V is given by

$$|\psi^{(n)}>=\frac{1}{(i\hbar)^n}\int_{-\infty}^{t}dt'\int_{-\infty}^{t'}dt''\cdots V_I(t')V_I(t'')\cdots|\psi^{(0)}>, \tag{2.32}$$

where the subscript I means that V is in the *interaction representation** and $\psi^{(0)}$ is the ground state wave function. To second-order, the induced current is given by

$$J_i=<\psi^{(0)}|\hat{J}_i|\psi^{(2)}>+<\psi^{(2)}|\hat{J}_i|\psi^{(0)}>+<\psi^{(1)}|\hat{J}_i|\psi^{(1)}>, \tag{2.33}$$

where $\hat{\vec{J}}$ is the quantum mechanical current operator [79]

$$\hat{\vec{J}}=\frac{e}{m}\hat{\vec{p}}-\frac{e^2}{mc}\vec{A}. \tag{2.34}$$

Substituting Eq. (2.32) and Eq. (2.34) into Eq. (2.33) and using $\vec{J}=\partial\vec{P}/\partial t$, where $P_i=\chi_{ijk}E_jE_k$ is the non-linear polarization, it is possible to obtain, within the long wavelength approximation, the imaginary part of the non-linear susceptibility as [27]

$$\begin{aligned}\Im m(\chi_{ijk}(\omega)) &= \frac{\pi n_0 e^4}{2Am^3\omega^3}\sum_{\xi}\sum_{r\in C}\sum_{s\in V}\\ &\left\{\sum_{n\in C}\left[\left(\frac{\mathcal{P}^i_{sn}P^j_{nr}P^k_{rs}}{E_{ns}-2E_{rs}}+\frac{P^j_{sn}\mathcal{P}^i_{nr}P^k_{rs}}{E_{ns}+E_{rs}}\right)\delta(E_{rs}-\hbar\omega)\right.\right.\\ &\left.\left.-2\frac{\mathcal{P}^i_{sn}P^j_{nr}P^k_{rs}}{E_{ns}-2E_{rs}}\delta(E_{ns}-2\hbar\omega)\right]\right.\end{aligned} \tag{2.35}$$

*In the *interaction representation* the time dependence of the system is partly transferred to the operators while the wavefunctions varies slowly. Let the hamiltonian be of the form $\hat{\mathcal{H}}=\hat{\mathcal{H}}_0+\hat{V}(t)$, where $\hat{\mathcal{H}}_0$ is the hamiltonian of the time independent non-perturbed system and $\hat{V}(t)$ is the perturbation. If $\hat{L}$ is the operator of an arbitrary physical quantity and $\psi(t)$ the time dependent wave function, then in the interaction picture we have

$$\begin{aligned}L_I &= \exp(\tfrac{i}{\hbar}\hat{\mathcal{H}}_0t)\hat{L}\exp(-\tfrac{i}{\hbar}\hat{\mathcal{H}}_0t),\\ \psi_I &= \exp(-\tfrac{i}{\hbar}\hat{\mathcal{H}}_0t)\psi(t).\end{aligned}$$

$$-\sum_{m\in V}\left[\left(\frac{\mathcal{P}^i_{mr}P^j_{sm}P^k_{rs}}{E_{rm}-2E_{rs}}+\frac{P^j_{mr}\mathcal{P}^i_{sm}P^k_{rs}}{E_{rm}+E_{rs}}\right)\delta(E_{rs}-\hbar\omega)\right.$$
$$\left.-2\frac{\mathcal{P}^i_{mr}P^j_{sm}P^k_{rs}}{E_{rm}-2E_{rs}}\delta(E_{rm}-2\hbar\omega)\right]\Bigg\},$$

where n_0 is the electron density, and $P^i_{sn}(\vec{k})$ is the matrix element of the i-Cartesian component of the momentum operator between states s and n, which may be valence (V), or conduction (C) states at point $\vec{k}$ in the two-dimensional Brillouin zone (2DBZ), A is the sample area,

$$E_{nr}=E_n(\vec{k})-E_r(\vec{k}), \tag{2.36}$$

with $E_n(\vec{k})$ the one-electron energy. We remark that Eq. (2.35) must be symmetrized in the last two indices (jk) in order to comply with the intrinsic permutation symmetry of $\overleftrightarrow{\chi}$. Figure 2.1 shows a sketch of the different transitions corresponding to each of the four terms of Eq. (2.35).

The fundamental electric field $\vec{E}(\omega)$ oscillating at ω, given by $\vec{E}(\omega)=i\omega/c\vec{A}(\omega)$, which induces the non-linear response, is taken to be inside the surface. In particular, this field is simply given by the external field properly multiplied by the corresponding Fresnel factors [51]. A more detailed description of the fields, which incorporates the spatial variation of the dielectric function near the surface within the three-layer model (see Sec. 2.3, shows no change in the SHG peak positions and only a slight difference in their intensity, as we will show in Chapter 5. However a full treatment of the surface screening is still missing, and further improvement of the present formulation can be made at this point. This screening will presumably affect more the zzz component of $\overleftrightarrow{\chi}$ than any other component, although it is not at all trivial to anticipate what the actual effect will be. Therefore we explain the results within the framework of our formalism. Also, at the present stage of the calculations for non-linear optical properties of semiconductor surfaces, like the one presented here, local-field and excitonic effects are still beyond current capabilities and are thus neglected throughout. Again, these effects along with the surface screening will prove to be crucial for a quantitative comparison between theory and experiment.

In order to describe the semi-infinite crystal we use a slab of N layers. The slab brings about the complication that such a system is intrinsically centrosymmetric.

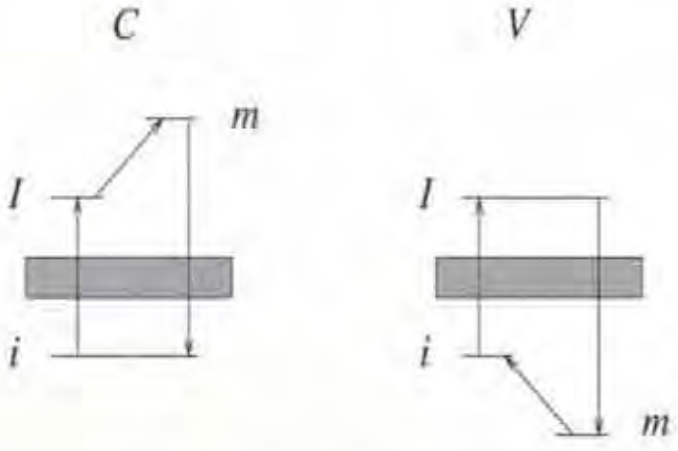

Figure 2.1: We sketch the two different transitions processes that contribute to SHG through Eq. (2.35). The shaded rectangle represents the energy gap. Here, i is the initial state always in the valence (V) band, I is the intermediate state always in the conduction (C) band, and m is the virtual state which could be in the conduction or valence band.

Therefore in order to describe the emission of SH light, we introduce the modified momentum operator

$$\vec{\mathcal{P}} = \frac{S(z)\vec{P} + \vec{P}S(z)}{2}, \tag{2.37}$$

where $\vec{P} = -i\hbar\vec{\nabla}$ is the usual momentum operator, and $S(z)$ is a function of z, being 1 at the front surface and 0 at the back surface. This function allows us to avoid the spurious destructive interference of SH light generated at the two surfaces of the slab.

2.2.1 The semi-empirical tight-binding method

In the tight-binding (TB) method each atom is associated with a finite set of orbitals, or atomic basis states, each of which can be occupied by two electrons, and is well documented in the condensed matter literature, see for instance [82,83]. To describe the bonding in silicon a minimal sp^3 basis is requiered consisting of

one s orbital and three p orbitals for each atom [84]. However attempts to fit the conduction bands of semiconductors with a nearest-neighbor sp^3 basis failed. To overcome this deficiency Vogl *et al.* [85] included an excited s state, s^*, on each atom, giving an sp^3s^* basis, with which the bulk optical properties could be fitted. The inclusion of various excited states (including the d states [86]) would obtain the correct band structure, but it would be still semiempirical and computationally more intensive. Thus, we use the simple sp^3s^* basis for the SETB approach, that has the advantage of being less computationally intensive than the other basis or *ab-initio* methods.

Based on previous formalism, and within a sp^3s^* basis set, Reining *et al.* [51] calculated the SHG of the As-covered Si(111) surface, and Gravrilenko and Rebentrost showed that qualitatively correct predictions of the non-linear optical response of both reconstructed and unreconstructed clean semiconductor surfaces could be obtained [52, 53]. Mendoza *et al.* [27] have calculated the surface SHG from clean and H-covered Si(100). Their microscopic calculation showed that the bulk E_1 resonance occurs in surface SHG spectra through electronic transitions across surface-perturbed bulk states, that H adsorption modifies the SHG lineshape by reducing the E_1 resonance and suppressing the spectral structures due to transitions across surface states and that, contrary to what may be argued, the $\chi_{\perp\perp\perp}$ component of the second-order surface susceptibility does not dominate the SHG signal. Instead, they found that the $\chi_{\parallel\parallel\perp}$ component of the second-order surface susceptibility is mostly responsible for the observed features. Therefore, it is the inter-play of both in-plane and perpendicular components of $\overleftrightarrow{\chi}$ that gives rise to the SH response. In this thesis we use the method followed above, which gives relaiable results for the SHG of Si surfaces.

2.2.2 *Ab-initio* Method

As in the former subsection, the key ingredient of the *ab-initio* method is $\overleftrightarrow{\chi}$ as defined in the Eq. (2.35), where the eigenenergies and wavefunctions used in the calculation of the momentum matrix elements are calculated from first principles. For this we use the well known density-functional theory within the local-density approximation (DFT-LDA) of Kohn and Sham [87], within which we calculate the non-linear optical properties of our surfaces.

For the *ab-initio* method the calculation of the $\vec{\mathcal{P}}$ matrix elements of Eq. (2.37) is computationally heavier than that of $\vec{P}$ matrix elements in a plane-wave basis,

since $\vec{P}$ is diagonal therein, while $\vec{\mathcal{P}}$ is not. To overcome this problem, the matrix elements of $\vec{\mathcal{P}}$, required in Eq. (2.35), are calculated according to Eq. (2.37) as

$$\vec{\mathcal{P}}_{mn} = \frac{1}{2}\sum_{s}(S_{ms}\vec{P}_{sn} + \vec{P}_{ms}S_{sn}), \tag{2.38}$$

where the completeness relation for the states of the slab has been used. Expanding the wavefunctions as

$$\psi_{n\vec{k}}(\vec{r}) = \sum_{\vec{G}} c_{n\vec{G}}(\vec{k})\exp[i(\vec{k}+\vec{G})\cdot\vec{r}], \tag{2.39}$$

where all plane waves up to a cutoff of 15 Rydberg are included, it is straightforward to obtain that

$$S_{mn} = \sum_{\vec{G}\vec{G}'} c^{*}_{m\vec{G}'}(\vec{k})c_{n\vec{G}}(\vec{k})\delta_{\vec{G}_{\parallel}\vec{G}'_{\parallel}} f(g-g'), \tag{2.40}$$

with

$$f(g) = \int_0^d dz S(z)e^{-igz}. \tag{2.41}$$

Here, $\vec{G} = \vec{G}_{\parallel} + g\hat{z}$, are the vectors of the reciprocal lattice, and d is the slab periodicity. As in the SETB scheme, for $S(z)$ we have used a step function centered at the middle of the slab. Using smoother functions yields the same SHG lineshape with only small changes in the absolute magnitude of $\mathcal{R}$ [51].

The *ab-initio* DFT-LDA calculation of the optical properties of solids produces gaps which are smaller than the experimental ones by about $\sim$ 0.5-1 eV in semiconductors, leading to redshifted spectra [88]. In principle, one should use a many-body formalism to improve beyond DFT-LDA [89–92]. In practice one has to consider an effective single-quasiparticle (QP) Hamiltonian, where self-energy effects are described according to Hedin's GW approximation [93] and the electron-hole interaction is neglected. The effect of the QP corrections on the linear optical spectra of semiconductors can be calculated by assuming nearly identical DFT-LDA and QP wave functions, and by following the next two steps due to Del Sole and Girlanda [94]: firstly the LDA energies $E_n(\vec{k})$ are shifted by $\Delta_n(\vec{k})$, and secondly the momentum matrix elements $\vec{P}_{mn}$ are renormalized according to

$$\vec{P}^{\text{eff}}_{mn} = \vec{P}_{mn}\frac{E_m(\vec{k}) + \Delta_m(\vec{k}) - E_n(\vec{k}) - \Delta_n(\vec{k})}{E_m(\vec{k}) - E_n(\vec{k})}. \tag{2.42}$$

We use the scissors-operator approximation, used in Ref. 95 for the calculation of the linear optical response (bulk) of Si and Ge, in which the conduction bands are rigidly upward shifted by a constant $\Delta_n(\vec{k}) = \Delta$ with respect to the valence bands. In Eq. (2.35) we replace $E_n(\vec{k}) \to E_n(\vec{k}) + \Delta$ if n is a conduction (C) state, and replace the C-valence(V) matrix elements of $\vec{P}$, by

$$\vec{P}^{\text{eff}}_{CV} = \vec{P}_{CV} \frac{E_C(\vec{k}) - E_V(\vec{k}) + \Delta}{E_C(\vec{k}) - E_V(\vec{k})}. \tag{2.43}$$

This renormalization stems from the non-local character of the self-energy. If the scissors-operator approximation is used without renormalizing the optical matrix elements according to Eq. (2.35), spectral intensities and dielectric constants are underestimated by about 30 percent in Si [95]. This procedure has recently been applied also to the calculation of bulk SHG spectra in III-IV compounds [96].

2.3 SHG Radiation

In this section we derive the formulas required for the calculation of the SHG yield, defined in Eq. (1.15). There are several ways to calculate $\mathcal{R}$, one of which is the procedure followed by Cini [65]. This approach calculates the non-linear susceptibility given in Eq. (2.35), and at the same time the radiated fields. However, we present an alternative derivation based in the work of Mizrahi and Sipe [47], since it is more straightforward and in a sense of shorter derivation. The final results are the same, regardless of the approach used.

Within our level of approximation, the best model that we can use, is the so called three-layer-model, where we assume that the SH conversion takes place in a thin layer, just below the surface, that is characterized by a surface dielectric function $\epsilon_\ell(\omega)$. This layer is below vacuum and sits on top of the bulk characterized by $\epsilon_b(\omega)$ (see Fig. 2.2). The non-linear polarization immersed in the thin layer, will radiate an electric field directly into vacuum and also into the bulk. This bulk directed field, will be reflected back into vacuum. Thus, the total field radiated into vacuum will be the sum of these two contributions (see Fig. 2.2). We decompose the field into s and p polarizations, then from Ref. [47], the electric field radiated by a polarization sheet, $\mathcal{P}_i = \chi_{ijk} E_j(\omega) E_k(\omega)$, is given by

$$E_{s\pm} = \frac{2\pi i \tilde{\omega}^2}{w} \tilde{s} \cdot \vec{\mathcal{P}}, \tag{2.44}$$

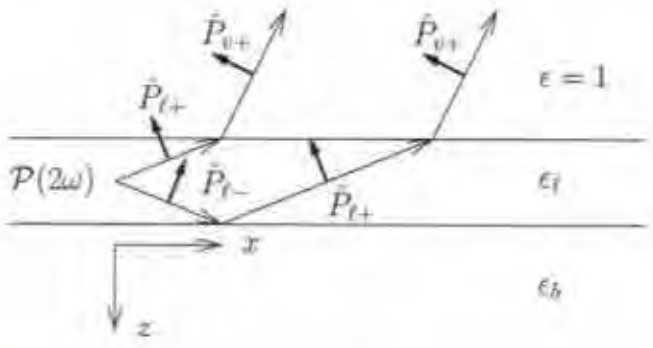

Figure 2.2: Sketch of the three layer model for SHG. Vacuum is on top with $\epsilon = 1$, the layer with non-linear polarization $\mathcal{P}$ is characterized with ϵ_ℓ, and the bulk, where in the dipolar approximation does not radiate SHG, with $\epsilon_b(\omega)$. The thin arrows are along the direction of propagation, and the unit vectors for p-polarization are denoted with thick arrows. The unit vector for s-polarization points along y (out of the page).

and

$$E_{p\pm} = \frac{2\pi i\tilde{\omega}^2}{w}\hat{p}\cdot\vec{\mathcal{P}}, \tag{2.45}$$

where $\hat{s}$ and $\hat{p}$ are the unitary vectors for s and p polarization, respectively, and the $\pm$ refers to upward $(+)$ or downward $(-)$ direction of propagation. Also, $\tilde{\omega} = \omega/c$ and $w = \tilde{\omega}k_z$, with

$$k_z(\omega) = \sqrt{\epsilon(\omega) - \sin^2\theta}, \tag{2.46}$$

and $\hat{p}_\pm = \vec{p}/\sqrt{\epsilon}$, with

$$\vec{p} = \mp k_z\hat{x} - \sin\theta\hat{z}. \tag{2.47}$$

In the above equations z is the direction perpendicular to the surface that points towards the bulk, x is parallel to the surface, and θ is the angle of incidence, where the plane of incidence is chosen as the xz plane (see Fig. 2.2), thus $\hat{s} = \hat{y}$. The function $k_z(\omega)$ is the projection of the wave vector perpendicular to the surface. As we see from Fig. 2.2, the SH field is refracted at the layer-vacuum interface, and reflected from the layer-bulk interface, thus we can define the transmission,

$\overleftrightarrow{T}$, and refraction, $\overleftrightarrow{R}$, tensors as,

$$\overleftrightarrow{T}_{\ell v} = \hat{s} T_s^{\ell v} \hat{s} + \hat{P}_{v+} \tilde{T}_p^{\ell v} \hat{P}_{\ell+}, \tag{2.48}$$

and

$$\overleftrightarrow{R}_{\ell b} = \hat{s} R_s^{\ell b} \hat{s} + \hat{P}_{\ell+} R_p^{\ell b} \hat{P}_{\ell-}, \tag{2.49}$$

where variables in capital letters are evaluated at the harmonic frequency 2ω. Notice that since $\tilde{s}$ is independent of ω, then $\hat{S} = \tilde{s}$. The Fresnel factors, T_i, R_i, and $\tilde{T}_p$, for $i = s, p$ polarization, are evaluated at the appropriate interface ℓv or ℓb, and will be given below. The subscript in $\hat{P}$ denotes the corresponding dielectric function to be used in its evaluation, i.e. $\epsilon_v = 1$ for vacuum (v), ϵ_ℓ for the layer (ℓ), and ϵ_b for the bulk (b). Therefore, the total radiated field at 2ω is

$$\begin{aligned} \vec{E}(2\omega) &= E_s(2\omega) \left(\overleftrightarrow{T}_{\ell v} + \overleftrightarrow{R}_{\ell b} \cdot \overleftrightarrow{T}_{\ell v} \right) \cdot \tilde{s} \\ &+ E_{p+}(2\omega) \overleftrightarrow{T}_{\ell v} \cdot \hat{P}_{\ell+} + E_{p-}(2\omega) \overleftrightarrow{T}_{\ell v} \cdot \overleftrightarrow{R}_{\ell b} \cdot \hat{P}_{\ell-}. \end{aligned} \tag{2.50}$$

The first term is the transmitted s-polarized field, the second one is the reflected and then transmitted s-polarized field and the third and fourth terms are the equivalent fields for p-polarization. The transmission is from the layer into vacuum, and the reflection between the layer and the bulk. After some simple algebra, we obtain

$$\vec{E}(2\omega) = \frac{4\pi i \tilde{\omega}}{K_{z\ell}} \overleftrightarrow{H} \cdot \vec{\mathcal{P}}, \tag{2.51}$$

where,

$$\overleftrightarrow{H} = \hat{s} T_s^{\ell v} \left(1 + R_s^{\ell b} \right) \hat{s} + \hat{P}_{v+} \tilde{T}_p^{\ell v} \left(\hat{P}_{\ell+} + R_p^{\ell b} \hat{P}_{\ell-} \right). \tag{2.52}$$

The magnitude of the radiated field is given by $E(2\omega) = \tilde{e}^{out} \cdot \vec{E}(2\omega)$, where $\tilde{e}^{out}$ is the polarization vector of the radiated field, for instance $\tilde{s}$ or $\hat{P}_{v+}$. Then we write

$$E(2\omega) = \frac{4\pi i \omega}{c} \vec{e}^{2\omega} \cdot \vec{\mathcal{P}}. \tag{2.53}$$

Using the above equations and the following simple relationships between T and R,

$$T_s^{\ell v} = \frac{K_{z\ell}}{\cos\theta} T_s^{v\ell}, \tag{2.54}$$

$$\tilde{T}_p^{\ell v} = \frac{\sqrt{\epsilon_\ell(2\omega)}K_{z\ell}}{\cos\theta} T_p^{v\ell}, \tag{2.55}$$

$$1 - R_p^{\ell b} = \frac{\epsilon_\ell(2\omega)K_{zb}}{K_{z\ell}} T_p^{\ell b}, \tag{2.56}$$

$$1 + R_p^{\ell b} = \epsilon_b(2\omega)T_p^{\ell b}, \tag{2.57}$$

we obtain

$$\vec{e}^{\,2\omega} = \frac{1}{\cos\theta}\vec{e}^{\,out} \cdot \left[\hat{s}T_s^{v\ell}T_s^{\ell b}\hat{s} - \hat{P}_{v+}T_p^{v\ell}T_p^{\ell b}\left(\epsilon_\ell(2\omega)K_{zb}\hat{x} + \epsilon_b(2\omega)\sin\theta\hat{z}\right)\right] \tag{2.58}$$

and then we write from Eq. (2.53)

$$E_s(2\omega) = \frac{4\pi i\omega}{c}\frac{1}{\cos\theta}T_s^{v\ell}T_s^{\ell b}\chi_{yij}E_i(\omega)E_j(\omega), \tag{2.59}$$

and

$$E_p(2\omega) = -\frac{4\pi i\omega}{c}\frac{1}{\cos\theta}T_p^{v\ell}T_p^{\ell b}\left[\epsilon_\ell(2\omega)K_{zb}\chi_{xij} + \epsilon_b(2\omega)\sin\theta\chi_{zij}\right]E_i(\omega)E_j(\omega). \tag{2.60}$$

As mentioned before $E_i(\omega)$ is the incident field, given by the external field properly screened, then we have

$$\vec{E}_s(\omega) = E_o t_s^{v\ell}\left(1 + r_s^{\ell b}\right)\hat{y}, \tag{2.61}$$

and

$$\vec{E}_p(\omega) = E_o\left[\tilde{t}_p^{v\ell}\left(1 - r_p^{\ell b}\right)\cos\theta_\ell\hat{x} - \tilde{t}_p^{v\ell}\left(1 + r_p^{\ell b}\right)\sin\theta_\ell\hat{z}\right], \tag{2.62}$$

where E_o is the incoming intensity and θ_ℓ is the angle of refraction in the layer. Notice that the transmitted and reflected fields in the layer are taken into $\vec{E}_s$ and $\vec{E}_p$. Using Eqs. (2.54)-(2.57) we get

$$\vec{E}_s(\omega) = E_o t_s^{v\ell}t_s^{\ell b}\hat{y}, \tag{2.63}$$

and

$$\vec{E}_p(\omega) = E_o t_p^{v\ell}t_p^{\ell b}\left(\epsilon_\ell(\omega)k_{zb}\hat{x} - \epsilon_b(\omega)\sin\theta\hat{z}\right). \tag{2.64}$$

Using Eqs. (2.59), (2.60), (2.63), (2.64), into Eq. (1.15) for $\mathcal{R}$, we finally write

$$\mathcal{R}_{iF} = \frac{32\pi^3\omega^2}{(n_o e)^2 c^3\cos^2\theta}\left|T_F^{v\ell}T_F^{\ell b}(t_i^{v\ell}t_i^{\ell b})^2\, r_{iF}\right|^2, \tag{2.65}$$

where i (lower case) stands for initial polarization and F (upper case) stands for final polarization, and

$$r_{iP} = \left(K_{zb}\chi_{xjk} + \sin\theta\chi_{zjk}\right)\mathcal{E}_j^i\mathcal{E}_k^l, \tag{2.66}$$

and

$$r_{iS} = \chi_{yjk}\mathcal{E}_j^i\mathcal{E}_k^l, \tag{2.67}$$

where from Eqs. (2.63)-(2.64),

$$\vec{\mathcal{E}}^s = \hat{y}, \tag{2.68}$$

and

$$\vec{\mathcal{E}}^p = \epsilon_\ell(\omega)k_{zb}\hat{x} - \epsilon_b(\omega)\sin\theta\hat{z}. \tag{2.69}$$

The $n_o e$ factor in Eq. (2.65), with n_o the electronic density, renders $\overleftrightarrow{\chi}$ dimensionless, so to get $\overleftrightarrow{\chi}$ with proper units of distance cube over charge we multiply it by $1/n_o e$. To complete the required formulas, we write down the Fresnel factors,

$$t_s^{v\ell} = \frac{2\cos\theta}{\cos\theta + k_{z\ell}}, \tag{2.70}$$

$$t_p^{v\ell} = \frac{2\cos\theta}{\epsilon_\ell(\omega)\cos\theta + k_{z\ell}}, \tag{2.71}$$

$$t_s^{\ell b} = \frac{2k_{z\ell}}{k_{z\ell} + k_{zb}}, \tag{2.72}$$

and

$$t_p^{\ell b} = \frac{2k_{z\ell}}{\epsilon_b(\omega)k_{z\ell} + \epsilon_s(\omega)k_{zb}}, \tag{2.73}$$

where the appropriate term $\sqrt{\epsilon(\omega)}$ from the usual definition of t_p [97] has been taken out to give Eqs. (2.66) and (2.67).

With the three-layer model we can get two opposite cases, one in which the SH conversion takes places in vacuum for which we simply put $\epsilon_\ell = 1$ in the above formulas, and the other case where the layer is identical to the bulk, or $\epsilon_\ell = \epsilon_b$. The former case corresponds to no screening and the latter to the usual Fresnel screening.

For a given surface symmetry and its corresponding non-zero tensor elements of χ_{ijk}, Eq. (2.65) can be calculated explicitly through Eqs. (2.66) and (2.67). The explicit formulas will be presented in the following Chapters.

Chapter 3

Single-domain Si(100) surfaces

3.1 Introduction

In this Chapter, we apply a microscopic formulation based on the semi-empirical tight-binding (SETB) method to calculate the second harmonic spectra of a clean single-domain Si(100)c(4 × 2) surface.

The SETB method has also been frequently and successfully employed to study the linear optical properties of semiconductor surfaces [98–100]. In particular we mention that the linear optical results for several Si(100) surface reconstructions have been compared with *ab initio* methods by Palummo *et al.* [101]. They analyzed two optical probes, reflectance anisotropy spectroscopy (RAS) and surface differential reflectivity (SDR). The conclusion of this work was that due to the omission of second-neighbor interactions in the SETB scheme, the RAS signal has the wrong sign for the low energy structures, but for the rest of the spectra there is a one to one correspondence between SETB and *ab initio* structures. On the other hand, the SDR spectrum being an average over two perpendicular polarizations depends less critically on the theoretical scheme used, and thus SETB and *ab initio* SDR agree rather well. Palummo *et al.* [101] calculated RAS and SDR spectra for Si(100)c(4 × 2) surface confirming the aforementioned behavior. However, the *ab initio* spectra have some surface features at low energy not shown by the SETB calculation. A similar comparison between SETB and *ab initio* SHG calculations shows that for Si(100)c(4 × 2) the spectra basically agree above 2 eV in the two-photon energy [32].

The atomic structure of a clean Si(100) surface is formed by asymmetric buckled surface dimers [102]. If the dimers are only oriented along the [01$\bar{1}$] direction then the surface is reconstructed in a 2×1 surface. On the other hand, if the orientation of the buckling angles also alternates perpendicularly to the rows the arrangement leads to a c(4×2) reconstruction, which is the ground state of the Si(100) surface at low temperature [103]. Depending on surface treatment, one can have either singular or vicinal Si(100) surfaces [15]. For a singular or double-domain surface there are equal populations of dimer domains where the orientation of the dimers changes by 90° from one domain to the other. Vicinal surfaces have predominantly single-domain terraces with only one orientation for the dimers. The terraces in single-domain surfaces are separated by inherent (double-height) steps. These steps could play a major role in SHG. As shown by Power et al. [15] the terraces seem to play only a marginal role in their measured spectra of vicinal Si(100) and Si(100)-Sb surfaces around E_1. Although the phenomenological modeling for SHG from vicinal surfaces has been presented by Lüpke et al. [104], the microscopic theoretical calculation of the susceptibilities involved in SHG for such step-terrace structures is beyond current capabilities. However, microscopic theoretical calculations of SHG within the semi-empirical tight-binding (SETB) method [21,27,30,31] or *ab-initio* schemes [21,29,30,32] for double-domain Si(100) with different reconstructions and adsorbate coverage, have been successfully compared with experiments. A comparison between SETB and *ab-initio* SHG calculations shows that for Si(100)c(4×2) the spectra agree above 2 eV and below 5.5 eV in the two-photon energy [32]. Also, these two methods have been used successfully to study boron and hydrogen covered Si(100) surfaces [21,30].

Here, we apply the SETB method of Ref. [27] to study the SHG spectra of a clean single-domain Si(100)c(4×2) surface. According to Höfer [105], it is possible by selective H doping to passivate the steps of vicinal surfaces, leaving only the terraces as active SHG sources, thus creating clean single-domain Si(100) surfaces.

In Sec. 3.2 we mention the preliminary considerations to calculate the SHG efficiency $\mathcal{R}$ through the nonlinear susceptibility tensor $\overleftrightarrow{\chi}$. In Sec. 3.3 we present the spectra for a Si(100)c(4×2) surface, analyzing in particular the E_1 SHG resonance. Finally, in Sec. 3.4, we summarize our results and give conclusions.

symmetry class	location of mirror plane	components
C_{1v}	$\hat{x}-\hat{z}$	χ_{yyx}, χ_{xyy}, χ_{xxx}, χ_{yyz}, χ_{xxz}, χ_{zxx}, χ_{zyy}, χ_{xzz}, χ_{zzx}, χ_{zzz}
C_{2v}	$\hat{x}-\hat{z},\hat{y}-\hat{z}$	χ_{xxz}, χ_{yyz}, χ_{zxx}, χ_{zyy},χ_{zzz}
C_{4v} or isotropic	$\hat{x}-\hat{z},\hat{y}-\hat{z}$	$\chi_{xxz}=\chi_{yyz}$, $\chi_{zxx}=\chi_{zyy}$,χ_{zzz}

Table 3.1: The independent nonvanishing components of $\overleftrightarrow{\chi}$ for the different symmetry classes. The intrinsic symmetry $\chi_{ijk}=\chi_{ikj}$ is satisfied by the corresponding components.

3.2 Preliminary Considerations

The reflected SHG efficiency $\mathcal{R}$ is calculated through the second-order surface susceptibility tensor $\overleftrightarrow{\chi}$. But first we have to analyze the symmetry properties of the single-domain surface in question. Considering only the dimers, they would form a surface with a C_{2v} symmetry, however as the atoms in the underneath layers are included the mirror plane perpendicular to the dimers no longer exists, and the symmetry is reduced to a C_{1v} with only one mirror plane parallel to the dimers (see Fig. 3.1). For a double-domain surface the symmetry is C_{4v} which is an isotropic surface. In Table 3.1 we give the independent nonvanishing components of $\overleftrightarrow{\chi}$ for the different symmetry classes, where x (y) is parallel (perpendicular) to the dimers. We define as anisotropic components of $\overleftrightarrow{\chi}$, those which are zero for the isotropic C_{4v} or C_{2v} symmetry, i.e. xxx, yyx, xyy, xzz and zxz. However, for the C_{2v} the $xxz \neq yyz$, and $zxx \neq zyy$ also give rise to anisotropy in the $\mathcal{R}$ signal.

To investigate the C_{1v} or C_{2v} surface non-linear optical anisotropy, we have to study the azimuthal dependence of $\mathcal{R}$. Toward this end, $\overleftrightarrow{\chi}$ is calculated on the fixed axes of the dimer and then rotated so the new x' direction is along the

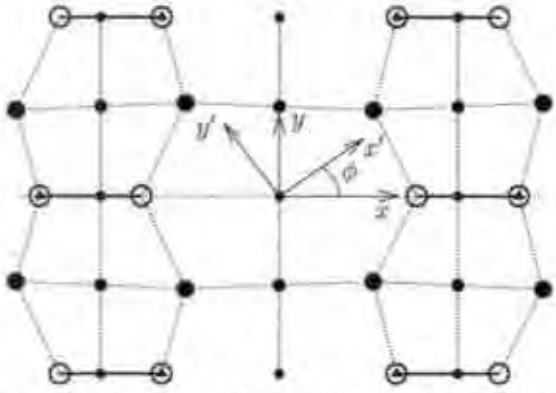

Figure 3.1: We show the top view of the Si(100)c(4 × 2) surface. The dimers are denoted by a solid line and atoms by open circles, where the triangle gives the top atom. The atoms below the dimer up to three layers are shown by solid circles of diminishing size. The dotted line represents the bonds connecting these atoms. Notice a plane of mirror symmetry parallel to the dimers. Perpendicular to them no mirror plane exists due to the underlying atoms. The coordinate axes and the azimuthal angle ϕ are shown for reference.

incident plane of the fundamental beam (see Fig. 3.1). Then,

$$\chi_{i'j'k'} = R_{i'i}R_{j'j}R_{k'k}\chi_{ijk}, \tag{3.1}$$

with

$$R = \begin{pmatrix} \cos\phi & \sin\phi & 0 \\ -\sin\phi & \cos\phi & 0 \\ 0 & 0 & 1 \end{pmatrix}, \tag{3.2}$$

where ϕ is the azimuthal angle. It is then straightforward to follow Sec. 2.3 in order to obtain, for a fundamental i-polarized beam, the f-polarized SH output for a surface with a C_{1v} symmetry as

$$\mathcal{R}_{if} = \frac{32\pi^3}{(n_0 e)^2 c^3}\frac{\omega^2}{\cos^2\theta}|T_f(2\omega)T_i^2(\omega)r_{if}|^2, \tag{3.3}$$

where $i = s$ or p indicates the s-polarization or p-polarization of the incoming photon of frequency ω, respectively, and $f = S$ or P the s-polarization or p-polarization of the outgoing photon of frequency 2ω, respectively. Here,

$$r_{pP} = k_z(\omega)\sin\theta\,[k_z(\omega)\chi_{zzz} - 2k_z(2\omega)\chi_{xxz}]\cos^2\phi$$

$$
\begin{aligned}
&+ \; k_z(\omega)^2 k_z(2\omega)\chi_{zzz}\cos^3\phi \\
&+ \; \left[\sin^2\theta\,[k_z(2\omega)\chi_{zzz} - 2k_z(\omega)\chi_{xxz}]\right. \\
&+ \; \left. k_z(\omega)^2 k_z(2\omega)\,[\chi_{xyy} + 2\chi_{yyz}]\sin^2\phi\right]\cos\phi \\
&+ \; \sin\theta\left[\sin^2\theta\chi_{zzz} + k_z(\omega)\,[k_z(\omega)\chi_{zyy} - 2k_z(2\omega)\chi_{yyz}]\sin^2\phi\right], \qquad (3.4a)
\end{aligned}
$$

$$
\begin{aligned}
r_{sP} \;&=\; \chi_{zyy}\sin\theta\cos^2\phi + k_z(2\omega)\chi_{xyy}\cos^3\phi + \chi_{zzz}\sin\theta\sin^2\phi \\
&+\; k_z(2\omega)\,[\chi_{xxz} - 2\chi_{yyz}]\cos\phi\sin^2\phi, \qquad (3.4b)
\end{aligned}
$$

$$
\begin{aligned}
r_{pS} \;&=\; k_z(2\omega)\left[\sin^2\theta\chi_{zzz} - 2k_z(\omega)\sin\theta\,[\chi_{xxz} - \chi_{yyz}]\cos\phi\right. \\
&+\; \left. k_z(\omega)^2\,[\chi_{xxz} - 2\chi_{yyz}]\cos^2\phi + k_z(\omega)\chi_{xyy}\sin^2\phi\right]\sin\phi, \qquad (3.4c)
\end{aligned}
$$

and

$$
r_{sS} \;=\; k_z(2\omega)\left[[\chi_{xyy} + 2\chi_{yyz}]\cos^2\phi + \chi_{zzz}\sin^2\phi\right]\sin\phi. \qquad (3.4d)
$$

In the equations above, θ is the angle of incidence, c the speed of light, e the electron charge, n_0 the electron density of the system, and $k_\perp = (\epsilon(\omega) - \sin^2\theta)^{1/2}$, with $\epsilon(\omega)$ being the bulk dielectric function. We recognize that above formulas are valid for the Fresnel screening of the fields, i.e. using $\epsilon_f = \epsilon$ in Sec. 2.3. The transmission Fresnel factors are given in Sec. 2.3. Note that all non-zero components of $\overleftrightarrow{\chi}$ contribute to $\mathcal{R}_{pP}$. Eqs. (3.4) are strictly valid within the dipole approximation. Notice that if one takes the C_{4v} symmetry, one recovers from Eqs. (3.4) the usual expressions for an isotropic surface given in Ref. [27], where $r_{iS} = 0$.

It is also possible to obtain $\mathcal{R}$ for the case of an arbitrarily polarized incident field $\vec{E}^{in}$. For instance we can consider a field whose polarization is a linear combination of p and s polarization. If α is the angle of the incident field with respect to the direction of the p-polarized field $\vec{E}_p$, then $\vec{E}^{in} = \vec{E}_s\sin\alpha + \vec{E}_p\cos\alpha$. Note that for $\alpha = 90°$ ($\alpha = 0°$) $\vec{E}^{in} = \vec{E}_s$ ($\vec{E}^{in} = \vec{E}_p$), i.e. s (p) polarization. For $\alpha = 45°$ we have what is known as q-polarization. As shown in Ref. [15], q-polarization and the variation of $\mathcal{R}$ with α, gives crucial information on the symmetry properties of vicinal Si(100) clean 1×2, 1×2-Sb and 2×1-Sb surfaces.

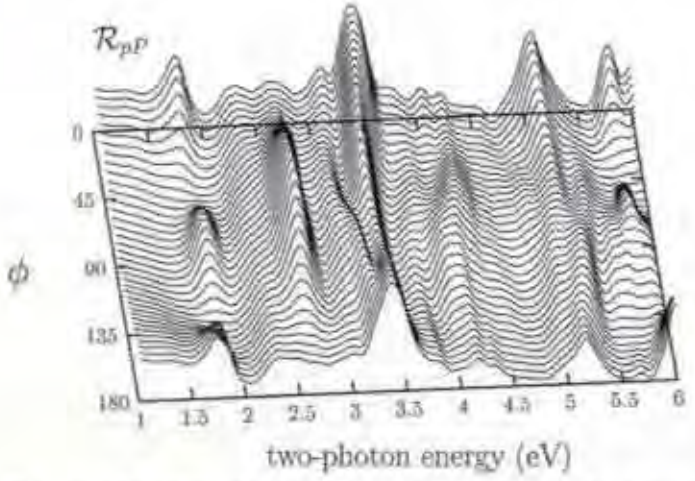

Figure 3.2: $\mathcal{R}_{pp}$ as a function of the two-photon energy and the azimuthal angle ϕ for a single-domain Si(100)c(4 × 2) clean surface. The angle of incidence is 45° and the maximum intensity is 4.2×10^{-18} W/cm^2 for $2\hbar\omega = 2.60$ eV.

The corresponding expressions for $\mathcal{R}_{ij}$ when $i = q$ are too cumbersome to be presented here.

The key step is the calculation of $\overleftrightarrow{\chi}$. Therefore, following Ref. [51], we substitute in the Eq. (2.35) to obtain the imaginary part of the single-domain second-order surface susceptibility. We consider a slab consisting of N atomic (100) layers, and use the same coordinates as those in Ref. [27]. These were obtained with total energy minimization, according to the density functional theory within the local density approximation (DFT-LDA), for a c(4 × 2) supercell [106]. The sum over $\vec{k}$ of Eq. (2.35) is usually carried out over only one quarter of the irreducible part of the 2DBZ, since the components of $\overleftrightarrow{\chi}$ of highest symmetry (i.e. isotropic surface of Table 3.1), are even functions of $\vec{k}$. However, this fact is no longer true for the anisotropic components of $\overleftrightarrow{\chi}$ for the C_{1v} symmetry, and thus the summation over $\vec{k}$ must be carried out over the full 2DBZ, i.e. for positive and negative values of $\vec{k} = (k_x, k_y)$. This in turn implies that the number of k-points needed to achieve good numerical convergence of the SHG spectra is four times that of the usual case. In particular the results shown below are for $N_k = 256$ special k-points in the full 2DBZ, that along with $N = 16$ planes is enough to obtain convergence of SHG spectra. For $S(z)$ a step function centered at the middle of the slab is used.

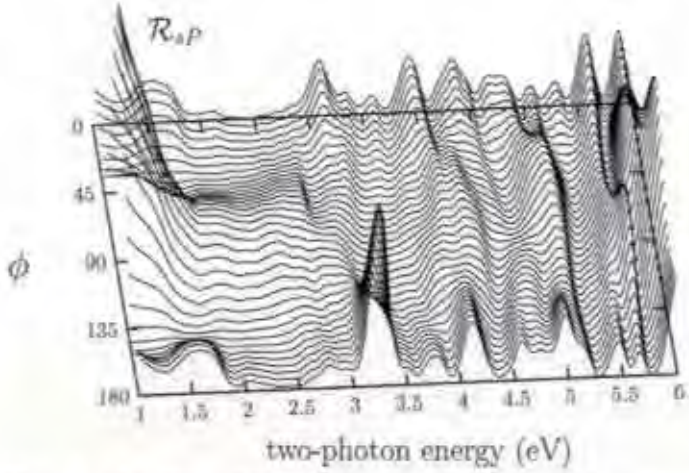

Figure 3.3: $\mathcal{R}_{sP}$ as a function of the two-photon energy and the azimuthal angle ϕ for a single-domain Si(100)c(4 × 2) clean surface. The angle of incidence is 45° and the maximum intensity is 1.2×10^{-18} W/cm^2 for $2\hbar\omega = 3.24$ eV

Using smoother functions yields the same SHG lineshape with only small changes in the absolute magnitude of $\mathcal{R}$.

3.3 Results

In Figs. 3.2-3.5 we show $\mathcal{R}$ for pP, sP, pS and sS input-output polarizations, respectively. The angle of incidence is $\theta = 45°$. We have shifted the theoretical curves upward in energy by 0.24 eV, in order to have a better correspondence between the calculated SHG E_1 resonance and the value of such bulk transition around 3.4 eV. Differences of this order, often occurring in SETB calculations [100], are due to the underlying approximations involved in the method. In carrying out the Kramers-Kronig transformation, a broadening of 50 meV was used; a larger (smaller) broadening will erase (sharpen) some of the small structures. The spectra have a series of resonances that have a rich and complex behavior as a function of ϕ and the photon energy. We can assign the following critical points of Si to some of the resonant peaks seen in the above figures. For instance $E_1 \sim 3.3$ eV, $E_2 \sim 4.2$ eV and $E_1' \sim 5.3$ eV in the spectra of $\mathcal{R}_{pP}$ and $\mathcal{R}_{sP}$, whereas for $\mathcal{R}_{pS}$ and $\mathcal{R}_{sS}$ these critical points are also seen but with smaller intensity and only for some

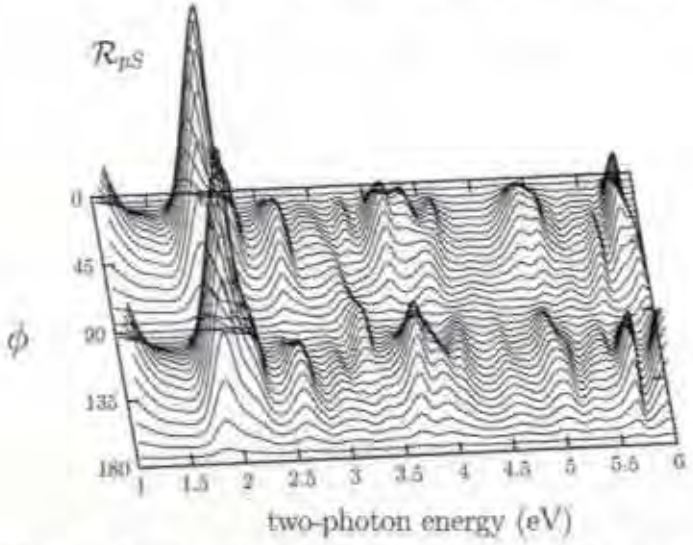

Figure 3.4: $\mathcal{R}_{pS}$ as a function of the two-photon energy and the azimuthal angle ϕ for a single-domain Si(100)c(4 × 2) clean surface. The angle of incidence is 45° and the maximum intensity is 1.8×10^{-1} W/cm^2 for $2\hbar\omega = 1.84$ eV

angles ϕ. All the resonances change their intensity and frequency to some extent as a function of ϕ. Some small resonances shift frequency and merge into larger structures, as the peak just below E_1 in $\mathcal{R}_{pP}$. Others shift their frequency until they disappear, as ϕ either increases or decreases. Where one of these resonances that disappears as ϕ increases (decreases), meets with one that disappears as ϕ decreases (increases), there is a double resonant structure, like E_1' in $\mathcal{R}_{pP}$. We mention that $\mathcal{R}(\phi) = \mathcal{R}(-\phi)$.

The dimer, as mentioned before, breaks the inversion symmetry along its direction, i.e. x, so from Eqs. (3.4) it follows that $\mathcal{R}_{pP}(0°) \neq \mathcal{R}_{pP}(180°)$, $\mathcal{R}_{sP}(0°) \neq \mathcal{R}_{sP}(180°)$, $\mathcal{R}_{pS}(45°) \neq \mathcal{R}_{pS}(135°)$ but $\mathcal{R}_{sS}(45°) = \mathcal{R}_{sS}(135°)$. Where the atoms in the underneath layers are include. This behavior is apparent for higher energies, which correspond to bulk states, throughout Figs. 3.2-3.5, and for pP, sP and pS, and we called it a *π-asymmetry*. Note also that above 2 eV and below 5.5 eV (in the two-photon energy), the intensity follows $\mathcal{R}_{pP} > \mathcal{R}_{sP} \sim \mathcal{R}_{pS} > \mathcal{R}_{sS}$, where $\mathcal{R}_{sS}$ is two orders of magnitude smaller than $\mathcal{R}_{pP}$ due to the fresnel factors.

To consider in more detail the behavior of the above spectra, we concentrate on the SHG E_1 resonance. This resonance has been measured in clean and adsorbate covered double-domain Si(100) and Si(111) surfaces [11, 12, 17–19, 23, 30], around

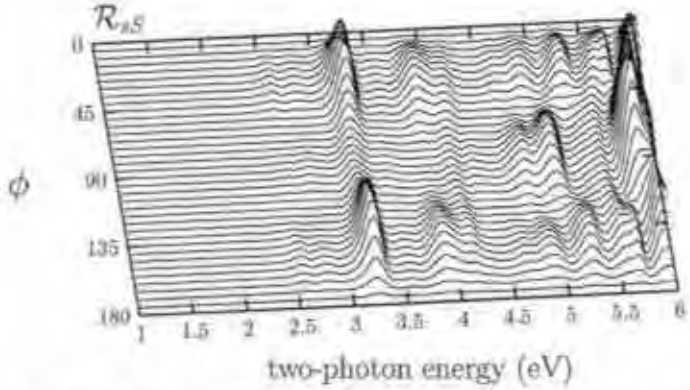

Figure 3.5: $\mathcal{R}_{sS}$ as a function of the two-photon energy and the azimuthal angle ϕ for a single-domain Si(100)c(4 × 2) clean surface. The angle of incidence is 45° and the maximum intensity is 0.10×10^{-18} W/cm^2 for $2\hbar\omega = 5.74$ eV.

~ 3.3 eV which is in good agreement with our theoretical values. In Fig. 3.6 some of the traces shown in Figs. 3.2-3.5 are shown for some fixed values of ϕ. For $\mathcal{R}_{pP}$ note that E_1 slightly redshifts as ϕ goes from 0° to 180°. Also, its intensity for 90° is smaller than at 0° or 180°. For $\mathcal{R}_{sP}$, E_1 strongly blueshifts as ϕ goes from 0° to 180°, and for 90° it disappears. For this combination of polarizations, $\mathcal{R}_{sP}(0°)$ is rather different from $\mathcal{R}_{sP}(180°)$, thus showing that the dimer-induced π-asymmetry could be large. For $\mathcal{R}_{pS}$ and $\mathcal{R}_{sS}$ the azimuthal angles of interest are 45°, 90° and 135°. From Fig.3.6, it follows that E_1 for $\mathcal{R}_{pS}$ is a broad structure for $\phi = 135°$ and that it is a well defined peak for $\phi = 45°$ and $\phi = 90°$, the latter showing a redshift with respect to the former. The difference between $\mathcal{R}_{pS}(45°)$ and $\mathcal{R}_{pS}(135°)$ is again due to the dimer-induced π-asymmetry. However, this asymmetry is no longer present in $\mathcal{R}_{sS}$, as can be seen in Fig.3.6, where $\mathcal{R}_{sS}(45°) = \mathcal{R}_{sS}(135°)$. Also E_1 for $\mathcal{R}_{sS}(90°)$ is redshifted with respect to the previous two identical signals.

Complementary to Figs. 3.2-3.6, we show in Fig. 3.7 polar plots of $\mathcal{R}$ fixing the two photon energy to E_1. Indeed from this plot the ϕ dependence is even more apparent. The spectra are symmetric with respect to the horizontal axis, i.e. $\mathcal{R}(\phi) = \mathcal{R}(-\phi)$; the π-asymmetry for pP, sP, and pS, and the totally symmetric sS spectra are clearly seen. Note that for sP the two corresponding E_1 peaks at $\phi = 0°$ and $\phi = 180°$ are shifted with respect to each other.

To understand some of the details of the figures, we have plotted in Fig. 3.8

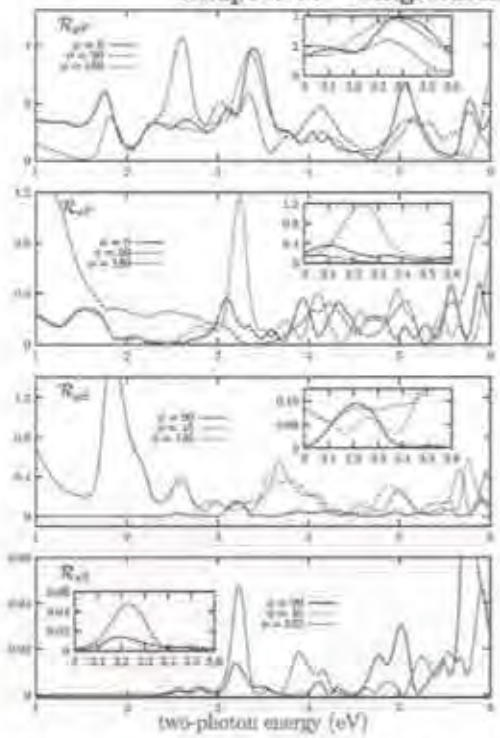

Figure 3.6: Selected traces of $\mathcal{R}$ for fixed values of ϕ as a function of the two-photon energy. For $\mathcal{R}_{pP}$ and $\mathcal{R}_{sP}$ the solid line is for $\phi = 0°$, the dashed line is for $\phi = 90°$, and the dotted line is for $\phi = 180°$. For $\mathcal{R}_{pS}$ and $\mathcal{R}_{sS}$ the solid line is for $\phi = 90°$, the dashed line is for $\phi = 45°$, and the dotted line is for $\phi = 135°$. Notice that $\mathcal{R}_{sS}(45°) = \mathcal{R}_{sS}(135°)$. $\mathcal{R}$ is given in 10^{-18} W/cm^2. Each inset shows the detail around E_1.

the absolute value of all nonzero components of $\overleftrightarrow{\chi}$ for C_{1v} as given in Table 3.1. The magnitude of $\overleftrightarrow{\chi}$ is consistent with the reported values of Höfer et al. [105]. We see that the anisotropic components of $\overleftrightarrow{\chi}$, i.e. those which are zero for the isotropic or C_{2v} symmetry, are smaller than the isotropic components, and that all of them except χ_{xxz} and χ_{zxz} show structure around E_1. From this figure and Eqs. (3.4) we can find the different contributions of $\overleftrightarrow{\chi}$ to $\mathcal{R}$, taking into account the different value of the prefactors that each susceptibility component has in Eqs. (3.4). For $\mathcal{R}_{pP}(0°, 180°)$ we see from r_{pP} that χ_{xxz}, χ_{xzx} and χ_{zxx} give the main contributions and that the interference among them gives rise to the shifted spectra at the two different angles. On the other hand, for $\mathcal{R}_{pP}(90°)$ only χ_{zyy}

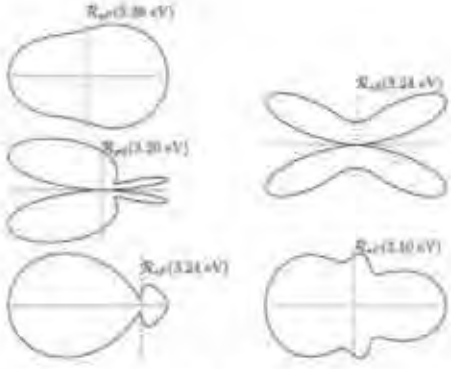

Figure 3.7: Polar plots of $\mathcal{R}$ for E_1. The energies chosen for E_1 are 3.38 eV for $\mathcal{R}_{pP}$ at 180°, 3.20 eV for $\mathcal{R}_{pS}$ at 90°, 3.10 eV at 0° and 3.24 eV at 180° for $\mathcal{R}_{sP}$, and 3.24 eV at 135° for $\mathcal{R}_{sS}$.

contributes. For $\mathcal{R}_{sP}(0°, 180°)$ we see from r_{sP} (Eq. (3.4b)) that only χ_{xyy} and χ_{xyy} contribute, as can be confirmed from Fig. 3.8. Then, from Eq. (3.4b), these terms add for $\phi = 0°$, but subtract for $\phi = 180°$, due to the $\cos^3(\phi)$ term of χ_{xyy}. This constructive/destructive interference gives rise to the shifted E_1 peak, even though χ_{xyy} is smaller than χ_{xyy}. On the other hand, r_{sP} is only proportional to χ_{zxz}, which as shown in Fig. 3.8 has no E_1 peak, in accordance to $\mathcal{R}_{sP}(90°)$ of Fig. 3.6. For $\mathcal{R}_{pS}(45°, 135°)$ we see from Fig. 3.8 that all components of r_{pS} (Eq. (3.4c)) contribute to some extent, and in this case the interference among all these components of $\overleftrightarrow{\chi}$ makes E_1 disappear from the spectra at $\phi = 135°$. For $\phi = 90°$ we see from Fig. 3.8 that χ_{xyy} dominates over χ_{xzz}, which are the only two components that contribute to r_{pS} (Eq. (3.4c)). Finally for $\mathcal{R}_{sS}(45°) = \mathcal{R}_{sS}(135°)$ we see that the three components given by r_{sS}, χ_{xzx}, χ_{xyy}, and χ_{yyx}, contribute to E_1 and that $\mathcal{R}_{yS}(90°)$ is only proportional to χ_{xzx} which is indeed responsible for the E_1 peak seen at this azimuthal angle.

To complement the spectra shown in Figs. 3.2-3.5, Figs. 3.9 and 3.10 show $\mathcal{R}$ for the case of a q-polarized incoming field, for P-polarized and S-polarized output, respectively. Note from Fig. 3.9, that $\mathcal{R}_{qP}$, gives a well defined E_1 peak with little dispersion as a function of ϕ, and another surface peak just below it that is present for all values of ϕ. On the other hand, the dispersion of E_1 as a function of ϕ for $\mathcal{R}_{qS}$ is large, and the same surface peak is only weakly present for some values of ϕ. The intensity is such that $\mathcal{R}_{qP} > \mathcal{R}_{qS}$ and both are of the same order of magnitude as $\mathcal{R}_{pP}$. The overall spectra basically follow the same rich and complex behavior for the other polarizations and could be explained using

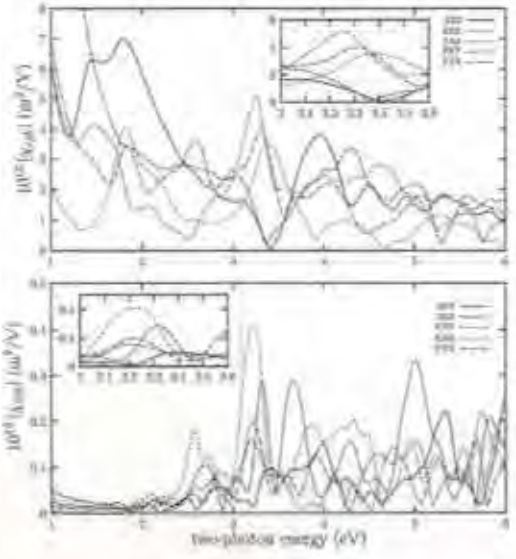

Figure 3.8: Absolute values of the components of $\overleftrightarrow{\chi}$ for the C_{1v} symmetry that corresponds to the single-domain dimerized surface. The top (bottom) panel is for the isotropic (anisotropic) components. Each inset shows detail around E_1.

the arguments given above.

As mentioned in Sec. 3.2, the atoms beneath the dimer atoms break the C_{2v} surface symmetry of the dimers alone. This implies a C_{1v} symmetry which gives $\mathcal{R}(0°) \neq \mathcal{R}(180°)$ for pP and sP and $\mathcal{R}(45°) \neq \mathcal{R}(135°)$ for pS polarization. That is, if a component of the incident fundamental or reflected SH beam has a component along the dimer, the π-asymmetry is present in $\mathcal{R}$, which means that this component explores the surface symmetry along the direction where it is broken. From Fig. 3.6 we notice an interesting point. For energies below E_1, which correspond to surface states, we see that the π-asymmetry is small, while for energies around and above E_1, it is readily present. The same behavior could be extracted from the q-polarized input field shown in Figs. 3.9 and 3.10. Therefore, for resonances whose electronic transitions take place among energy states within the dimer, the surface symmetry should be that of the dimers alone, i.e. C_{2v}, and thus no π-asymmetry should be present. On the other hand, if the resonance involves energy states related not only with the dimer atoms, but with the atoms beneath, the symmetry should be C_{1v}, thus showing the aforementioned

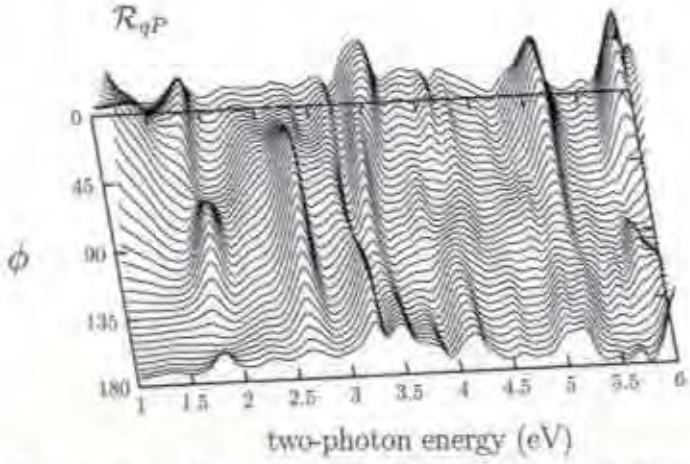

Figure 3.9: $\mathcal{R}_{qP}$ for a q-polarized input field, as a function of the two-photon energy and the azimuthal angle ϕ for a single-domain Si(100)c(4 × 2) clean surface. The angle of incidence is 45° and the maximum intensity is 1.4×10^{-18} W/cm^2 for $2\hbar\omega = 5.74$ eV.

anisotropy. Recently, in Ref. [31] a detailed analysis of SHG from double-domain Si(100)c(4 × 2) surface has shown that the surface resonances are indeed related to electronic transitions confined to the dimer, and that the bulk resonances come from electronic transitions that involve dimer and subsurface atoms. We have checked that this anisotropy is zero at all frequencies for an ideally terminated Si(100) surface as it must be for a C_{2v} surface. Finally we note that the SHG is generated by surface and subsurface atoms, where the inversion symmetry of the bulk is broken.

3.4 Conclusions

We have calculated the SHG spectra of a single-domain Si(100) surface with a c(4 × 2) reconstruction. The concomitant formation of the dimers as the surface relaxes to its equilibrium configuration gives a surface with C_{1v} symmetry. The anisotropies shown by the SHG radiated efficiency $\mathcal{R}$ are related to the spatial localization of the electronic transitions of the particular SHG resonance. For surface resonances the SHG spectrum shows a C_{2v} symmetry, which

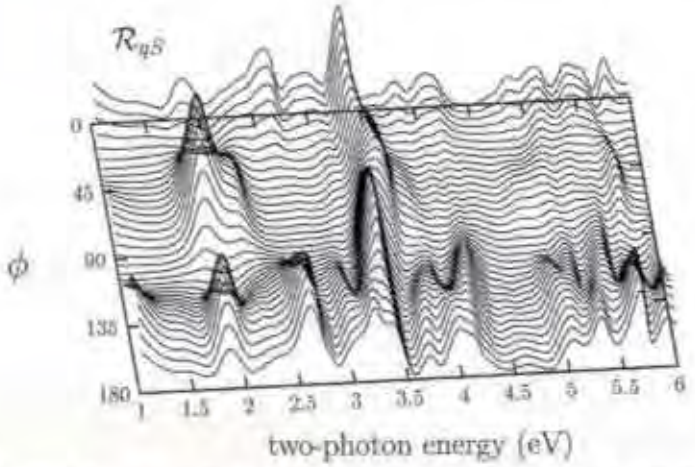

Figure 3.10: $\mathcal{R}_{qS}$ for a q-polarized input field, as a function of the two-photon energy and the azimuthal angle ϕ for a single-domain Si(100)c(4 × 2) clean surface. The angle of incidence is 45° and the maximum intensity is 0.8×10^{-18} W/cm^2. for $2\hbar\omega = 3.24$ eV.

implies $\mathcal{R}_{pP}(0°) = \mathcal{R}_{pP}(180°)$, $\mathcal{R}_{sP}(0°) = \mathcal{R}_{sP}(180°)$, $\mathcal{R}_{pS}(45°) = \mathcal{R}_{pS}(135°)$, and $\mathcal{R}_{sS}(45°) = \mathcal{R}_{sS}(135°)$. In contrast, for the bulk SHG resonances that sample the energy states of atoms below the dimer atoms, the symmetry of the spectrum is reduced to a C_{1v} class, for which $\mathcal{R}_{pP}(0°) \neq \mathcal{R}_{pP}(180°)$, $\mathcal{R}_{sP}(0°) \neq \mathcal{R}_{sP}(180°)$, and $\mathcal{R}_{pS}(45°) \neq \mathcal{R}_{pS}(135°)$. We called this a π-asymmetry. Concentrating on E_1 we explain its behavior for the different polarization combinations of incoming (fundamental) and outgoing (SH) beams in terms of the radiation formulas and the different components of the non-linear susceptibility tensor $\overleftrightarrow{\chi}$. The spectra shown by this calculation show a rich and complex structure that should be experimentally explored.

Chapter 4

Polarizable Bond Model for Si(111):(1×1)

4.1 Introduction

An important example of surface SHG is given by the resonance measured around 3.3 eV (in the two-photon energy) in Si [12]. This resonance coincides with the E_1 bulk critical point of Si, that is SHG (dipolar) allowed due to the presence of the surface. Modifications on the surface change this resonance, and thus it can be ascribed as a surface enhanced SHG resonance. Therefore, this E_1 surface SHG peak has been used to study different aspects of the Si(100) and Si(111) surfaces with several reconstructions, adatom coverage, etc [12,13,15–18,20,21,38,107,108]. Höfer [17] and Dadap et al. [19] demonstrated the ability of SHG to describe the dynamics of H adsorption on Si surfaces. Recently in Ref. [68] femtosecond laser pulses have been used to measure SHG of several chemical modifications of Si(111) surfaces around E_1, and in Ref. [67] the spectrum for the H-covered surface has been measured including the E_2 critical point as well.

In this Chapter we present a study based on the PBM of the SHG spectra of a Si(111):H (1×1) surface close to the E_1 resonance. In particular, we study the changes that the position of the Si back-bond produces in the SHG spectra.

4.2 Preliminary Considerations

As we mentioned in Sec. 2.1 the PBM considers the semiconductor crystal as an array of point-like polarizable dipoles where each dipole is located at the middle of every Si-Si bond since the maximum distribution of valence charge is precisely located here [75]. However, for the Si1-H and Si1-Si2 bond the actual position of the dipole may be off-centered due to the charge transfer that takes place as the surface reconstructs [109] (Fig. 4.1).

Within PBM, the polarizability $\overleftrightarrow{\alpha}$ is written in terms of the principal polarizabilities $\alpha_{\parallel}$ and $\alpha_{\perp}$, where $\parallel$ ($\perp$) is parallel (perpendicular) to the bond. Close to the visible spectral region, we expect that the main contributions to $\alpha_{\parallel}$ originate in bonding-antibonding transitions, while $\alpha_{\perp}$ is due mainly to transitions involving atomic states with different symmetry. We assume that the latter has larger resonant frequencies than the former, and we approximate $\alpha_{\perp}$ by a Lorentzian centered at some relatively high frequency $\omega_{\perp}$ with a weight characterized by a frequency ω_p, and ω_c as a damping parameter. Then,

$$4\pi n_B \alpha_{\perp}(\omega) = \frac{\omega_p^2}{\omega_{\perp}^2 - (\omega + i\omega_c)^2}, \tag{4.1}$$

with n_B the bulk density of bonds. To obtain $\alpha_{\parallel}(\omega)$, we use the following equation,

$$\vec{P}(B,\omega) = \frac{\epsilon(\omega) - 1}{4\pi}\vec{E}(B,\omega), \tag{4.2}$$

where $\vec{P}(B,\omega)$ is the total bulk dipole moment, $\vec{E}(B,\omega)$ is the electric field in the bulk and $\epsilon(\omega)$ is the experimentally measured bulk dielectric function. Since $\vec{P}(B,\omega)$ is a function of $\alpha_{\parallel}$ and $\alpha_{\perp}$, Eq. (4.2) yields an analytical relation between $\overleftrightarrow{\alpha}$ and $\epsilon(\omega)$, which is a generalized Clausius-Mossotti relation [24, 25]. Therefore, once $\omega_{\perp}$, ω_p and ω_c are chosen in Eq. (4.1), we can solve Eq. (4.2) for $\alpha_{\parallel}$ for any given $\epsilon(\omega)$. Then we follow the method of Ref. [24, 25] to solve the local field equations for the linear and nonlinear dipole moments, through which the surface non-linear susceptibility $\overleftrightarrow{\chi}$ is calculated. Alternative approaches, where the bare and dressed contributions to $\overleftrightarrow{\alpha}$ are considered, can be found in [63, 110, 111].

To obtain the reflected SHG efficiency $\mathcal{R}$, we use that the symmetry group C_{3v} of an ideal (111) surface has the following non-zero components: $\chi_{zzz} \equiv \chi_{\perp\perp\perp}$, $\chi_{zxx} = \chi_{zyy} \equiv \chi_{\perp\parallel\parallel}$, $\chi_{xxz} = \chi_{yyz} \equiv \chi_{\parallel\parallel\perp}$, and $\chi_{xxx} = -\chi_{xyy} = -\chi_{yyx} \equiv$

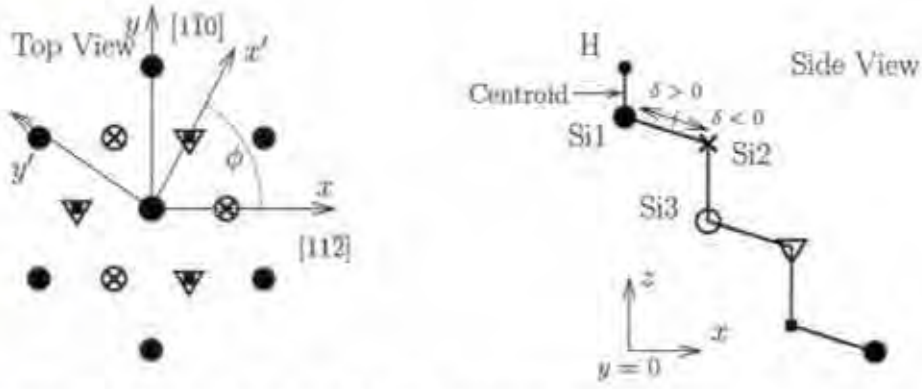

Figure 4.1: Top and side view of Si(111):H (1 × 1). The Si1-H bond centroid and the displacement δ of the Si1-Si2 bond from its bulk centered position are shown.

$\chi_{\parallel\parallel\parallel}$, where we have chosen the x and y axes along the $[11\bar{2}]$ and $[1\bar{1}0]$ directions, respectively. Also, the intrinsic permutation symmetry $\chi_{ijk} = \chi_{ikj}$ is satisfied. The $\chi_{\parallel\parallel\parallel}$ component induces a SH response which is anisotropic with respect to the azimuthal angle ϕ that the plane of incidence makes with the x axis (Fig. 4.1). The radiated SHG efficiency $\mathcal{R}$ is given in the next Chapter.

4.3 Results

In the calculations, the values used for the frequency parameters of Eq. (4.1) are $\hbar\omega_\perp = 7.05$ eV and $\hbar\omega_p = 1.68$ eV. These were obtained by finding the best agreement with the experimental results of SHG. The value of $\hbar\omega_\perp$ is of the order of the transition energy between the atomic states of Si $3p^2{}^3P$ with $J = 0$ and $3d^3D^0$ with $J = 1$ [112], in qualitative agreement with the discussion before Eq. (4.1). These parameters are also consistent with the ones used in Ref. [24,25]. We finally mention that the results do not depend strongly on ω_c as long as $\omega_c \ll \omega_\perp$ (we take $\hbar\omega_c = .2$ eV) and that a good numerical convergence was reached with ~ 20 crystalline planes.

In principle one should choose an appropriate $\overleftrightarrow{\alpha}(\omega)$ for the Si1-H and Si1-Si2 bonds. However, to keep the number of adjustable parameters to a minimum, and to look into the phenomenology that the present model allows in very simple physical terms, we take only two variables in consideration. One is the position of the bond centroid where we locate the polarizable harmonic oscillator, and

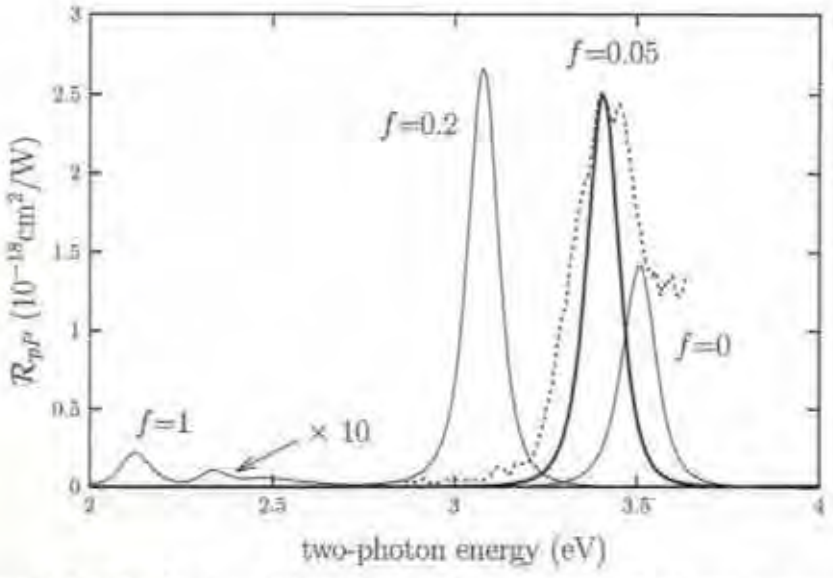

Figure 4.2: $\mathcal{R}_{pP}$ for $\phi = 30°$ vs the two-photon energy. The linear susceptibility of the Si1-H bond is adjusted through f in order to obtain the correct E_1 position at $\sim$ 3.4 eV (thick line). The experimental result from Ref. [68] (dotted line) is rescaled on the vertical axis, and its maximum intensity is $\sim 7 \times 10^{-21}$ cm^{2}W^{-1}.

the other is the linear polarizability of the surface bonds that is simply taken as $f \overleftrightarrow{\alpha}(\omega)$. The position of the centroid and f are enough to get agreement with experiment, as well as insight into the SHG process of this surface.

According to Ref. [109] the charge transfer between H and Si1, moves the charge centroid from its nominal position at the center of the bond (0.74Å) towards Si1 by 4.1% (Fig. 4.1). Then, the position of the Si-H bond is taken at 0.71 Å from the Si1 position. In Fig. 4.2, we show $\mathcal{R}_{pP}$ taking $f \overleftrightarrow{\alpha}$ for the Si-H bond, for different values of f, along with the experimental result from Ref. [68]. Note that the calculated intensity is larger than the one reported in Ref. [68], however the line shape and energy position of the resonance are very well described by the PBM. For $f = 0$, which represents a clean surface, we see a well defined E_1 peak at 3.5 eV, similar to that of Ref. [24,25]. As f is increased, E_1 redshifts until for $f = 1$, the spectrum shows two very weak peaks at 2.2 and 2.3 eV. This case, corresponds to the replacement of the Si-H bond by a bulk Si-Si bond at the Si-H centroid. If the centroid is moved back to the Si-Si centroid at 1.17 Å above Si1, we find only one peak strongly blueshifted that corresponds to E_1. From Ref. [68],

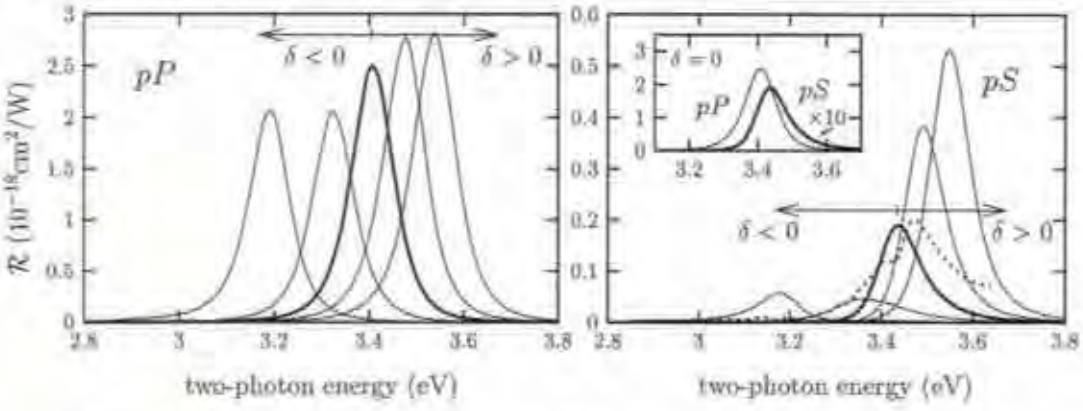

Figure 4.3: $\mathcal{R}$ for $\phi = 30°$ vs the two-photon energy. Left and right panels are for pP and pS polarizations, respectively. The variation of E_1 with δ of Fig. 4.1 is shown. δ is changed by $\pm 5\%$ and $\pm 10\%$, from the reference spectra (thick line) at ~ 3.4 eV. The inset shows the reference spectra ($\delta = 0$), where pS is blueshifted with respect to pP. For pS the experimental result from Ref. [68] (dotted line) is rescaled on the vertical axis and its maximum intensity is $\sim 10 \times 10^{-21}$ cm^{2}W^{-1}.

the experimental spectrum shows E_1 at ~ 3.4 eV, and we find that $f = .05$ gives the theoretical peak at this position. This f, that represent 5% of the value used for the Si-Si linear microscopic polarizability $\overleftrightarrow{\alpha}$, indicates that a small contribution from the Si-H bond is needed to give the experimental value, and clearly shows the surface sensitivity of SHG. Thus, assuming that the linear polarizability of the Si1-H bond is proportional to the bulk Si-Si bond gives good results. Also, we have checked that moving the centroid around the chosen position does not change the SHG spectrum.

The charge transfer in the Si1-H bond, induces noticeable changes in the Si1-Si2 backbond (Fig. 4.1), whereas it leaves the more internal Si-Si interactions as those of the bulk [109]. This leaves the Si1 atom isolated from the outside by its interaction with the H atom, while the Si2 atom is more prone to interact with an approaching chemical agent. For instance, the experimental observation that passive substitution or oxidation on this surface, are mediated by Si2 and not by Si1 [113,114], allow us to identify Si2 as true *surface* atoms [109]. Within the PBM we can study the behavior of SHG under modifications of any given Si-Si bond, in particular the back bonds, and thus test the former ideas through non-linear optics. In the following results we fix the Si1-H bond as described in the previous paragraph, and take this spectrum, that agrees with the experimental data, as a

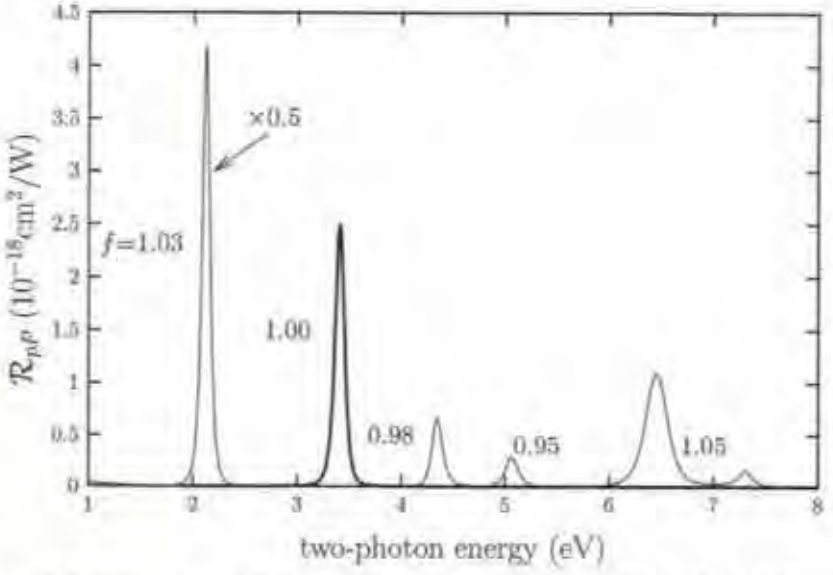

Figure 4.4: $\mathcal{R}_{pP}$ for $\phi = 30°$ vs the two-photon energy. The polarizability of the Si1-Si2 bond is taken as $f\ \overleftrightarrow{\alpha}$, and the variation of E_1 with f is shown

reference.

We begin by changing the centroid of charge of the back-bond, which implies an off-centered position for its polarizability $\overleftrightarrow{\alpha}$. The variable δ is defined as the distance that the backbond centroid is moved around the centered position along the bond's axis, and is expressed as a percent of bond length (Fig. 4.1). In Fig. 4.3 we show the calculated SHG spectra, along with the experimental results from Ref. [68], for different values of δ, where a positive (negative) value indicates that the centroid is closer to Si1 (Si2). Notice that the intensity of the calculated pS spectrum is smaller than for the pP case, contrary to the experimental result. For positive (negative) δ E_1 is blueshifted (redshifted) and its intensity increases (decreases) with respect to the reference spectrum. Note that the intensity changes more for the pS than for the pP configuration. This is related to the fact that for $\phi = 30°$, $\mathcal{R}_{pP}$ is given by the contribution of $\chi_{\perp\perp\perp}$, $\chi_{\perp\parallel\parallel}$, and $\chi_{\parallel\parallel\perp}$, and $\mathcal{R}_{pS}$ is given by $\chi_{\parallel\parallel\parallel}$ alone (see Eqs. (5.3a) and (5.3b)). Indeed, for pP the contribution of $\chi_{\perp\parallel\parallel}$ dominates the spectrum. Thus we see how different components of $\overleftrightarrow{\chi}$ respond differently to surface changes. Likewise, we can fix δ, and take $f\ \overleftrightarrow{\alpha}$ as the polarizability of the backbonds. Fig. 4.4 shows $\mathcal{R}_{pP}$ for $\delta = 0$ and several

values of f. Again the SHG signal shows large changes as a function of f, but in contrary to the previous case, the changes do not follow a trend for E_1's blueshifts or redshifts. In this case the change of the linear susceptibility of the backbond does not agree with the experimental results. Therefore the lineal susceptibility of the backbond is not affected by the Si1-H bond and should maintain the value of the Si-Si bond. Then the effect of the Si1-H bond only is on the position of the backbond.

A final point that is worth considering is the experimental result of Ref. [68], where for Si(111):H (1×1) the SHG E_1 peak in the pS configuration is blueshifted with respect to the pP case by 5 meV. Although the PBM gives an smaller shift of 2 meV (see inset of Fig. 4.3), the sensitivity of SHG to the different components of $\overleftrightarrow{\chi}$ is experimentally confirmed. Also, when this surface is modified to be either oxidized or covered with $C_{10}H_{21}$(-decyl) monolayers, E_1 is redshifted with respect to the H-covered case for both pP and pS polarizations. It is plausible to argue, that as the Si(111) surface is covered with other substance, the Si dangling bonds will be saturated first. For H this will be the end of the process, but for the oxide or decyl covered surfaces, extra interaction with the backbonds will produce the experimentally blueshifted E_1 peak, which according to the PBM is produced by the charge centroid being displaced towards Si2. This mechanism is ultimately produced by the local-field effect, that influences the components of $\overleftrightarrow{\chi}$ differently.

As shown in Figs. 4.2, 4.3 and 4.4, the PBM overestimates the SHG intensity by two orders of magnitude. This result may be explained by the simple approach taken in here, by which only the bare contribution to $\overleftrightarrow{\alpha}$ is used in the calculation, and thus the polarization of every bond is overestimated. Inclusion of the bare and dressed parts of $\overleftrightarrow{\alpha}$ as in Refs. [63, 110, 111] may be required to find better quantitative agreement with experiment, but this is beyond the scope of the present work. Nevertheless, the qualitative features of the experiments are well reproduced by the PBM, with a direct physical understanding.

4.4 Conclusions

We conclude that SHG is very sensitive to back-bond changes for a Si(111):H (1×1) surface, and that by use of the PBM we can obtain qualitative information which gives physical insight into the non-linear optical phenomena taking place. Although the PBM overestimates the SHG intensities and gives the pS

yield smaller than the pP yield, the line-shape and energy position of the E_1 SHG peak follows the correct experimental trend. The PBM is driven by the local-field effect, that for this surface shows clearly how the inversion symmetry is broken in the surface region, and how the spatial position of the bonds determines SHG. Similar results are found by the microscopic models of the following Chapters, that also show a large SHG sensitivity to the backbonds [67]. Therefore, the less computational demanding and easier to interpret PBM calculations are very useful to study surface SHG.

Chapter 5

Microscopic Calculations for Si(111):H (1×1)

5.1 Introduction

In this Chapter we study Si(111):H with a 1×1 reconstruction, which is the most simple of all semiconductor surfaces. Indeed, the relaxed atomic geometry of minimum energy corresponds to an ideally bulk terminated (111) surface, with an H atom saturating each Si dangling bond at the nominal Si-H distance of 1.48 Å. We use a microscopic formulation to calculate the second harmonic generation. We apply a semi-empirical tight binding method (SETB) (as in Chapter 3) and an *ab-initio* method to evaluate the microscopic nonlinear surface susceptibility tensor $\overleftrightarrow{\chi}$. We do an extensive analysis on the different parameters that enter the calculation in order to assess the convergence of the results. Thus, we study this convergence as a function of the number of crystalline planes, number of k-points, energy cut-off, etc. The comparison of the theoretical spectra with the experimental results is good and several interesting conclusions are drawn from here. In Sec. 5.2 we describe the theoretical scheme used to calculate SHG through the nonlinear susceptibility tensor $\overleftrightarrow{\chi}$. In Sec. 5.3 we present and analyze the results for both methods and their comparison with the experimental spectra. Finally, in Sec. 5.4 conclusions are made.

5.2 Preliminary Considerations

To calculate the reflected SHG efficiency $\mathcal{R}$, we use the second-order susceptibility tensor $\overleftrightarrow{\chi}$. Out of the 27 possible components of χ_{ijk}, the symmetry properties of the surfaces make most of them to vanish. As in the previous Chapter, an ideal (111) surface belongs to a symmetry group C_{3v}, we get the following non-zero components of $\overleftrightarrow{\chi}$,

$$\chi_{zzz} \equiv \chi_{\perp\perp\perp}, \tag{5.1a}$$

$$\chi_{zxx} = \chi_{zyy} \equiv \chi_{\perp\parallel\parallel}, \tag{5.1b}$$

$$\chi_{xxz} = \chi_{yyz} \equiv \chi_{\parallel\parallel\perp}, \tag{5.1c}$$

and

$$\chi_{xxx} = -\chi_{xyy} = -\chi_{yyx} \equiv \chi_{\parallel\parallel\parallel}, \tag{5.1d}$$

where, we have chosen the x and y axes along the $[11\bar{2}]$ and $[1\bar{1}0]$ directions, respectively (see Fig. 4.1). Also, the intrinsic permutation symmetry $\chi_{ijk} = \chi_{ikj}$ is satisfied. The $\chi_{\parallel\parallel\parallel}$ component induces a SH response which is anisotropic with respect to the azimuthal angle ϕ that the plane of incidence makes with the x axis. Then as in Chapter 3, we calculate $\overleftrightarrow{\chi}$ on the fixed x and y axes and then we rotate it so the new x' direction is along the incident plane of the fundamental beam. With these rotated components, it is straightforward to obtain that for a fundamental i-polarized beam, the f-polarized SH output for a surface with a C_{3v} symmetry is given by

$$\mathcal{R}_{if} = \frac{32\pi^3\omega^2}{(n_0 c)^2 c^3 \cos^2\theta} |T_f(2\omega) T_i^2(\omega) r_{if}|^2, \tag{5.2}$$

where $i = s$ or p indicates the polarization of the incoming photon of frequency ω, and $f = S$ or P the polarization of the outgoing photon of frequency 2ω. Here,

$$\begin{aligned} r_{pP} &= \sin\theta \epsilon_b(2\omega) \left(\sin^2\theta \epsilon_b^2(\omega) \chi_{\perp\perp\perp} + k_{zb}^2(\omega) \epsilon_\ell^2(\omega) \chi_{\perp\parallel\parallel} \right) \\ &\quad + \epsilon_\ell(\omega) \epsilon_\ell(2\omega) k_{zb}(\omega) k_{zb}(2\omega) \left(-2\sin\theta \epsilon_b(\omega) \chi_{\parallel\parallel\perp} \right. \\ &\quad \left. + k_{zb}(\omega) \epsilon_\ell(\omega) \chi_{\parallel\parallel\parallel} \cos(3\phi) \right), \end{aligned} \tag{5.3a}$$

$$r_{sP} = \sin\theta \epsilon_b(2\omega) \chi_{\perp\parallel\parallel} - k_{zb}(2\omega) \epsilon_\ell(2\omega) \chi_{\parallel\parallel\parallel} \cos(3\phi), \tag{5.3b}$$

$$r_{pS} = -k_{zb}^2(\omega)\epsilon_t^2(\omega)\chi_{|||||}\sin(3\phi), \tag{5.3c}$$

and

$$r_{sS} = \chi_{|||||}\sin(3\phi). \tag{5.3d}$$

We have used the three-layer-model of Sec. 2.3, where the different quantities could be found. These expressions are strictly valid within the dipole approximation. It is interesting to notice that the pS or sS SH efficiency measures $\chi_{|||||}$ directly.

As we mention in Chapter 2, the semi-infinite solid is modeled by a slab of N atomic planes which is intrinsically centrosymmetric. To break this centrosymmetry, we introduced the $S(z)$ function of Eq. (2.37). This means that we must guarantee that the slab that represents Si(111):H is symmetric with respect to its center. This in turn means that the front and back surfaces must have the same surface symmetry. Then, we must consider slabs with multiples of six atomic planes of Si, where the single dangling bond of the front and back surface is saturated by one H. Such unit cell with six atomic planes of Si, assures that the same geometry is obtained for both (111) faces of the slab. Thus, we can have slabs with 6, 12, 18, etc. planes of Si, always adding one saturating H atoms for each of the two surfaces.

5.3 Results

We use the density functional theory within the local density approximation (DFT-LDA) to find the equilibrium atomic positions for the Si(111):H 1×1 surface. In the *ab-initio* approach, the electronic wave functions and eigenvalues are obtained from this self-consistent calculation using a plane-wave basis set with an energy cut-off of 15 Ry, with which the momentum matrix elements are calculated, and then Eq. (2.35) is evaluated. The structure that we obtain is in agreement with similar structure calculations of Ref. [115] and Ref. [109], to wit, the H-Si distance is 1.48 Å, and the relaxation of the subsurface atoms is less than 3% from the ideal positions. For the SETB approach, we use the previous atomic structure, with which we calculate the one-electron energies, wave functions and the momentum matrix elements following Ref. [27], and then evaluate Eq. (2.35) for the nonlinear susceptibility. To coincide with the experiment [116], we take $\phi = 30°$, with which $\chi_{|||||}$ drops from r_{pP} and maximizes its contribution in r_{pS}, and $\theta = 65°$.

We show in Fig. 5.1 and Fig. 5.2 the radiation efficiency as a function of

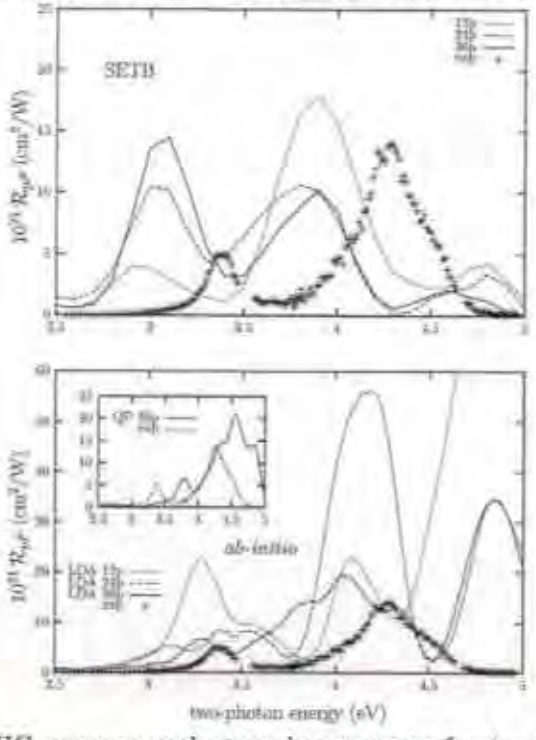

Figure 5.1: $\mathcal{R}_{Pp}$ SHG response vs the two photon energy for $\phi = 30°$ and $\theta = 65°$. The experimental data are shown with plus signs and the theoretical results are rescaled with a factor of 1/10 in the vertical axis. The top panel shows the SETB results for 12 (dots), 24 (short-dashes), and 36 (solid) planes. The bottom panel shows the *ab-initio* results for 12 (dots), 24 (short-dashes), and 36 (solid) planes. The inset shows the spectrum for 36 planes (solid line) along with the experiment (dotted line). Note E_1 ($\sim$ 3.3 eV) and E_2 ($\sim$ 4.3 eV) experimental SH peaks.

two-photon energy for different number of atomic planes, for $\mathcal{R}_{pP}$ and $\mathcal{R}_{pS}$, respectively. In each figure we show the SETB, *ab-initio*, and experimental spectra for comparison. The theoretical curves overestimate the experimental intensity by a factor of ~ 10, that in view of the approximations is a rather good result. Also, SETB and *ab-initio* give very similar intensities. In carrying out the Kramers-Kronig transform, a finite broadening of 75 meV was used; a larger (smaller) broadening will erase (sharpen) some of the structures. With this broadening the comparison with experiment is good. The overall spectra show well defined E_1 ($\sim$ 3.3 eV) and E_2 ($\sim$ 4.3 eV) SH peaks for both pP and pS, in agreement with experiment. Below E_1 the spectra are zero as they should from the fact that there

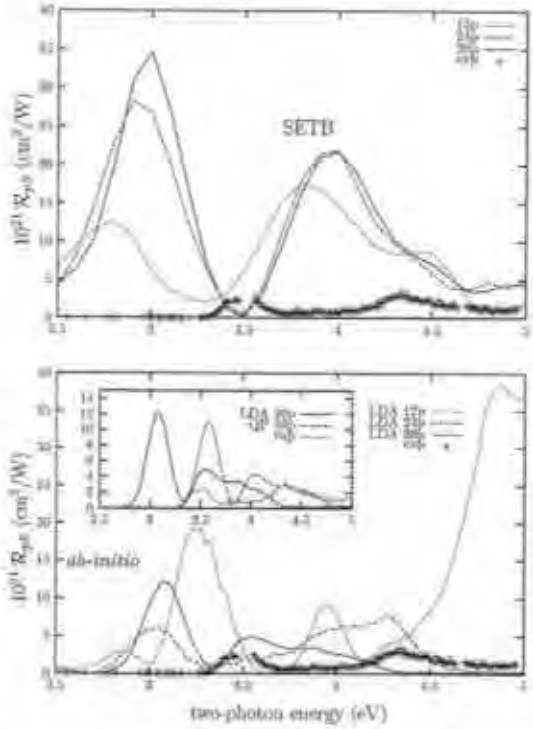

Figure 5.2: Same as Fig. 5.1 but for $\mathcal{R}_{pS}$. The experimental data are shown with plus signs and the theoretical results are rescaled with a factor of 1/10 in the vertical axis. The inset shows the spectra for 36 planes, where the solid line is the LDA result, the short-dashed line is the QP results for $\Delta = 0.5$ eV, and the dotted line is the experimental result. Note E_1 (~ 3.3 eV) and E_2 (~ 4.3 eV) experimental SH peaks.

are no surface related states, and above E_2 one can recognize E_1' around 5 eV. It is very interesting that the intensity of $\mathcal{R}$ is larger than for a Si(100) surface [27], a fact that could be related to the closer packing of the atoms in Si(111). Now, we proceed by describing the spectra for the different cases in more detail.

First, we have shifted upward in energy the theoretical SETB curves by 0.3 eV, in order to have a better correspondence in energy between calculated and measured structures. Differences of this order, often occurring in SETB calculations [100], are due to the underlying approximations involved in the method; in this case they could be related to surface effects on the electron self-energies. For SETB we notice that 36 or more planes are required to find converging spectra.

For pP or pS $\mathcal{R}$ shows the experimentally correct intensity ratio between E_1 and E_2 for 12 planes, but for 24 or more planes $\mathcal{R}(E_1) > \mathcal{R}(E_2)$, thus reversing the correct ratio. The position of E_1 and E_2 are basically independent of the number of planes and agree well with the experiment. The intensity for pP is larger than the experimental one by a factor of ~ 10, and for pS the theoretical curves are almost two orders of magnitude higher.

On the other hand, the *ab-initio* calculation shows a different behavior. As we can see from Fig. 5.1, in the pP spectra the convergence of E_1, E_2 and E_1' as a function of the number of unit cells, is slower than for SETB. However, the calculated spectra also show a redshift with respect to the experiment of ~ 0.3 eV for E_2. For pS (see Fig. 5.2) the convergence of the peaks is even slower. For instance notice how the E_1' peak is strongly quenched as we move from 12 to 24 or 36 planes. Also, for 36 planes, the energy separation between E_1 and E_2 is shorter than the experimental one, and the spectrum is redshifted from the experiment by almost 0.5 eV. The intensity of E_2 is ~ 10 larger than the measured one, and that of E_1 is a factor of ~ 20 larger. In any case, the intensity ratio between pP and pS is in better agreement with experiment if calculated by *ab-initio* than with SETB. Also, the experimental inequality $\mathcal{R}(E_1) < \mathcal{R}(E_2)$, is correctly preserved for the pP *ab-initio* spectra.

As we see from the above results, although SETB and *ab-initio* give an overall spectra that compares fairly well with the experiment, there are some discrepancies which may reflect in a sense the limitations of the methods. To improve beyond DFT-LDA in SHG, and correct the redshifted spectra, we follow Ref. [32] and include quasi particle (QP) corrections within the scissors approximation with a shifting parameter Δ, as explained in Chapter 2. Recently, the QP corrections have been applied to surface SHG [32], where the QP effects on a clean and H covered Si(100)c(4×2) surface make the SHG efficiency $\mathcal{R}$ agree with experiment. But as this system has surface related resonances, the QP corrections not only shift the resonances to higher energies, but also redistribute substantially their weights, as a consequence of the different shifts of 1ω and 2ω resonances in Eq. (2.35). [32] However, for Si(111):H (1×1), the absence of surface states produces and almost rigid shift of the spectrum. Indeed, in Fig. 5.2 we show the spectrum for pS with QP corrections for $\Delta = 0.5$ eV, a value that produces a bulk dielectric function in good agreement with the experimental one. We see that the spectrum is almost rigidly blueshifted and that the position of E_1 coincides with the measured one, but as we explained above, E_2 is still redshifted with respect to the experiment.

It is interesting to notice that for pP an smaller $\Delta \sim 0.3$ eV would be required for a very good agreement with the experiment. Thus, even though QP corrections blueshift the components of $\overleftrightarrow{\chi}$ by the same amount, the interference of $\chi_{\perp\perp\perp}$, $\chi_{\perp\parallel\parallel}$ and $\chi_{\parallel\parallel\perp}$ in r_{pP} (Eq. (5.3a) with $\phi = 30°$) gives $\mathcal{R}_{pP}$ less blueshifted than $\mathcal{R}_{pS}$ which is only related to $\chi_{\parallel\parallel\parallel}$.

In the same spirit, the inversion of $\mathcal{R}(E_2)$ with respect to $\mathcal{R}(E_1)$, in the SETB approach can be understood as follows. Recently, in Ref. 31 a method to analyze the different contributions of the nonlinear susceptibility tensor $\overleftrightarrow{\chi}$, which are classified according to 1ω and 2ω transitions and to the surface or bulk character of the states among which the transitions take place, was successfully used to analyze the effects of these microscopic susceptibilities on the SHG spectrum of a clean Si(100)c(4 × 2) surface. We apply, such formalism to our surface and present here only the main results. First, it turns out that the $\mathcal{R}_{pP}$ SHG spectra are produced by the interference of $\chi_{\parallel\parallel\perp}$ and $\chi_{\perp\parallel\parallel}$ alone, see Fig. 5.3 with the contribution of $\chi_{\perp\perp\perp}$ being negligible. In contrast, we mention that for a Si(100) surface only $\chi_{\parallel\parallel\perp}$ dominates. [27,31] As we increase the number of unit cells $\chi_{\perp\parallel\parallel}$ remains almost unchanged, but $\chi_{\parallel\parallel\perp}$ changes in such a way that this component of $\overleftrightarrow{\chi}$ gives the aforementioned inversion of the intensity. Analyzing the several contributions to $\chi_{\parallel\parallel\perp}$ reveals that only one component changes as we increase the number of unit cells. This component involves 2ω transitions across the energy gap from the bulk states in the valence band to the bulk states in the conduction band, then a transition into a virtual bulk state in the conduction band, see Fig. 5.3. These surface states are classified according to the localization of its wavefunction in the surface region, and even though the surface is ideal and the Si dangling bonds are H saturated, the slab itself introduces this surface states. These states are not in the energy gap, rather they are intermixed with the bulk states, and are thus known as resonant states [31]. Therefore, we can conclude that as we increase the number of unit cells, the surface related states tend to disappear making their contribution less important. Thus, in slab calculations one has to be very careful about this fact. A similar analysis can be carried for the pS spectra with the same conclusions. Although SETB gives well converged spectra, its intrinsic limitations give for this surface in particular the inversion of $\mathcal{R}(E_2)$ with respect to $\mathcal{R}(E_1)$.

Several other issues that affect calculated spectra have been checked. For instance the number of k-points in the summation over the 2DBZ in Eq. (2.35) is essential to obtain converged data. We have used 126 special k-points and have

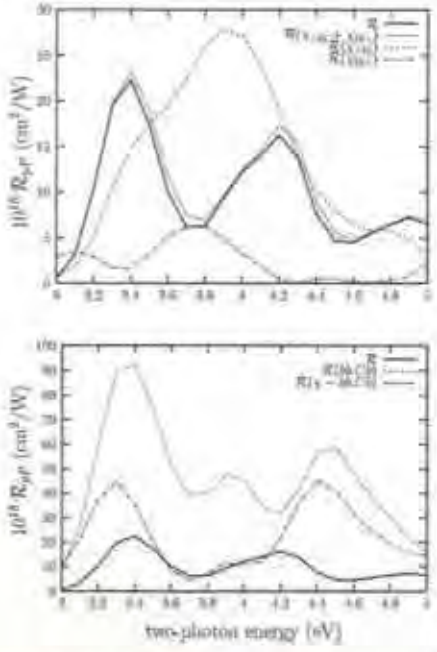

Figure 5.3: In the top panel, we show the SHG radiation for the sum of $\chi_{\parallel\perp}$ and $\chi_{\perp\parallel\parallel}$ which reproduce well $\mathcal{R}_{pp}$ for 36 planes. Also we can see the $\mathcal{R}$ for both χ susceptibilities. In the bottom panel, we show the SHG radiation for the contributions of the nonlinear susceptibility tensor $\overleftrightarrow{\chi}$ of the bulk states in the valence band to the bulk states in the conduction band, with a transition into a virtual bulk state in the conduction band ($bb.Cb$), where we observe the inversion of the resonances. On the other hand, when we calculate the SHG radiation without this contribution, the inversion is not observed ($\chi - bb.Cb$).

checked that using 183 or more the spectra are basically the same. In connection with the k-points, is the issue of the surface (111) symmetry restriction given by Eq. (5.1d). Indeed, if the number of k-points is not enough, this symmetry is not satisfied.

Another important point is the behavior of the SHG spectra with respect to the atomic positions for this surface. For instance, changing the Si-H distance as much as 5% of its equilibrium value, does not alter the SHG spectra appreciably (see Fig. 5.4). On the other hand, changing the vertical position of the back-bonded Si in the second layer, induces changes in the spectra. Fig. 5.4 shows $\mathcal{R}_{pp}$ (*ab-initio*) for a vertical displacement of the back-bonded Si towards the surface (bulk) of 30% of its length (which is equivalent to a Si-Si bond-length change

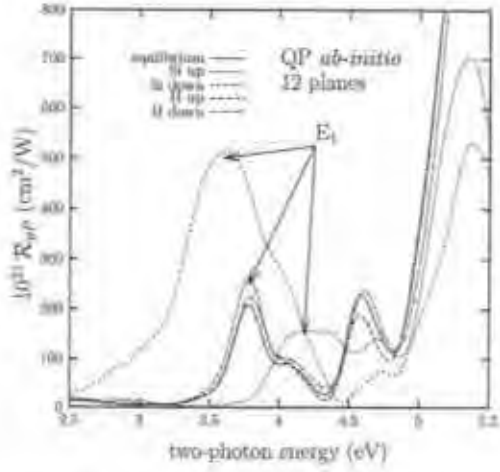

Figure 5.4: *ab-initio* $\mathcal{R}_{pp'}$ for 12 planes by moving the back-bonded Si by 30% up (dots) or down (short-dashes) and the H by 5% up (long-dashes with dots) or down (short-dashes with dots) from its equilibrium position (solid line).

of only 3%), that clearly shows a blueshifted (redshifted) E_1 peak. Although the vertical displacement is artificial and does not give an equilibrium structure, they show the surface sensitivity of SHG. A similar result follows for $\mathcal{R}_{ps}$. It is interesting to notice that the lack of sensitivity of SHG to the H bond and its large sensitivity to the back-bonded Si is in agreement with Ref. [109] where it is found that this Si presents more surface like behavior, in the sense that a chemical agent is more propense to interact with this Si (or H), than any other Si including the surface Si. If this interaction induces relaxation of the back-bonded Si, SHG could be used to monitor such process. This idea could be applied to the results of Ref. [68], where SHG measurements of Si(111) with several chemical modifications have been made.

An important issue in SHG is the screening of the electric field that induces the non-linear response. As explained in [32], the fundamental field used in the evaluation of $\overleftrightarrow{\chi}$ is simply given by the Fresnel screening of external field, and thus the contribution of the different components of $\overleftrightarrow{\chi}$ towards $\mathcal{R}$, are weighted accordingly. Besides this, there is also the important fact of the prefactors in Eqs. (5.3), for the visible range it follows that $\sin^2\theta < k_\perp^2(\omega) < k_\perp(\omega)k_\perp(2\omega)$, and although the different components of $\overleftrightarrow{\chi}$ may be of the same order, $\chi_{\parallel\parallel\perp}$ has the larger prefactor. As such, for Si(100) it is found that $\chi_{\parallel\parallel\perp}$ dominates the

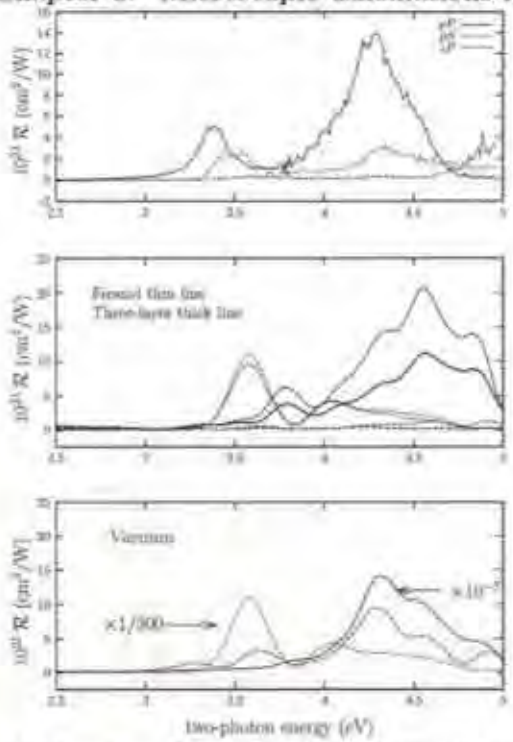

Figure 5.5: $\mathcal{R}$ for 36 planes vs different models of screening, for pP (solid), pS (dotted) and sP (dashed) polarization. Top panel are the experimental results. Middle panel are the Fresnel (thin lines), and the three-layer-model (thick line) results. Bottom panel is the vacuum model, that represents no screening. Note the factors by which the vacuum results need to be multiplied in order to be seen on the same vertical scale.

spectra and the contribution of $\chi_{\perp\parallel\parallel}$ and $\chi_{\perp\perp\perp}$ are negligible [27]. Although the theoretical evidence is strong, the lack of experimental measurements for other than pP polarization, still leaves some room for improper screening, thus allowing for the possibility of a larger contribution from $\chi_{\perp\parallel\parallel}$ and in particular of $\chi_{\perp\perp\perp}$. With the measurement of pP, pS, and sP spectra of the Si(111)(1 × 1) surface, we can conclusively answer for the first time how accurate the screening is in the model for $\mathcal{R}$ and $\overleftrightarrow{\chi}$. In Fig. 5.5 we show $\mathcal{R}$ (*ab-initio*) for the case where the screening is simply given by the Fresnel factors (evaluated with the bulk dielectric function), for the case where the screening is given by the three-layer model, in which the non-linear conversion takes place in an small surface region characterized by a surface dielectric function ϵ_ℓ (see Sec. 2.3) , and for the case where the fields

are evaluated above the surface, i.e. in vacuum, that represents no screening at all. Notice that the Fresnel and three-layer models give very similar spectra, that agrees rather well in lineshape and intensity with the experiment. Thus, $\chi_{\parallel\parallel\perp}$ dominates $\mathcal{R}$, with a small contribution from $\chi_{\perp\parallel\parallel}$ at high energies. On the other hand, for the vacuum case, $\chi_{\perp\perp\perp}$ dominates, but the spectra is in disagreement both in lineshape and intensity with the experiment. For instance, $\mathcal{R}_{pP}$ is six orders of magnitude larger than $\mathcal{R}$ for the other polarizations. Similar conclusions follow from the SETB approach. Therefore, the present calculation along with the experiments, allow us to conclude that the screening is properly accounted for by the Fresnel approximation. Although, this conclusion was derived for the present surface, we think that it also applies to other semiconductor surfaces.

5.4 Conclusions

We have presented a microscopic calculation of SHG for the Si(111):H(1×1) surface. We have used two different schemes, one is the semi-empirical tight-binding (SETB) method and the other is an *ab-initio* method based on the DFT-LDA. With the SETB method, the spectra converge as a function of the number of planes but have an anomalous behavior in the magnitude of their predicted E_1 and E_2 resonances. Our results are in good agreement with the experimental data, i.e. $\mathcal{R}(E_1) < \mathcal{R}(E_2)$ up to 18 planes, but as more planes are included to achieve convergence, the magnitude of the peaks change giving $\mathcal{R}(E_1) > \mathcal{R}(E_2)$. This anomalous behavior is traced to the existence of surface states (resonant with bulk states), whose influence diminishes as we increase the size of the slab. In the *ab-initio* method this does not occur, the magnitude of $\mathcal{R}$ for E_1 and E_2 is in agreement with the experimental spectra regardless of the number of planes, although the convergence of the signal is slower. The inclusion of QP corrections gives very good results for pP polarization, and for pS the E_2 peak is redshifted from its experimental position. However, the QP correction has not the same value for both cases, showing how the components of $\overleftrightarrow{\chi}$ may be driven by different mechanisms. Also, we find that the SHG spectra are produced by the interference of $\chi_{\parallel\parallel\perp}$ and $\chi_{\perp\parallel\parallel}$, in contrast with the Si(100) surface, in which the susceptibility $\chi_{\parallel\parallel\perp}$ dominates. The sensitivity of SHG to the back-bonded Si supports the conclusion of Ref. [109], by which this atom seems to be the only one chemically active for this surface. Further, the screening of the fundamental field that excites

the non-linear process is well given by the Fresnel approximation. We can conclude that both SETB and *ab-initio* methods give qualitatively similar results for this surface. Further improvements of our scheme and more refined experiments, will keep on rendering SHG as a very powerful and useful surface tool.

Chapter 6

SHG from Si(111)7×7, SETB vs. experiment

In this Chapter, we consider the most fascinating of all semiconductor surfaces, the Si(111) surface with a 7×7 reconstruction. The unit cell of this huge reconstruction has 49 atoms and is seven times larger than the simple 1×1 reconstruction treated in the previous Chapters. The computational burden of this surface is only possible through the semi-empirical tight binding (SETB) approach, an *ab-initio* calculation is just out of the question for SHG.

As we have seen in the previous Chapters, SHG is a very powerful tool to study surface phenomena, and its application to Si(111)7×7 is no exception. Three experimental groups have done excellent experiments, two of which have done spectroscopy [18,117] and one fixed frequency measurements [7]. We mention that this surface has been investigated with linear optical techniques, and an excellent account could be found in Ref. [118] and Ref. [119], and references therein.

In this Chapter we first review the morphologic characteristics of the reconstructed surface and its implication on the symmetry of $\overleftrightarrow{\chi}$, and then we compare the theoretical results with the experiments. Conclusions and an outlook of future possible experiments will be given afterwards.

6.1 Symmetry of a Si(111)7×7 surface

We follow the Adatom-Stacking Fault (DAS) model of Takayangai *et al.* [120] to describe the atomic arrangement of the surface, from which the SHG is calculated.

In Fig. 6.1 we show the DAS model that has the following morphology. The unit cell of the first atomic plane only has 42 atoms, instead of 49, due to a fault in the piling of the planes. This fact can bee seen from Fig. 6.1 as these atoms are symmetrically situated with respect to the minor diagonal of the unit cell. On top of this plane, there are 12 adatoms (ADs) that saturate 36 of the 42 dangling bonds (DBs) of the atoms of the first plane. The remaining 6 atoms with unsaturated dangling bonds are called the restatoms (RAs). Some atoms from the second plane are displaced laterally in such a way that they form a bond called a dimer. There are 9 dimers at the boundary of the unit cell, that divide the cell in two subunits. One subunit has the piling fault of the first atomic plane (faulted subunit), and the other does not (unfaulted subunit). Due to this fault and the dimer formation, the second plane has only 48 atoms instead of 49. The missing atom corresponds to a hole at the corner or corner hole (CH), and there is one per unit cell. The CH is surrounded by a ring of atoms that belong to the first and second planes, therefore the atoms in the third plane associated with the CH is unsaturated, and then with the 12 ADs and the 6 RAs, there are 19 dangling bonds per unit cell. The rather small number of dangling bonds reduces the surface energy. The atoms of the next planes do not change much their in-plane positions, however some of them show large vertical displacements. For instance atoms of the second and third plane that are just below the ADs have vertical displacements up to ~ 0.5 Å towards the bulk. In general the ADs and RAs in the faulted subunit are $\sim 0.1 - 0.2$ Å above their analogs in the unfaulted subunit. The ADs close to the CH, are called the corner ADs and the ones in the center and close to the minor diagonal, are called the center ADs. In short, the DAS model has 6 corner ADs, 6 center ADs, 6 RAs and 1 CH that give 19 DBs, plus 9 dimers and the piling fault along the minor diagonal of the unit cell, that divides the cell in two subunits, one faulted and one unfaulted.

Recent molecular dynamic *ab-initio* calculations have shown that the DAS model is energetically favorable as compared with other models [121]. The atomic positions are taken from these *ab-initio* calculations [122]. Below the third atomic plane, the atomic positions are bulk like.

In Chapter 4, we mentioned that an ideal 1×1 (111) surface satisfies the following symmetry relationship of $\overleftrightarrow{\chi}$,

$$\chi_{xxz} = -\chi_{yyz} = -\chi_{xyy}. \tag{6.1}$$

First, these components are different from zero due to the fact that the xy plane

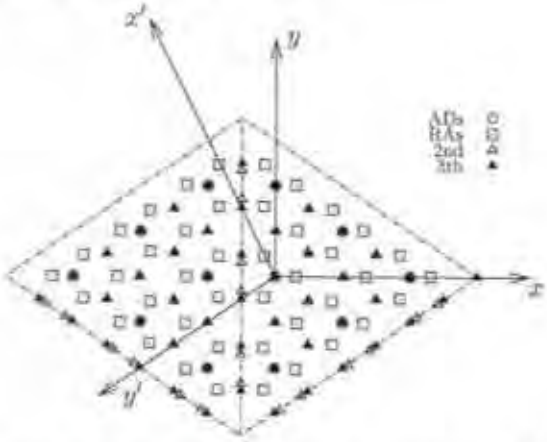

Figure 6.1: We show the three first planes plus the adatoms (ADs) for a Si(111)7×7 surface, according to the Adatom-Stacking Fault (DAS) model. The xy and $x'y'$ axes are rotated by 120°. The rhomboid with dashed lines denotes the unit cell, and the minor diagonal can be seen as a dashed vertical line. Note that with respect to the ADs, the RAs do not satisfy the 120° rotational symmetry. The same is true between other surface of planes.

is not a mirror plane, and they follow Eq. (6.1) since there is 120° symmetry operation at this surface. That is, rotating the coordinate system by 120 degrees, we get exactly the same environment for any given atom of the unit cell (only one atom for the 1 × 1). This environment involves not only the atoms on the same plane but also, and more importantly, the atoms in the neighboring planes. If we take any of the atoms in the first 3 planes or the ADs, we see from Fig. 6.1, that this 120 degree symmetry is not satisfied. The environment due to the atoms in the planes above or below make the original coordinate system to be inequivalent with the rotated one, thus although the zy plane is still not a mirror plane, the restriction of Eq. (6.1) should not longer hold. Then, in general for a reconstructed DAS 7 × 7 Si(111) surface, we have that

$$\chi_{xxz} \neq \chi_{yyz} \neq \chi_{xyy} \neq 0 \qquad (7 \times 7 \quad (111) \text{ surface}). \tag{6.2}$$

This fact implies that the symmetry shown by $\mathcal{R}$ in its azimuthal rotation could be different from the six-fold symmetry of the ideal 1 × 1 unit cell. In the next section, we show that indeed the 7 × 7 shows a different symmetry through the SHG spectrum.

6.2 Results

We begin this section by writing the appropriate radiation factors for this surface in view of the reduced symmetry imposed by Eq. (6.2). Using the corresponding equations of Chapter 2 (Eqs. (2.66) and (2.67)), we get that

$$\begin{aligned} r_{pp} &= \frac{1}{4}[4\sin\theta\epsilon_b(2\omega)\left(\sin^2\theta{\epsilon_b}^2(\omega)\chi_{zzz}+\epsilon_\ell{}^2(\omega)k_{zb}\chi_{zxx}\right) \\ &+ \epsilon_\ell(\omega)\epsilon_\ell(2\omega)k_{zb}(\omega)k_{zb}(2\omega)[-8\sin\theta\epsilon_b(\omega)\chi_{zxx} \\ &+ \epsilon_\ell(\omega)k_{zb}(\omega)((3\chi_{xxx}+\chi_{xyy}+2\chi_{yyx})\cos\phi \\ &+ (\chi_{xxx}-\chi_{xyy}-2\chi_{yyx})\cos 3\phi)]], \end{aligned} \tag{6.3}$$

$$\begin{aligned} r_{sp} &= \frac{1}{4}[4\sin\theta\epsilon_b(2\omega)\chi_{zxx}+\epsilon_\ell(2\omega)k_{zb}(2\omega)((\chi_{xxx}+3\chi_{xyy}-2\chi_{yyx})\cos\phi \\ &+ (-\chi_{xxx}+\chi_{xyy}+2\chi_{yyx})\cos 3\phi)], \end{aligned} \tag{6.4}$$

$$\begin{aligned} r_{pS} &= \frac{1}{4}\epsilon_\ell{}^2(\omega)k_{zb}^2[(-\chi_{xxx}-3\chi_{xyy}+2\chi_{yyx})\sin\phi \\ &+ (-\chi_{xxx}-\chi_{xyy}-2\chi_{yyx})\sin 3\phi], \end{aligned} \tag{6.5}$$

and

$$\begin{aligned} r_{sS} &= \frac{1}{4}[(-3\chi_{xxx}-\chi_{xyy}-2\chi_{yyx})\sin\phi \\ &+ (\chi_{xxx}-\chi_{xyy}-2\chi_{yyx})\sin 3\phi]. \end{aligned} \tag{6.6}$$

If we take $\epsilon_\ell = \epsilon_b$ and use Eq. (6.1), we get the same results as those of a 1×1 symmetry (see Eq. (5.3)). From r_{ij} we see that superimposed to the 6-fold symmetry, related to 3ϕ, there is a modulation given by ϕ. In what follows, we use the Fresnel model for screening, then we take $\epsilon_\ell = \epsilon_b$.

Following the SETB procedure explained in the previous Chapters, we calculate SHG. Before comparing the theoretical results with the experiments, we discuss some important issues concerning the consistency of the numerical calculation. To this end we have chosen three different slabs. All have 4 surface planes (reconstructed) on the front surface. One slab has three bulk planes and the back surface is ideally terminated with H saturating the corresponding Si (dangling) bonds, we call it the H-surface. The other two slabs have a reconstructed back

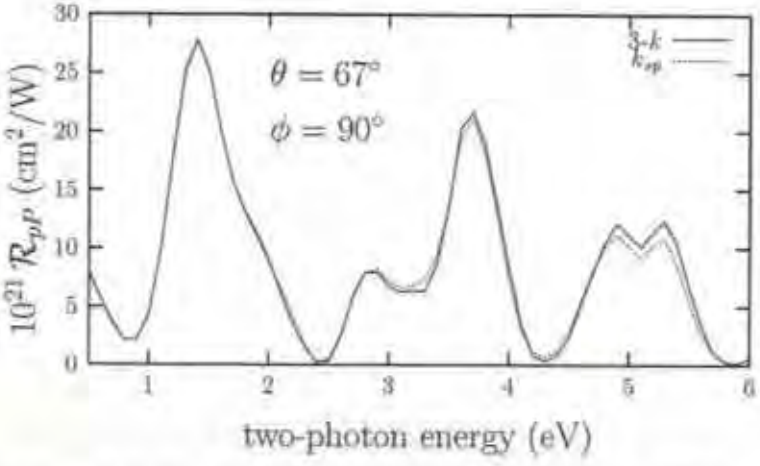

Figure 6.2: $\mathcal{R}_{pP}$ vs. the two-photon energy for the H-surface slab. The solid (dotted) line is for 3 (sp) k-points in the 2DBZ.

surface, and only differ in the number of bulk planes, one has 2 and the other 6, thus we refer them by the total number of planes. Then we have a 10 planes and a 14 planes slabs (with no H).

One advantage of the large unit cell in real space, is that in reciprocal space it is 49 ($= 7 \times 7$) smaller, and then only very few k-points are required to sum over the irreducible part of the two-dimensional Brillouin zone (2DBZ). Indeed, we have checked that by using only one point of maximum symmetry the SHG spectra are converged as far as the k-sum is concerned. This point is the well known Baldereschi point k_{sp} [123]. In Fig. 6.2 we show $\mathcal{R}_{pP}$ for the H-surface slab, for 3-k points and only the sp point, where we see that sp is enough to get a converged spectrum. Thus, all the results shown in the next figures are for the sp point. The angles chosen are those of the experiments, where with $\phi = 90°$ the anisotropic contribution to pP, coming from χ_{xxz}, χ_{xyy} and χ_{yyx} vanishes (see Eq. (6.3)). The broadening used in the Kramers-Kronig transformation is set to 75 meV.

Another important issue is the way of simulating the semiinfinite system. For this as we mention before we use a slab. In this case we can use, in principle, a slab with two identical surfaces or with one surface H-terminated. However, as we can see from Fig. 6.3, the SHG spectrum is not the same, and thus we have to discard the H-terminated slab as a possibility for doing the SHG calculations.

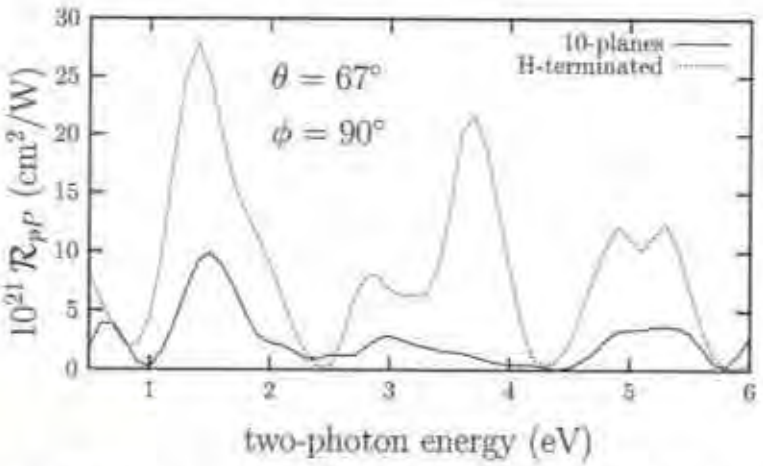

Figure 6.3: $\mathcal{R}_{pP}$ vs. the two-photon energy for the H-surface slab (dotted line) and for the 10 planes slab with the two reconstructed surfaces (solid line).

In the previous Chapters, the slabs used for Si(100)$c4 \times 2$ and Si(111)1×1, have identical front and back surfaces. We mention that in Ref. [118], it is claimed that the linear optical response below 4.5 eV is basically the same for both slabs, but we see that this is not longer correct for SHG.

The large number of atoms forbids to check for a full convergence as the number of planes in the slab is increased, however we have done two slabs of 10 and 14 planes to check on this issue. In Fig. 6.4 we show $\mathcal{R}_{pP}$ for the two slabs with both front and back surface reconstructed. We see that below 1 eV the spectra are different, for 10 planes we see a peak that is absent from the 14 planes, however above 1 eV the three SHG resonances shown by the spectra of both slabs coincide in energy. Although the intensity and detailed lineshape of both spectra are not the same, the qualitative features are preserved as we increased the number of atomic planes. Since going above 14 planes is numerically very difficult, we take the 14 planes slab as our reference for a qualitative comparison with the experiments, and leave the computational challenge of larger slabs for a more refined calculation.

In Fig. 6.5 we show $\mathcal{R}$ for pP, sP and pS, along with the corresponding experimental results of Ref. [18]. The angles chosen are those of the experiments, $\theta = 67°$ and $\phi = 90°$. The theoretical curves have been shifted by 0.2 eV, in order to have a better agreement with the experiment. As mentioned before, this kind of shifting is usual in SETB calculations, and is due to the inherent approximations

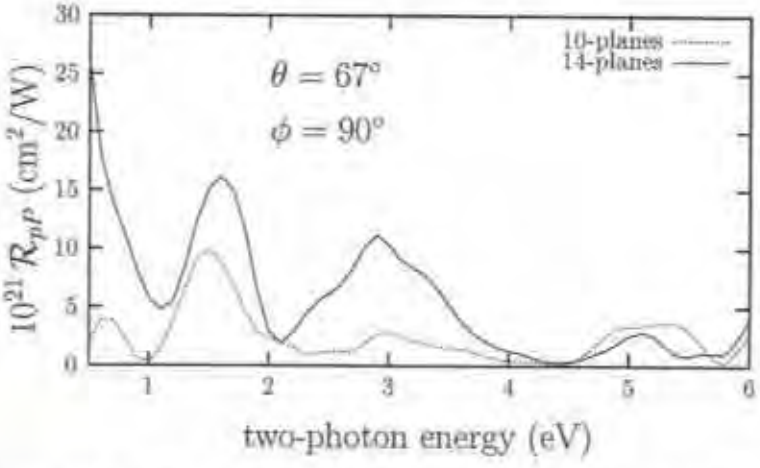

Figure 6.4: $\mathcal{R}_{pP}$ vs. the two-photon energy for the 10-planes slab (dotted line) and the 14-planes slab (solid line). Note that above 1 eV the three SHG peaks coincide in energy.

of the method. The experimental curve for pP has been rescaled to coincide with the theoretical intensity, and the same scaling is applied to sP and pS. The peak above 1.6 eV is E_1, which is reproduced in the three spectra, although with some extra shifting for sP and pS. The theoretical intensity for sP has been multiplied by 30 and pS by 0.3 in order to follow experimental results. Below 1.6 eV, both sP and pS show a broad peak that is well reproduced only by the calculated pS. For pP this feature is absent in theory and experiment. As can be seen from Eqs. (6.3)-(6.5) and recalling that $\phi = 90°$, pP depends on the isotropic components of $\overleftrightarrow{\chi}$, i.e. χ_{zzz}, χ_{zxx} and χ_{xxz}, and sP on χ_{xxx}, whereas pS on the anisotropic ones, χ_{xxx}, χ_{xyy} and χ_{yyx}. Thus the different polarizations relate to different components of $\overleftrightarrow{\chi}$ and in particular for pP is the χ_{xxz} component the one that dominates with some small interference coming from χ_{xxx} and χ_{zzz}.

In order to see the effects of the lower symmetry of this surface, we concentrate on the pS polarization which only depends on the anisotropic components of $\overleftrightarrow{\chi}$ (see Eq. (6.5)). For this combination of polarization there are two sets of experimental data, both done for normal incidence ($\theta = 0$) and for $\phi = 90°$. One is from Ref. [125] where $\mathcal{R}_{pS}$ is studied as a function of temperature, the other is from Ref. [124] that does the experiment at room temperature and as a function of

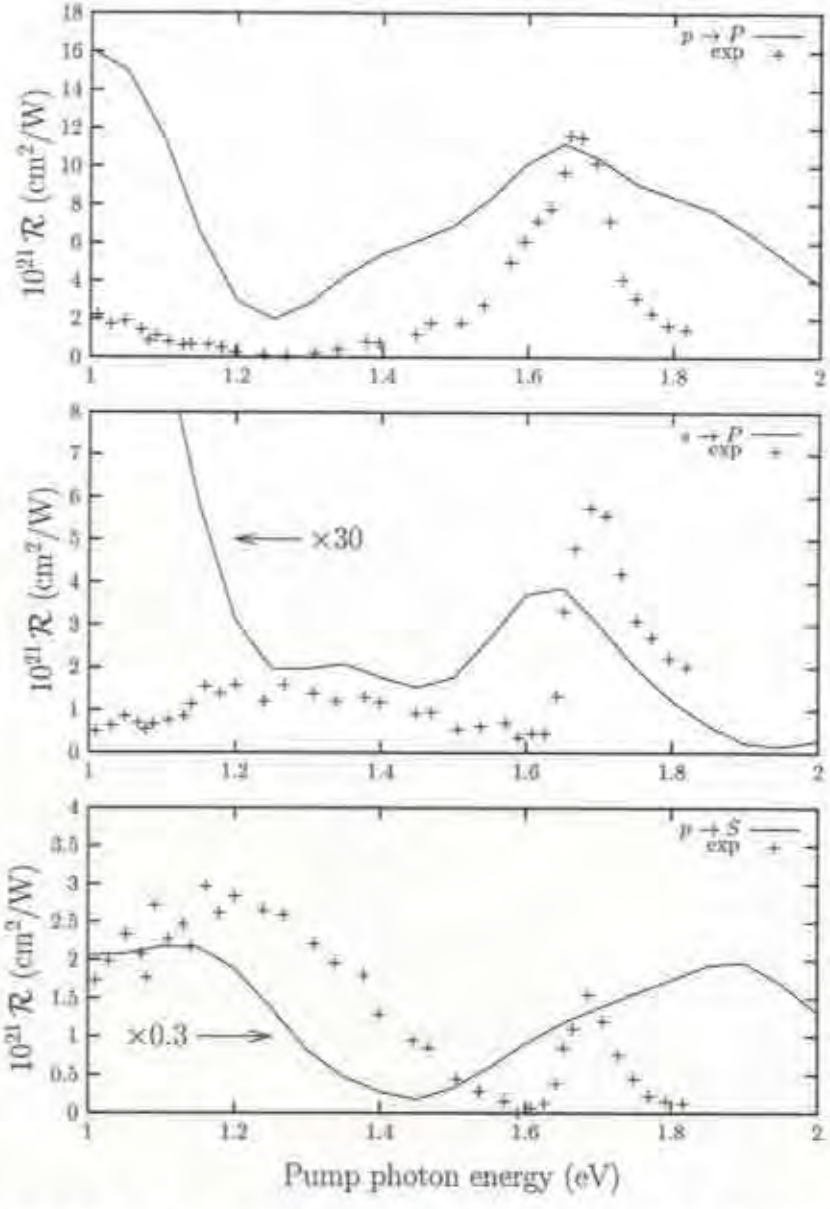

Figure 6.5: $\mathcal{R}$ vs. the photon energy for the 14-planes slab for pP (top), sP (middle) and pS (bottom) polarizations. The experimental results are from Ref. [18] and have been rescaled on the vertical axis by the same amount. The theoretical curves are shifted by 0.2 eV. See text for details

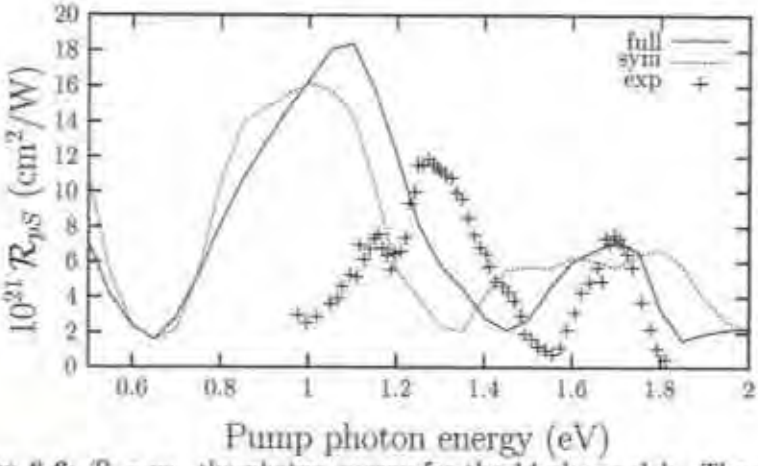

Figure 6.6: $\mathcal{R}_{pS}$ vs. the photon energy for the 14-planes slab. The solid line is the full calculation using Eq.(6.2), and the dotted line is assuming the symmetry of Eq. (6.1). The experimental results are from Ref. [124] and have been rescaled on the vertical axis by the same amount. The theoretical curves are shifted down by 0.6 eV. See text for details.

oxygen content. Under the same conditions, both sets of experiments coincide. In Fig. 6.6 we compare the theoretical spectrum with the experimental results of Ref. [124]. We have shifted down in energy the theoretical spectra by 0.6 eV and the experimental data has been rescaled on the vertical axis. We see that the spectrum for the full calculation that assumes Eq. (6.2), reproduces much better E_1 ($\sim$ 1.7 eV), than the spectrum for the symmetric case of Eq. (6.1). For the surface peak, we see that both spectra are similar. This behavior is similar to the one found for the Si(100)c4 $\times$ 2 single domain surface of Chapter 3. To wit, the surface related SHG resonances sample more the inplane electronic structure, than the bulk related ones, due to the coupling of the out-of-plane wave function. Thus, E_1 is more sensitive to the symmetry imposed by the coupling of the atomic layers out-of-plane, i.e. Eq. (6.1) is satisfied for surface resonances, whereas Eq. (6.2) for bulk resonances. The experimental spectrum shown in Fig. 6.6 confirms this hypothesis.

To see the azimuthal dependence of $\mathcal{R}$ we take again the pS polarization at normal incidence, and show in Fig. 6.7, the variation of the SHG as a function of the incoming photon energy and azimuthal angle ϕ. We see that for most of the

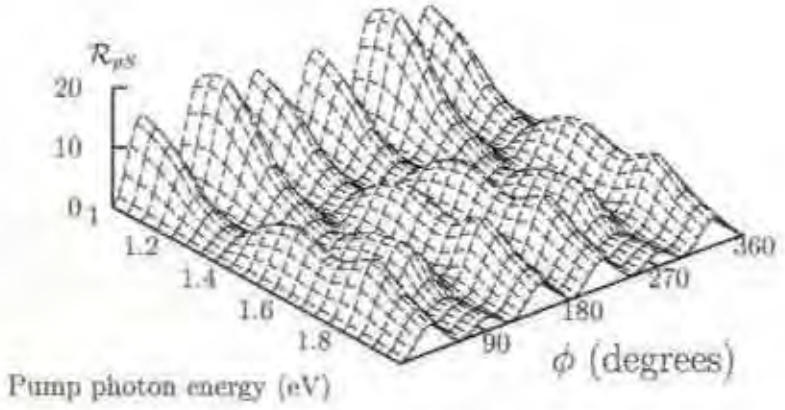

Figure 6.7: $\mathcal{R}_{pS}$ vs. the photon energy and the azimuthal angle ϕ for the 14-planes slab at normal incidence. The deviation from a full six-fold symmetry is apparent. The figure below shows the SHG traces instead of the 3D surface.

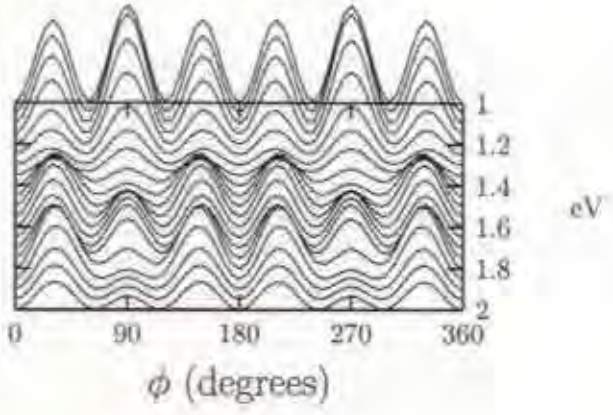

energies the 6-fold symmetry is broken, but there are some selected frequencies for which the 6 peaks have equal magnitudes, showing the full 6-fold symmetry. This happens at low energies as we discussed in the previous paragraph. Also notice that for some other frequencies around E_1, the deviation from the 6-fold symmetry is rather small, as the height of the peaks at $\phi = 90°$ and $270°$, is very similar to the other 4 peaks. Thus, to confirm this prediction one has to do experiments at the most convenient frequencies, where this difference is much larger. We mention that we have checked that if we use an ideal 7×7 unit cell, the 6-fold symmetry is fully satisfied, and thus this effect that lowers the symmetry is a true consequence of the geometry of this surface. Again, SHG is very sensitive to this symmetry breaking for the bulk resonances.

To complete this study, we would need to investigate the origin of the SHG surface resonances, for instance the one shown in the normal incidence results of Fig. 6.6. To this end, we could follow the procedure of Ref. [31], in order to investigate the electronic and spatial origin of the SHG resonances. In that work, a full decomposition of the susceptibility into surface and bulk real and virtual one-photon and two-photon transitions is done, and thus it is possible to fully investigate the origin of any SHG resonance. However, this goes beyond the scope of the present thesis. Nevertheless, we can say that these surface resonances are related to well known electronic surface states of this reconstruction. Indeed, various techniques have shown the existence of three filled surface states below/above the Fermi level: S_1 at ~ -0.2 eV, S_2 at ~ -0.8 eV, and S_3 at ~ -1.8 eV, and two empty surface states: U_1 at ~ 0.5 eV, and U_2 at $1.3 - 1.5$ eV [117]. Within the DAS model, these states are attributed: S_1 to the adatom dangling bond, S_2 to the RA dangling bond, S_3 to the back-bond of the adatoms and the corner-hole atoms, U_1 to the adatom dangling bond, and U_2 to the adatom back antibond. Thus, following Ref. [125], we can attribute the SHG surface peak to a convolution of one-photon $S_2 - U_1$ transitions and two-photon $S_3 - U_1$ transitions. As we say, a full treatment following Ref. [31] remains to be done.

6.3 Conclusions

In this Chapter we have investigated the SHG of the largest surface reconstruction known for Si, the Si(111)7×7. The computational burden is of paramount proportions, and we were able to solve a 14 layer slab of 596 atoms. The calculated non-linear optical properties show good qualitative agreement with the available

experiments. In particular, the experiments confirm the theoretical prediction of the lowering of the 6-fold symmetry displayed by an ideal 1×1 reconstruction, which is believed to be followed also by the 7×7 reconstruction [7]. The discrepancies between theory and experiment leave room for improvement, but what comes out very clearly is that SHG is indeed a very powerful surface spectroscopy from which many interesting physical aspects can be studied.

Chapter 7

Conclusions

In this work, we showed the importance of nonlinear optics in the study of the physical properties of surfaces. In particular, we used second harmonic generation (SHG) to investigate several nonlinear optical properties of Si surfaces. We have analyzed SHG for a Si(100)c(4×2) single domain surface applying the semi-empirical tight binding (SETB) method. Furthermore, we have used three different approaches to obtain the optical spectra in Si(111):H (1×1); the phenomenological polarizable bond model (PBM) and two microscopic formulations which are the SETB method and the *ab-initio* calculation. The results obtained by these models show a good agreement with the available experimental data. We studied the symmetry of both surfaces, and proposed different classes of symmetries that could be studied with SHG. The sensitivity of SHG to the backbonds was studied, and we find that the SHG can be used to monitor the chemical modifications of Si(111) surfaces.

In Chapter 3, we have calculated the SHG spectra of a single-domain Si(100) surface with a c(4 × 2) reconstruction. The concomitant formation of the dimers as the surface relaxes to its equilibrium configuration gives a surface with C_{1v} symmetry. The anisotropies shown by the SHG radiated efficiency $\mathcal{R}$ are related to the spatial localization of the electronic transitions of the particular SHG resonance. For surface resonances the SHG spectrum shows a C_{2v} symmetry, which implies $\mathcal{R}_{pP}(0°) = \mathcal{R}_{pP}(180°)$, $\mathcal{R}_{sP}(0°) = \mathcal{R}_{sP}(180°)$, $\mathcal{R}_{pS}(45°) = \mathcal{R}_{pS}(135°)$, and $\mathcal{R}_{sS}(45°) = \mathcal{R}_{sS}(135°)$. In contrast, for the bulk SHG resonances that sample the energy states of atoms below the dimer atoms, the symmetry of the spectrum is reduced to a C_{1v} class, for which $\mathcal{R}_{pP}(0°) \neq \mathcal{R}_{pP}(180°)$, $\mathcal{R}_{sP}(0°) \neq \mathcal{R}_{sP}(180°)$,

and $\mathcal{R}_{pS}(45°) \neq \mathcal{R}_{pS}(135°)$. We called this a π-asymmetry. Concentrating on E_1 we explain its behavior for the different polarization combinations of incoming (fundamental) and outgoing (SH) beams in terms of the radiation formulas and the different components of the non-linear susceptibility tensor $\overleftrightarrow{\chi}$. The spectra shown by this calculation show a rich and complex structure that should be experimentally explored.

In Chapter 4, we conclude that SHG is very sensitive to back-bond changes for a Si(111):H (1×1) surface, and that by use of the PBM we can obtain qualitative information which gives physical insight into the non-linear optical phenomena taking place. Although the PBM overestimates the SHG intensities and gives the pS yield smaller than the pP yield, the line-shape and energy position of the E_1 SHG peak follows the correct experimental trend. The PBM is driven by the local-field effect, that for this surface shows clearly how the inversion symmetry is broken in the surface region, and how the spatial position of the bonds determines SHG. The less computational demanding and easier to interpret PBM calculations are very useful to study surface SHG and could complement the more rigorous microscopic models.

In Chapter 5, we have presented a microscopic calculation of SHG for the Si(111):H(1 × 1) surface. We have used two different schemes, one is the semi-empirical tight-binding (SETB) method and the other is an *ab-initio* method based on the DFT-LDA. With the SETB method, the spectra converge as a function of the number of planes but have an anomalous behavior in the magnitude of their predicted E_1 and E_2 resonances. Our results are in good agreement with the experimental data, i.e. $\mathcal{R}(E_1) < \mathcal{R}(E_2)$ up to 18 planes, but as more planes are included to achieve convergence, the magnitude of the peaks change giving $\mathcal{R}(E_1) > \mathcal{R}(E_2)$. This anomalous behavior is traced to the existence of surface states (resonant with bulk states), whose influence diminishes as we increase the size of the slab. In the *ab-initio* method this does not occur, the magnitude of $\mathcal{R}$ for E_1 and E_2 is in agreement with the experimental spectra regardless of the number of planes, although the convergence of the signal is slower. The inclusion of QP corrections gives very good results for pP polarization, and for pS the E_2 peak is redshifted from its experimental position. However, the QP correction has not the same value for both cases, showing how the components of $\overleftrightarrow{\chi}$ may be driven by different mechanisms. Also, we find that the SHG spectra are produced by the interference of $\chi_{\parallel\parallel\perp}$ and $\chi_{\perp\parallel\parallel}$, in contrast with the Si(100) surface, in which

the susceptibility $\chi_{\parallel\parallel\perp}$ dominates. The sensitivity of SHG to the back-bonded Si supports the conclusion of Ref. [109], by which this atom seems to be the only one chemically active for this surface, and corroborates the PBM model. Further, the screening of the fundamental field that excites the non-linear process is well given by the Fresnel approximation. We can conclude that both SETB and *ab-initio* methods give qualitatively similar results for this surface.

Finally, in Chapter 6 we have investigated the SHG of the largest surface reconstruction known for Si, the Si(111)7 $\times$ 7. The computational burden is of paramount proportions, and we were able to solve a 14 layer slab of 596 atoms. The calculated non-linear optical properties show good qualitative agreement with the available experiments. In particular, the experiments confirm the theoretical prediction of the lowering of the 6-fold symmetry displayed by an ideal 1×1 reconstruction, which is believed to be followed also by the 7×7 reconstruction [7].

The study of surfaces has been consolidated as an important field in physics. In the next years, the progress in surface science will lead to new technological development. However, to be able to understand better the physical processes involved, more theoretical calculations need to be done. The future work based on this thesis will be to study the effects of hydrogen on the Si(111) (7×7) surface and to observe the surface sensitivity to the backbonds. An analysis of the different contributions of the nonlinear susceptibility is necessary to understand which of the atomic transitions produce the SHG. Therefore, we will be able to know if the transitions come from the surface states or from the bulk states. These important aspects should be studied for the different surfaces considered in this work.

We can conclude that the optical SHG technique is a very versatile *surface sensitive* probe to analyze surfaces and interfaces, which offers unique advantages over other surface probes: does not require ultra-high vacuum environments, is non-invasive, non-destructive and has a wide spectral range.

Further improvements of our schemes and more refined experiments, will keep on rendering SHG as a very powerful and useful surface tool. The discrepancies between theory and experiment leave room for improvement, but what comes out very clearly is that SHG is indeed a very powerful surface spectroscopy from which many interesting physical aspects can be studied. The future of the non-linear optical probes for surface physics, hinges on the dialog between theory and experiment, and the present thesis constitutes yet another big leap in this process.

Appendix A

Publication list

Part of the research of this thesis is published in the following articles:

1. N. Arzate, J. E. Mejía, Bernardo S. Mendoza and Rodolfo Del Sole, *D.C.-electric-field modified second-harmonic-generation at the Si(100)*, Appl. Phys. B, **68** 629, (1999).

2. J. Mejía and B. S. Mendoza, *Second-harmonic generation from single-domain Si(100) surfaces*, Surface Science, **487** 180-109, (2001).

3. J. E. Mejía and B. S. Mendoza, *Polarizable-bond model for surface second-harmonic generation at Si(111):H (1×1)*, Phys. stat. sol. (a), **188** (2001).

4. J. E. Mejía, Bernardo S. Mendoza, M. Palummo, G. Onida, R. Del Sole, S. Bergfeld and W. Daum, *Surface Second harmonic generation at Si(111):H* (1×1), Phys. Rev. B *To be sent.*

5. J. E. Mejía, Bernardo S. Mendoza, M. Palummo, G. Onida, R. Del Sole, S. Bergfeld and W. Daum, *Theoretical approaches to surfaces second harmonic generation vs. experiment: Si(111):H* (1×1) *as a test case.*, Phys. Rev. B *To be sent.*

6. J. E. Mejía and Bernardo S. Mendoza, *Suface second harmonic generation at clean H covered Si(111)* (7×7)., Phys. Rev. B *To be sent.*

References

[1] P. A. Franken, A. E. Hill, C. W. Peters, and G. Weinreich, *Generation of optical harmonics*, Phys. Rev. Lett. **7**(4), 118 (1961).

[2] N. Bloembergen and P. S. Pershan, *Light waves at the boundary of nonlinear media*, Phys. Rev. **128**, 606 (1962).

[3] N. Bloembergen, R. K. Chang, S. S. Jha, and C. H. Lee, *Optical second harmonic generation in reflection from media with inversion symmetry*, Phys. Rev. **174**(3), 813 (1968).

[4] N. Bloembergen, *Surface nonlinear optics: a historical overview*, Appl. Phys. B **68**, 289 (1999).

[5] H. J. Simon, D. E. Mitchell, and J. G. Watson, Phys. Rev. Lett. **33**, 1531 (1974).

[6] X. D. Shu, Y. R. Shen, and R. Carr, Surf. Sci. **163**, 114 (1985).

[7] T. F. Heinz, M. M. T. Loy, and W. A. Thomson, Phys. Rev. Lett. **54**, 63 (1985).

[8] H. I. Smith and H. G. Craighead, *Nanofabrication*, Physics Today p. 24 (February 1990).

[9] Q. Du, R. Superfine, E. Freysz, and Y. R. Shen, Phys. Rev. **70**, 2313 (1993).

[10] T. Rasing, Y. R. Shen, M. W. Kim, and S. Grubb, Phys. Rev. Lett. **55**, 2903 (1985).

[11] W. Daum, H.-J. Krause, U. Reichel, and H. Ibach, *Nonlinear optical spectroscopy at silicon interfaces*, Physica Scripta **T49**, 513 (1993).

[12] W. Daum, H.-J. Krause, U. Reichel, and H. Ibach, *Identification of strained silicon layers at Si-SiO_2 interfaces and clean Si surfaces by nonlinear optical spectroscopy*, Phys. Rev. Lett. **71**(8), 1234 (1993).

[13] J. F. MacGilp, M. Cavanagh, J. R. Power, and J. D. O'Mahony, *Probing semiconductor interfaces using nonlinear optical spectroscopy*, Optical Engineering **33**(12), 3895 (1994).

[14] C. Meyer, G. Lüpke, U. Emmerichs, F. Wolter, H. Kurz, C. H. Bjorkman, and G. Lucovsky, *Electronic transitions at $Si(111)/SiO_2$ and $Si(111)/Si_3N_4$ interfaces studied by optical second-harmonic spectroscopy*, Phys. Rev. Lett. **74**(15), 3001 (1995).

[15] J. R. Power, J. D. O'Mahony, S. Chandola, and J. F. McGilp, *Resonant optical second harmonic generation at the steps vicinal Si(001)*, Phys. Rev. Lett. **75**(6), 1138 (1995).

[16] P. Godefroy, W. de Jong, C. W. van Hasselt, M. A. C. Devillers, and T. Rasing, *Electric field induced second harmonic generation spectroscopy on a metal-oxide-silicon structure*, Appl. Phys. Lett. **68**(14), 1981 (1996).

[17] U. Höfer, *Nonlinear optical investigations of the dynamics of hydrogen interaction with silicon surfaces*, Appl. Phys. A **A 63**, 533 (1996).

[18] K. Pedersen and P. Morgen, *Optical second-harmonic generation spectroscopy on Si(111) (7×7)*, Surf. Sci. **377-379**, 393 (1997).

[19] J. I. Dadap, Z. Xu, X. F. Hu, M. C. Downer, N. M. Russell, J. G. Ekerdt, and O. A. Aksipetrov, *Second-harmonic spectroscopy of a Si(100) surface during calibrated variations in temperature and hydrogen coverage*, Phys. Rev. B **56**(20), 13367 (1997).

[20] G. Lüpke, *Characterization of semiconductor interfaces by second-harmonic generation*, Surface Science Reports **35**, 75 (1999).

[21] M.C. Downer, B.S. Mendoza and V.I. Gavrilenko, Surface and Interface Analysis, in press (2001).

[22] P. T. Wilson, Y. Jiang, O. A. Aksipetrov, E. D. Mishina, and M. C. Downer, *Frequency-domain interferametric second-harmonic spectroscopy*, Phys. Rev. B **24**, 1 (1999).

[23] S.A.Mitchell, M.Mehendale, D.M.Villeneuve, C.P.Flueraru, and R. Boukherroub, Surf. Sci. p. 660 (2001).

[24] B. S. Mendoza and W. L. Mochán, *Local-field effect in the second-harmonic-generation spectra of Si surfaces*, Phys. Rev. B **53**(16), R10473 (1996).

[25] B. S. Mendoza and W. L. Mochán, *Polarizable-bond model for second harmonic generation*, Phys. Rev. B **55**(4), 2489 (1997).

[26] P. Guyot-Sionnest, A. Tadjeddine, and A. Liebsch, *Electronic distribution and nonlinear optical response at the metal-electrolyte interface*, Phys. Rev. Lett. **64**(14), 1678 (1990).

[27] B. S. Mendoza, A. Gaggiotti, and R. Del Sole, *Microscopic theory of second harmonic generation at Si(100) surfaces*, Phys. Rev. Lett. **81**(17), 3781 (1998).

[28] B. S. Mendoza, W. L. Mochán, and J. A. Maytorena, *Visible-infrared sum and difference frequency generation at adsorbate-covered Au*, Phys. Rev. B **60**(20), 14334 (1999).

[29] V. I. Gavrilenko, *Optical second harmonic spectra of silicon-adatom surfaces: theory and experiment*, Thin Solid. Films **1-5**, 364 (2000).

[30] D. Lim, M. C. Downer, J. G. Ekerdt, N. Arzate, B. S. Mendoza, V. I. Gavrilenko, and R. Wu, *Optical second harmonic spectroscopy of boron-reconstructed Si(001)*, Phys. Rev. Lett. **84**(15), 3406 (2000).

[31] N. Arzate and B. S. Mendoza, *Microscopic study of surface second harmonic generation from a clean Si(100)c4 × 2 surface*, Phys. Rev. B **63**, 125303 (2001).

[32] B. S. Mendoza, M. Palummo, G. Onida, and R. D. Sole, *Ab inition calculation of second harmonic generation at the Si(100) surface*, Phys. Rev. B **63**(20), 205406 (2001).

[33] Y. R. Shen, *Surface properties probed by second-harmonic and sum-frequency generation*, Nature **337**, 519 (1989).

[34] P. Guyot-Sionnest and Y. R. Shen, *Bulk contribution in surface second-harmonic generation*, Phys. Rev. B **38**(12), 7985 (1988).

[35] K. van Hasselt, *Nonlinear and linear optical studies of Si-SiO_2 interfaces*, Ph.D. thesis, Katholieke Universiteit Nijmegen (1997), contains a nice and comprehensive list of references for this field.

[36] Y. R. Shen, *Surface contribution versus bulk contribution in surface nonlinear optical spectroscopy*, Appl. Phys. B **68**, 295 (1999).

[37] P. Guyot-Sionnest, W. Chen, and Y. R. Shen, *General considerations on optical second-harmonic generation from surfaces and interfaces*, Phys. Rev. B **33**(12), 8254 (1986).

[38] Y. R. Shen, *Wave mixing spectroscopy for surface studies*, Solid State Commun. **102**, 221 (1997).

[39] G. Burns, *Solid State Physics* (Academic Press, Inc., 1985).

[40] T. F. Heinz, C. K. Chen, D. Ricard, and Y. R. Shen, *Spectroscopy of molecular monolayers by resonant second-harmonic generation*, Phys. Rev. Lett. **48**(7), 478 (1982).

[41] A. Janner, *Second-harmonic generation, a selective probe for excitons*, Ph.D. thesis, Rijksuniversiteit Groningen (1998).

[42] H. A. Wierenga, *Magnetization induced optical second-harmonic generation on magnetic multilayers*, Ph.D. thesis, Katholieke Universiteit Nijmegen (1995).

[43] G. Lüpke, D. J. Bottomley, and H. M. van Driel, *SiO_2/Si interfacial structure on vicinal Si(100) studied with second-harmonic generation*, Phys. Rev. B **47**(16), 33 (1993).

[44] Z. Xu, X. F. Hu, D. Lim, J. G. Ekerdt, and M. C. Downer, *Second harmonic spectroscopy of Si(001) surfaces: Sensitivity to surface hydrogen and doping, and applications to kinetic measurements*, J. Vac. Sci. Technol. B **15**(4), 1059 (1997).

[45] O. A. Aksipetrov, I. M. Baranova, and Y. A. Il'inskiĭ, *Surface contribution to the generation of reflected second-harmonic light for centrosymmetric semiconductors*, Sov. Phys. JETP **64**(1), 167 (1986).

[46] J. E. Sipe, D. J. Moss, and H. M. van Driel, *Phenomenological theory of optical second- and third-harmonic generation from cubic centrosymmetric crystals*, Phys. Rev. B **35**(3), 1129 (1987).

[47] V. Mizrahi and J. E. Sipe, *Phenomenological treatment of surface second-harmonic generation*, J. Opt. Soc. Am. B **5**(3), 660 (1988).

[48] W. L. Schaich and B. S. Mendoza, *Simple model of second-harmonic generation*, Phys. Rev. B **45**(24), 14279 (1992).

[49] W. L. Mochán and B. Mendoza, *Second harmonic generation at crystal surfaces*, J. Phys. Condens. Matter **5**, A183 (1993).

[50] M. Cini, R. Del Sole, and L. Reining, *Theory of second-harmonic generation at semiconductor surfaces*, Surf. Sci. **287-288**, 693 (1993).

[51] L. Reining, R. Del Sole, M. Cini, and J. G. Ping, *Microscopic calculation of second-harmonic generation at semiconductor surfaces: As/Si(111) as a test case*, Phys. Rev. B **50**(12), 8411 (1994).

[52] V. I. Gavrilenko and F. Rebentrost, *Nonlinear optical susceptibility of the (111) and (001) surfaces of silicon*, Appl. Phys. A **60**, 143 (1995).

[53] V. I. Gavrilenko and F. Rebentrost, *Nonlinear optical susceptibility of the surfaces of silicon and diamond*, Surf. Sci. **331-333**, 1355 (1995).

[54] J. Rudnick and E. A. Stern, *Second harmonic radiation from metal surfaces*, Phys. Rev. B **4**(12), 4274 (1971).

[55] M. Weber and A. Liebsch, *Density-functional approach to second-harmonic generation at metal surfaces*, Phys. Rev. B **35**(14), 7411 (1987).

[56] W. L. Schaich and A. Liebsch, *Nonretarded hydrodynamic-model calculation of second harmonic generation at a metal surface*, Phys. Rev. B **37**(11), 6187 (1988).

[57] A. Liebsch, *Second-harmonic generation at simple metal surfaces*, Phys. Rev. Lett. **61**(10), 1233 (1988).

[58] A. Liebsch and W. L. Schaich, *Second-harmonic generation at simple metal surfaces*, Phys. Rev. B **40**(8), 5401 (1989).

[59] A. Liebsch, *Electronic excitations at metal surfaces* (Plenum, 1996), 1st ed.

[60] A. Liebsch, *Theory of sum frequency generation from metal surfaces*, Appl. Phys. B **68**, 301 (1999).

[61] N. Arzate and B. S. Mendoza, *Polarizable bond model for optical spectra of Si(100) reconstructed surfaces*, Phys. Rev. B **63**(11), 113303 (2001).

[62] C. M. J. Wijers, P. L. de Boeij, C. W. van Hasselt, and T. Rasing, *Effect of linear polarizability and local fields on surface SHG*, Solid State Commun. **93**(1), 17 (1995).

[63] C. H. Patterson, D. Wearie, and J. McGilp, J. Phys. Condens. Matter (4), 4017 (1992).

[64] B. S. Mendoza, *A theoretical model for second-harmonic generation in silicon*, J. Phys. Condens. Matter **5**, A181 (1993).

[65] M. Cini, *Simple model of electric dipole second-harmonic generation from interfaces*, Phys. Rev. B **43**(6), 4792 (1991).

[66] J. F. McGilp, M. Cavanagh, J. R. Power, and J. D. OMahony, *Spectroscopic optical second-harmonic generation from semiconductor interfaces*, Appl. Phys. A **A 59**, 401 (1994).

[67] J. E. Mejía, B. Mendoza, M. Palummo, G. Onida, R. Del Sole, S. Bergfeld and W. Daum, To be sent.

[68] S. Mitchell, M. Mehendale, D. Villeneuve, and R. Boukherroub, Surf. Sci. (367), 488 (2001).

[69] B. S. Mendoza, A. Gaggiotti, and R. Del Sole, *Microscopic theory of second harmonic generation at the Si(100)2×1 surface*, Phys. Stat. Sol. (a) **170**(2), 343 (1998).

[70] N. Arzate, J. E. Mejía, B. S. Mendoza, and R. Del Sole, *DC-electric-field-modified second-harmonic generation at the Si(100) surface*, Appl. Phys. B **68**(3), 629 (1999).

[71] J. Mejía and B. S. Mendoza, *Second harmonic generation from single-domain Si(100) surface*, Surf. Sci. **487**, 180 (2001).

[72] V. I. Gavrilenko, R. Q. Wu, M. C. Downer, J. G. Ekerdt, D. Linn, and P. Parkinson, *Optical second harmonic spectra of Si(001) with H and Ge adatoms: first principles theory and and experiment*, Thin Solid. Films **1**, 364 (2000).

[73] W. L. Mochán and R. G. Barrera, *Intrinsic surface-induced optical anisotropies of cubic crystals: Local-field effect*, Phys. Rev. Lett. **55**(11), 1192 (1985).

[74] W. L. Mochán and R. G. Barrera, *Local-field effect on the surface conductivity of adsorbed overlayers*, Phys. Rev. Lett. **56**(20), 2221 (1986).

[75] Y. R. Shen, *The principles of nonlinear optics* (John Wiley & Sons, 1984).

[76] A. Guerrero and B. S. Mendoza, *Model for great enhancement of second-harmonic generation in quantum dots*, J. Opt. Soc. Am. B **12**(4), 559 (1995).

[77] F. W. de Wette and G. E. Schacher, *Internal field in general dipole lattices*, Phys. Rev. **137**(1A), A78 (1965).

[78] R. Del Sole, *Present status of the theory of surface optical properties*, Phys. Stat. Sol. (a) **170**(2), 183 (1998).

[79] L. D. Landau and M. Lifshitz, *Quantum Mechanics* (Pergamon Press., 1977), 3rd ed.

[80] A. Bagchi and R. G. Barrera and A. K. Rajagopal, *Perturbative approach to the calculation of the electric field near a metal surface*, Phys. Rev. B **20**(12), 4824 (1979).

[81] R. R. Schlicher and W. Becker and J. Bergou and M. O. Scully, *In Quantum Electrodynamics and Quantum Optics*, edited by A. O. Barut (Plenum, New York, 1984) See. Eqs. (2.17)-(2.20).

[82] J. C. Slater and G. F. Koster, *Simplified LCAO method for the periodic potential problem*, Phys. Rev. **94**(6), 1498 (1954).

[83] Neil W. Ashcroft and N. David Mermin, *Solid State Physics* (Saunders College, 1976).

[84] T. J. Lenosky, J. D. Kress, I. Kwon, A. F. Voter, B. Edwards, D. F. Richards, S. Jang, and J. B. Adams, *Highly optimized tight-binding model of silicon*, Phys. Rev. B **55**(3), 1528 (1997).

[85] P. Vogl, H. P. Hjalmarson, and J. D. Dow, *A semi-empirical tight-binding theory of the electronic structure of semiconductors*, J. Phys. Chem. Solids **44**(5), 365 (1983).

[86] J.-M. Jancu, R. Scholz, F. Beltram, and F. Bassani, *Empirical spds tight-binding calculation for cubic semiconductors: General method and material parameters*, Phys. Rev. B **57**(11), 6493 (1998).

[87] W. Kohn and L. Sham, Phys. Rev. **140**, A1133 (1965).

[88] W. E. Pickett, Comments Solid State Phys. **12**, 57 (1986).

[89] G. Onida, L. Reining, R. W. Godby, R. D. Sole, and W. Andreoni, Phys. Rev. Lett. **75**, 818 (1995).

[90] M. Rohlfing and S. G. Louie, *Electron-hole excitons in semiconductors and insulators*, Phys. Rev. Lett. **81**(11), 2312 (1998).

[91] S. Albercht, L. Reining, R. D. Sole, and G. Onida, Phys. Rev. Lett. **80**, 4510 (1998).

[92] L. X. Benedict, E. L. Shirley, and R. B. Bohn, Phys. Rev. Lett. **80**, 4514 (1998).

[93] L. Hedin, Phys. Rev. **139**, A796 (1965).

[94] R. Del Sole and R. Girlanda, Phys. Rev. B **48**, 11789 (1993).

[95] Z. H. Levine and D. C. Allan, Phys. Rev. Lett. **63**, 1719 (1989).

[96] B. Adolph and F. Bechstedt, Phys. Rev. B **57**, 6519 (1998).

[97] J. D. Jackson, *Classical electrodynamics* (John Wiley & Sons, 1975), 2nd ed.

[98] J. R. Power, P. Weightman, S. Bose, A. I. Shkrebtii, and R. Del Sole, *Sensitivity of reflectance anisotropy spectroscopy to the orientation of Ge dimers on vicinal Si(001)*, Phys. Rev. Lett. **80**(14), 3133 (1998).

[99] A. I. Shkrebtii and R. Del Sole, *Microscopic calculation of the optical properties of Si(100)2×1: Symmetric versus asymmetric dimers*, Phys. Rev. Lett. **70**(17), 2645 (1993).

[100] C. Noguez, C. Beitia, W. Preyss, A. I. Shkrebtii, M. Roy, Y. Borensztein, and R. Del Sole, *Theoretical and experimental optical spectroscopy study of hydrogen adsorption at Si(111)-(7×7)*, Phys. Rev. Lett. **76**(26), 4923 (1996).

[101] M. Palummo, G. Onida, R. Del Sole, and B. S. Mendoza, *Ab initio optical properties of Si(100)*, Phys. Rev. B **60**(4), 2522 (1999).

[102] D. J. Chadi, *Atomic and electronic structures of reconstructed Si(100) surfaces*, Phys. Rev. Lett. **43**(1), 43 (1979).

[103] A. I. Shkrebtii, R. D. Felice, C. M. Bertoni, and R. Del Sole, *Ab initio study of structure and dynamics of the Si(100) surface*, Phys. Rev. B **51**(16), 11201 (1995).

[104] G. Lüpke, D. J. Bottomley, and H. M. van Driel, *Second- and third-harmonic generation from cubic centrosymmetric crystals with vicinal faces: phenomenological theory and experiment*, J. Opt. Soc. Am. B **11**(1), 33 (1994).

[105] U. Höfer, private communication.

[106] A.I. Shkrebtii, Private communication.

[107] T. Rasing, J. Magn. Magn. Mater **175**, 35 (1997).

[108] J. F. McGilp, *Second-harmonic generation at semiconductor and metal surfaces*, Surface Rev. and Lett. **6**(3-4), 529 (1999).

[109] F. Cargnoni, C. Gatti, E. May, and D. Narducci, *Geometrical reconstructions and electronic relaxations of silicon surfaces. I. An electron density topological study of H-covered and clean Si(111)(1×1) surfaces*, The Journal of Chemical Physics **112**(2), 887 (2000).

[110] C. H. Patterson, *A novel method for computing bond-bond interactions of large systems*, Chemical Physics Letters **213**(1,2), 59 (1993).

[111] C. H. Patterson, Surf. Sci. (304), 365 (1994).

[112] C. E. Moore, *Atomic Energy Levels* (NBS, Washington, 1970).

[113] T. Sunada, et al., *22nd International Conference on Solid State Devices and Materials*, Sendai, Japan, 1990, p. 1071 extended abstracts.

[114] A. Kurokawa and S. Ichimura, Appl. Surf. Sci. (436), 100 (1996).

[115] D. Alfonso, C. Noguez, D. Drabold, and S. Ulloa, Phys. Rev. B **54**, 8028 (1996).

[116] W. Daum, private communication.

[117] T. Suzuki et al., Phys. Rev. B **59**, 12305 (1999).

[118] *Propiedades Opticas de Sistemas Inhomogenes de Baja Dimensionalidad.* Cecilia A. Noguez Garrido PhD Tesis, 1995.

[119] C. Noguez, J. Song, S. E. Ulloa, D. A. Drabold, and S. H. Yang, *Size dependence of the optical properties of silicon clusters*, Superlattices and Microstructures **20**(1), 1 (1996).

[120] K. Takayanagi *et al.*, Surf. Sci. **164**, 367 (1985).

[121] K. D. Brommer *et al.*, Phys. Rev. Lett. **68**, 1355 (1992).

[122] We thank Dra. Cecilia Noguez Garrido for allowing us to use the atomic position of Si(111)(7×7).

[123] A. Baldereschi *et al.*, Phys. Rev. B **8**, 5747 (1973).

[124] K. Pedersen and P. Morgen, *Dispersion of optical second-harmonic generation from Si(111)*7×7, Phys. Rev. B **52**(4), R2277 (1995).

[125] T. Suzuki, *Surface-state transitions of Si(111)-7×7 probed using nonlinear optical spectroscopy*, Phys. Rev. B **61**(8), R5117 (2000).